LOW-ENERGY AND SPECTRALLY-EFFICIENT IOT SENSORS WITH LOW-COST ADDITIVE MANUFACTURING

A Dissertation
Presented to
The Academic Faculty

By

Ioannis Kimionis

In Partial Fulfillment
of the Requirements for the Degree
Doctor of Philosophy in the
School of Electrical and Computer Engineering

Georgia Institute of Technology

December 2017

LOW-ENERGY AND SPECTRALLY-EFFICIENT IOT SENSORS WITH LOW-COST ADDITIVE MANUFACTURING

Approved by:

Dr. Manos M. Tentzeris
School of Electrical and Computer Engineering
Georgia Institute of Technology

Dr. Gregory Durgin
School of Electrical and Computer Engineering
Georgia Institute of Technology

Dr. Alenka Zajic
School of Electrical and Computer Engineering
Georgia Institute of Technology

Dr. Yves Baeyens
High-Speed Electronics and Opto-Electronics Research Department
Nokia - Bell Labs
Electrical Engineering Department
Columbia University

Dr. Apostolos Georgiadis
School of Engineering and Physical Sciences
Heriot-Watt University

Date Approved: November 9, 2017

Σα βγεις στον πηγαιμό για την Ιθάκη,	As you set out for Ithaka
να εύχεσαι νάναι μακρύς ο δρόμος,	hope the voyage is a long one,
γεμάτος περιπέτειες, γεμάτος γνώσεις.	full of adventure, full of discovery.
Τους Λαιστρυγόνας και τους Κύκλωπας,	Laistrygonians and Cyclops,
τον θυμωμένο Ποσειδώνα μη φοβάσαι,	angry Poseidon—don't be afraid of them:
τέτοια στον δρόμο σου ποτέ σου δεν θα βρεις,	you'll never find things like that on your way
αν μέν' η σκέψις σου υψηλή, αν εκλεκτή	as long as you keep your thoughts raised high, as long as
συγκίνησις το πνεύμα και το σώμα σου αγγίζει.	a rare excitement stirs your spirit and your body.
Τους Λαιστρυγόνας και τους Κύκλωπας,	Laistrygonians and Cyclops,
τον άγριο Ποσειδώνα δεν θα συναντήσεις,	wild Poseidon—you won't encounter them
αν δεν τους κουβανείς μες στην ψυχή σου,	unless you bring them along inside your soul,
αν η ψυχή σου δεν τους στήνει εμπρός σου.	unless your soul sets them up in front of you.
Να εύχεσαι νάναι μακρύς ο δρόμος.	Hope the voyage is a long one.
Πολλά τα καλοκαιρινά πρωιά να είναι	May there be many a summer morning when,
που με τι ευχαρίστησι, με τι χαρά	with what pleasure, what joy,
θα μπαίνεις σε λιμένας πρωτοειδωμένους·	you come into harbors seen for the first time;
να σταματήσεις σ' εμπορεία Φοινικικά,	may you stop at Phoenician trading stations
και τες καλές πραγμάτειες ν' αποκτήσεις,	to buy fine things,
σεντέφια και κοράλλια, κεχριμπάρια κ' έβενους,	mother of pearl and coral, amber and ebony,
και ηδονικά μυρωδικά κάθε λογής,	sensual perfume of every kind—
όσο μπορείς πιο άφθονα ηδονικά μυρωδικά·	as many sensual perfumes as you can;
σε πόλεις Αιγυπτιακές πολλές να πας,	and may you visit many Egyptian cities
να μάθεις και να μάθεις απ' τους σπουδασμένους.	to gather stores of knowledge from their scholars.
Πάντα στον νου σου νάχεις την Ιθάκη.	Keep Ithaka always in your mind.
Το φθάσιμον εκεί είν' ο προορισμός σου.	Arriving there is what you are destined for.
Αλλά μη βιάζεις το ταξείδι διόλου.	But do not hurry the journey at all.
Καλλίτερα χρόνια πολλά να διαρκέσει·	Better if it lasts for years,
και γέρος πια ν' αράξεις στο νησί,	so you are old by the time you reach the island,
πλούσιος με όσα κέρδισες στον δρόμο,	wealthy with all you have gained on the way,
μη προσδοκώντας πλούτη να σε δώσει η Ιθάκη.	not expecting Ithaka to make you rich.
Η Ιθάκη σ' έδωσε τ' ωραίο ταξείδι.	Ithaka gave you the marvelous journey.
Χωρίς αυτήν δεν θάβγαινες στον δρόμο.	Without her you would not have set out.
Άλλα δεν έχει να σε δώσει πια.	She has nothing left to give you now.
Κι αν πτωχική την βρεις, η Ιθάκη δεν σε γέλασε.	And if you find her poor, Ithaka won't have fooled you.
Έτσι σοφός που έγινες, με τόση πείρα,	Wise as you will have become, so full of experience,
ήδη θα το κατάλαβες η Ιθάκες τι σημαίνουν.	you will have understood by then what these Ithakas mean.

Κ.Π. Καβάφης, Ιθάκη C.P. Kavafy, Ithaka

To the ones who love me the most: *My Parents - My Sister - My Sofia.*

ACKNOWLEDGEMENTS

"Ithaka" symbolizes the goal. Having the goal takes you out to the journey. For a PhD Candidate, the goal is to obtain the highest of all degrees - the doctorate -, but the journey - the way to obtain it - is clearly unknown from the beginning. And while the road to the PhD is a highly personal effort, the support one gets on the way has to be acknowledged.

My advisor Dr. Tentzeris has been the greatest and most knowledgable mentor that I could have wished for! He always gave detailed feedback on my work and excellent advice on shaping my research career. His ethos and support have exceed all of my expectations. Dr. Durgin has given great comments on my work and his presence in my committee has strengthened my confidence on my work's impact in the field of wireless communications. Dr. Zajic can not be thanked enough for serving my committee and letting me use her lab's facilities when my testing equipment unexpectedly malfunctioned before a big deadline. Dr. Baeyens also served my committee, and is highly thanked for giving me the opportunity to work at Bell Labs, the pioneering research center, during my PhD and right after it. Last, but not least, Dr. Georgiadis served my committee, but apart from that, he was my most-active colleague during my doctoral work. A great amount of the projects in this thesis were enhanced with his technical excellence and hands-on experience, which he passed to me with generosity.

My father has been there; he has done his PhD journey and knows the courage that it takes. He talked to me after failures and pinpointed that I should not expect something to come out easily. My mother always cared about my well-being; she had experienced my father's journey at first hand, so she knew how nervous and anxious one becomes during the PhD, and reminded me that I have to take care of myself. My sister has always been my big sister! She has cheered me up so many times and has recognized every little of my achievements with full enthusiasm - she is simply the best. My Sofia has always been so supportive and she has given me so much motivation through endless discussions and brainstorming; she is the proof that a beautiful relationship that colors your life will give you inspiration and optimism to follow any of your dreams.

The ATHENA Lab members have been great collaborators and we have shared long times of work and fun together in and out of the lab. My roommates have made everyday-life all these years in Atlanta more enjoyable. Special thanks goes to my long-time friend Konstantinos who took a flight just to attend my defense. Finally, I can only feel lucky for making genuinely good friends in GeorgiaTech: Ioakeim, Filippos, Yiannis. I like to tease them by saying that if I had not met them, I would have probably graduated sooner, but where would all the fun be?

TABLE OF CONTENTS

Acknowledgments v

List of Tables ix

List of Figures x

Chapter 1: Introduction 1

1.1 Low-power Backscatter communication 2

1.2 Integrated IoT Sensors 3

1.3 Prior art 4

Chapter 2: Backscatter front-ends for increased tag range 13

2.1 Increasing Scattering Efficiency 13

2.2 Reflection Amplifier Design 20

2.3 Phase Shift Modulator Design 23

2.4 System Characterization 26

Chapter 3: Backscatter front-ends for increased spectral efficiency 32

3.1 Arbitrary signal backscattering 32

3.2 Signal Model 34

3.3 Continuous Load Variation 37

3.4 Pulse Shaping Front-end Design 40
3.4.1 PIN Diode Front-end 41
3.4.2 FET Switch Front-end 43
3.5 Processing and Measurements 44
3.5.1 Offline Processing 45
3.5.2 Backscatter Communicator 51
3.6 Pulse Shaping Measurements 52
3.7 Front-end Energy Efficiency 56
3.7.1 Energy per bit E_{bit} 59
3.7.2 Average reflected power $|\Delta\Gamma|^2$ 60
3.7.3 Pulse Energy Loss 60
3.7.4 Receiver Bandwidth (Rx BW) Energy Loss 61
3.7.5 Energy Efficiency 62
3.7.6 Link Budgets 63
3.8 Practical MCU Implementation 64

Chapter 4: Extreme-datarate backscatter front-ends 68

4.1 Pushing Backscatter Radio to mmWave 68
4.2 mmWave Backscatter Front-end 69
4.3 Flexible printed mmWave backscatter array 72
4.4 End-to-end mmWave Backscatter System 75
4.5 Gbit Backscatter Communication 77

Chapter 5: Origami Front-ends for energy harvesting 85

5.1 Powering randomly-deployed sensors 85
5.2 Origami Packaging 87
5.3 3D & Inkjet Origami Manufacturing 90
5.4 Printed Antenna Measurements 99
5.5 Multi-source RF Energy Harvester 100
5.6 Harvester Measurements 105

Chapter 6: Flexible printed front-ends for UWB harvesting 110

6.1 Decade-bandwidth flexible RF harvester 111
6.2 Inkjet-printed Harvester Fabrication 113
6.3 Inkjet-printed UWB harvester performance 116

Chapter 7: Summary of Contributions and Future directions 119

7.1 Summary of Contributions 119
7.2 Future Directions 120

References 128

LIST OF TABLES

2.1 Reflection Amplifier Consumption. 22

3.1 Backscatter front-ends comparison. Bitrate: R=100 kbps, Receiver Bandwidth: B=R/2 (1 Sample/bit) 58

4.1 Comparison of high-order constellation backscatter front-ends 81

6.1 UWB Rectifier Optimization Parameters, P = -10 dBm 114

LIST OF FIGURES

1.1 Backscatter radio: reflection-based communication. 2

1.2 Left: Sensor block diagram. Right: 3D cube with on-package antennas and enclosed RF electronics. 3

1.3 Backscatter sensor network topology (100–200 m range) [1]. 7

2.1 Left: conventional backscatter RF tag modulator. Right: proposed tag with reflection amplifier and binary phase shift modulator. 14

2.2 For a tag with a conventional load modulator, both reflection coefficient points lie in the Smith chart. In the ideal case, Γ_0 and Γ_1 are antipodal. . . . 18

2.3 For a reflection amplifier tag that switches the amplifier on and off, Γ_0 ('off'-state) lies inside the Smith chart, while Γ_1 ('on'-state) lies away from the unitary circle (reflection gain). 18

2.4 For a reflection amplifier tag that utilizes a phase shift modulator, Γ_0 and Γ_1 can both lie far from the unitary circle. Maximum distance between Γ_0 and Γ_1 can be achieved when these are diametrically opposed. 19

2.5 Maximum acceptable phase shifter loss for given reflection amplifier gain, to achieve tag SNR gain over conventional tags with load modulators. . . . 19

2.6 Reflection amplifier schematic: Negative resistance amplifier topology with a common input/output terminal (RF PORT). The amplifier is biased with a low DC voltage to prevent oscillations. An RF blocking filter is utilized at the bias point to prevent RF leakage to the DC supply. 20

2.7 Fabricated prototypes. Left: phase shift modulator. Right: reflection amplifier. 21

2.8 Reflection amplifier gain measurements for different input power levels and DC bias voltage values. 21

2.9 Delay line phase shift modulator block diagram. 24

2.10 Transmission coefficient values of the implemented binary phase shift modulator. State 0: 90° delay. State 1: No delay. 25

2.11 Measurements of phase shift modulator insertion loss and return loss for State 0 (90° delay) and State 1 (no delay). 25

2.12 Measured antipodal reflection coefficient values (S_{11}) for the two tag modulation states (-40 dBm input power). 27

2.13 Comparison of reflection coefficient distance between the two tag states for a conventional modulator-only tag and an enhanced backscatter efficiency amplifier-equipped tag (-40 dBm input power). 27

2.14 Measured backscattered spectrum of a conventional tag without a reflection amplifier and an amplifier-equipped tag. Both tags are excited with a 915 MHz CW and continuously switch between two modulation states with a 250 kHz rate, thus backscattering a 250 kHz subcarrier. 30

3.1 Spectrum comparison of 100 kbps rectangular pulses (typically used in backscatter radio) and square root raised cosine (SRRC) pulses of the same energy. Using pulse shaping for backscatter radio significantly reduces the required bandwidth per RFID tag or backscatter sensor. 33

3.2 Left: Conventional tag switching between two discrete impedance loads. Right: Pulse shaping tag with variable impedance load. 34

3.3 Reflection coefficient of (3.4) as a function of bias voltage in linear form and impedance representation. 36

3.4 Reflection coefficient of (3.4) decomposed to magnitude and phase components, defining a positive and a negative reflected signal region. 37

3.5 Inverted function of (3.6) providing the required bias voltage to achieve a certain reflection coefficient value. 37

3.6 Left: pulse to be transmitted. Center: transformation to reflection coefficient values (applying (3.7)). Right: transformation to required bias voltage (applying (3.8)). 40

3.7 Pulse shaping front-end schematic (left) and prototype (right). 41

3.8 Reflection coefficient versus bias voltage level (0–1 Volts) for PIN diode front-end (913 MHz). 42

3.9 Front-end characterization setup. 43

3.10 FET implementation of pulse shaping front-end schematic (left) and prototype (right). 43

3.11 Reflection coefficient versus bias voltage level (0–2 Volts) for FET front-end (913 MHz). 45

3.12 Characterization, processing, and communication steps. 46

3.13 Measured reflection coefficient variation across 850–950 MHz band for PIN and FET front-ends. 47

3.14 Normalization of reflection coefficient values. Measured data from PIN diode used for processing. 49

3.15 Inverted $V_{\text{bias}}(\hat{\Gamma})$ function and polynomial-fitted $\hat{V}_{\text{bias}}(\hat{\Gamma})$ points. Measured data from PIN diode used for processing. 50

3.16 Two SRRC pulses (one positive and one negative) in reflection coefficient and bias voltage representation.Measured data from PIN diode used for processing. 50

3.17 Front-end measurement setup. 52

3.18 50-bit SRRC-modulated waveform to be backscattered. Top: In reflection coefficient domain. Bottom: Translated to bias voltage domain with measured PIN front-end data. 53

3.19 SDR-measured backscatter signals in time domain. 1: conventional rectangular pulses. 2 & 3: SRRC pulses with PIN front-end. 4: SRRC pulses with FET front-end & 5: SRRC pulses with MCU + FET front-end. 54

3.20 Eye diagrams for SRRC pulse transmission and received pulses overlay for ideal SRRC, measured PIN-generated SRRC, and measured FET-generated SRRC. 55

3.21 Measured spectrum comparison of wireless SDR-received backscatter rectangular pulse and SRRC pulse-shaped backscatter. The strong DC peak corresponds to the reader's CW that illuminates the backscatter modulator. . 57

3.22 Measured spectrum comparison of rectangular pulse-modulated waveform, SRRC pulse-shaped waveform from the PIN front-end, SRRC pulse-shaped waveform from the FET front-end, and SRRC pulse-shaped waveform from the FET driven by an MCU. 57

3.23 Pulse shaping FET front-end interfaced to MCU board. Only the MCU and JTAG programming connector are utilized from the development kit. 65

3.24 Pulse shaping implementation options. 66

4.1 Front-end for mmWave backscatter communication. 69

4.2 Physical layout of mmWave backscatter front-end. 70

4.3 Prototype of mmWave backscatter front-end on Rogers RO4003C laminate. 71

4.4 Backscatter modulation factor $\Delta\Gamma$ versus frequency for front-end DC bias voltages of 0 V and 1 V. 71

4.5 Inkjet-printed 5×1 array prototype with 2.92 mm (K) connector for VNA characterization. 72

4.6 Simulated and measured array return loss (RL). 73

4.7 Simulated 5×1 array directivity. 73

4.8 Simulated 5×1 array realized gain. 74

4.9 Microphotographs of inkjet-printed SNP metallization on LCP. Left: microstrip-to-patch transition. Right: 3-lead HEMT footprint (0402 SMD package). . . 74

4.10 Gbit-datarate capable mmWave backscatter tag. 75

4.11 End-to-end millimeter-wave backscatter system for Gigabit communication. 75

4.12 Left: Wireless backscatter testing setup. Right: Tx and Rx chains with Software Defined Radio. 76

4.13 Backscattered frequency for sensing examples. Top: Presence detection with photocell. Bottom: Soil moisture detection with capacitive probes. . . 77

4.14 Backscattered subcarrier at 2 GHz and 4 GHz, and SNR versus subcarrier frequency. 78

4.15 Measurement setup for Gbit-datarate mmWave backscatter. 79

4.16 Demodulated BPSK Gbit backscatter. 80

4.17 Heterodyne modulation and demodulation of Gbit-datarate mmWave backscatter. Grey lobes correspond to spectra of complex-valued signals. 82

4.18 Demodulated QPSK Gbit backscatter. 83

4.19 Demodulated 16-QAM Gbit backscatter. 84

5.1 3D cube with orthogonally-positioned on-side planar antennas on the sides and enclosed RF energy harvesting electronics. 86

5.2 Origami folding of planar structure to realize a 3D shape. 88

5.3 All-additive manufacturing: 3D printing of substrate and inkjet printing of conductive features. 89

5.4 Partial views of the package exterior (left) and interior (right). 90

5.5 Rendering of the flat configuration of the folding package used for 3D printing. 91

5.6 Exploitation of the full 3D printer bed for building longer-dimension structures. 91

5.7 DMA (Dynamic Mechanical Analysis) of Grey60 yielding T_g of $55°$C. . . . 93

5.8 Shape recovery ratio vs. time for Grey60. 93

5.9 Rendering of the hinge design in a $90°$ folded orientation. 94

5.10 (a) Silver nanoparticle (SNP) ink layer with partial diamminesilver acetate (DSA) ink layer on top. (b) SNP+DSA patch after heat-drying. 96

5.11 Comparison of sheet resistance between DSA-only and DSA+SNP metallization. 97

5.12 Single patch antenna fabricated on 3D-printed substrate. 98

5.13 S-parameters of the patch antennas. 99

5.14 (a) Inkjet-printed patch antenna on unfolded 3D-printed cube. (b) "Origami"-folded cube after heating, folding, and cooling down. 100

5.15 Measured and simulated realized gain of a single inkjet-printed patch. . . . 101

5.16 Measured and simulated cross-polarization isolation of a single inkjet-printed patch. 101

5.17 Summation of two harvesters' outputs. Top: Single harvester. Bottom: Double harvester. 103

5.18 Schematic of the 2-port harvester with dc combining. 104

5.19 Fabricated harvester prototype with on-board matching. 105

5.20 Measured harvester ports' return loss and coupling (input power level: -14.5 dBm). 106

5.21 Harvester port matching across frequency band and input power levels. Resonance around -14.5 dBm/2.3 GHz. 106

5.22 Harvester port isolation across frequency band and input power levels. High isolation (more than 45 dB) for all points. 107

5.23 Harvester output voltage versus port input power. 108

5.24 Origami package with harvester electronics inside. 108

5.25 Wireless measurement setup for the origami RF harvester. 109

6.1 Rectifier impedance matching network consisting of a series inductor and a non-uniform transmission line. 111

6.2 Top: SMS730 diode parasitic model. Bottom: Optimization schematic for decade bandwidth rectifier with non-uniform transmission line. 112

6.3 Rectifier RF-dc conversion efficiency without and with UWB matching (RF input power -10 dBm, load value 1.3 kΩ). 113

6.4 Printed board fabrication process. 114

6.5 Left: Drilled via holes on polyimide and copper tape substrate. Right: Inkjet-printed board; feeding section, non-uniform transmission line, and SMD components pads. 115

6.6 Microphotograph of assembled harvester, with SMD components and epoxy-metallized vias. 116

6.7 Flexible UWB harvester prototype with end-launch SMA connector and V_{out} testing output. 116

6.8 S_{11} Smith Chart for input power $P = 0$ dBm and $R_L = 1.3$ kΩ. 117

6.9 Contours of simulated and measured rectifier dc output voltage for varying input power level and frequency values. 117

6.10 Simulated and measured efficiency for inkjet-printed UWB harvester. 118

7.1 Potential for origami technology: shape-changing structures for on-the-fly reconfigurable RF systems and smart wireless sensors. 121

SUMMARY

This thesis develops low-energy and low-cost communication and powering modules for sensors and devices for the Internet of Things (IoT). To minimize the energy footprint of IoT sensors, backscatter radio is utilized for communication, instead of power-demanding active radios. Custom tag front-ends are designed to increase the sensors' maximum range and incorporate RF energy harvesters for battery recharging or battery exclusion. Custom, non-conventional front-ends are proposed that a) maximize the backscattering efficiency and operating range, b) generate smooth, arbitrary waveforms for reduced per-sensor bandwidth occupancy which allows high network density, c) boost datarates up to the Gigabit-range by utilizing mmWave frequency bands. RF harvesting front-ends are developed to complement the communication front-ends, taking into account the complex requirements of the IoT: hassle-free device deployment without knowledge/predetermined RF source positions or frequency bands. Additive manufacturing (3D- and inkjet- printing) are fully exploited to build compact Origami-reconfigurable packages with embedded antennas and front-ends or fully-flexible and miniaturized printed communicators and harvesters that can be integrated to wearables and small portable devices. The broad range of modules presented in this thesis will reduce the complexity of IoT nodes ranging from low-bitrate, long-range sensors at UHF frequencies up to ultra-wideband backscatter communicators operating at mm-Wave bands for real-time, high-datarate applications.

CHAPTER 1
INTRODUCTION

Wireless sensor networks (WSNs) have been an active field of research and engineering for many years [2], with applications that extend from environmental and habitat sensing [3, 4] to pipe network crack detection [5] and health monitoring [6]. WSN nodes have been constructed in the form of motes with radio modules or tags with low-power communicators, and numerous research testbeds for have been built for the comparison of WSN nodes, in terms of their communication performance, sensing capabilities, power consumption, fabrication cost, etc [2, 7–9].

A new path for wireless systems has opened with the advent of the Internet-of-Things (IoT), with ubiquitous connected systems, large-scale sensing, smart home sensors, wearables, and wirelessly-powered devices [10–12]. The new large scale aspect of the IoT calls for low-cost implementations of sensors that deviate from the conventional fabrication techniques, lower energy consumption levels with alternative energy sources, and re-designed modules to accommodate the new tight cost and energy constraints.

In this thesis, a series of front-end modules are developed for next-generation low-cost IoT sensors. Backscatter communication is favored, leveraging reflection-type radio technology found in RFIDs for use in dynamic-data sensors, rather than static ID information. Improved range, power consumption, and spectral efficiency are the aspects covered for novel communication front-ends, as well as multi-source and multi-band energy harvesting for wireless powering front-ends. Additive manufacturing technologies (AMTs) are considered, which have been proven to be efficient for diverse device implementation, including but not limited to sensors, RFIDs, antennas, passives, and active components [13, 14]. The fabrication flexibility enabled by AMTs, such as inkjet printing and 3D printing, provides a new implementation framework for energy-aware and low-cost IoT modules, with

the potential of mass fabrication in roll-to-roll processes with a low material cost and minimized waste.

1.1 Low-power Backscatter communication

Existing commercial WSN technologies utilize active radios for wireless connectivity such as ZigBee, Bluetooth, or other power-hungry systems. These Marconi-type radios are usually the overhead for both the monetary cost and the energy consumption of a WSN node, because of the complex active radio frequency (RF) components they incorporate. The high cost per node along with the high energy demands are prohibiting factors for the scalability of a WSN to dense network levels. Thus, conventional WSN technologies cannot serve very large scale IoT sensing under a relatively low budget or very limited energy resources. Scalability issues apply to scenarios such as environmental sensing, healthcare monitoring for real-time patient data transmission, chemical safety sensors in public spaces, or food quality sensors on food packages. The approaches and technologies developed throughout this work can be applied to a plethora of systems, tailored to the constraints of power, bandwidth, size, cost, etc.

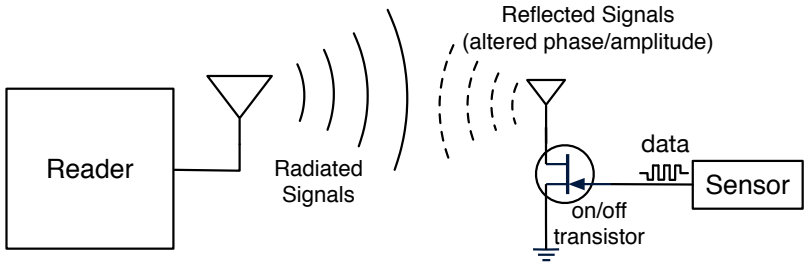

Figure 1.1: Backscatter radio: reflection-based communication.

Instead of actively radiating power to transmit information, a node may reflect induced RF signals to modulate data. The backscatter radio principle is based on emitting a carrier wave that illuminates many nodes (RF tags). A tag's antenna is connected to an impedance switch that changes the antenna load according to the transmitted data. Different loads have

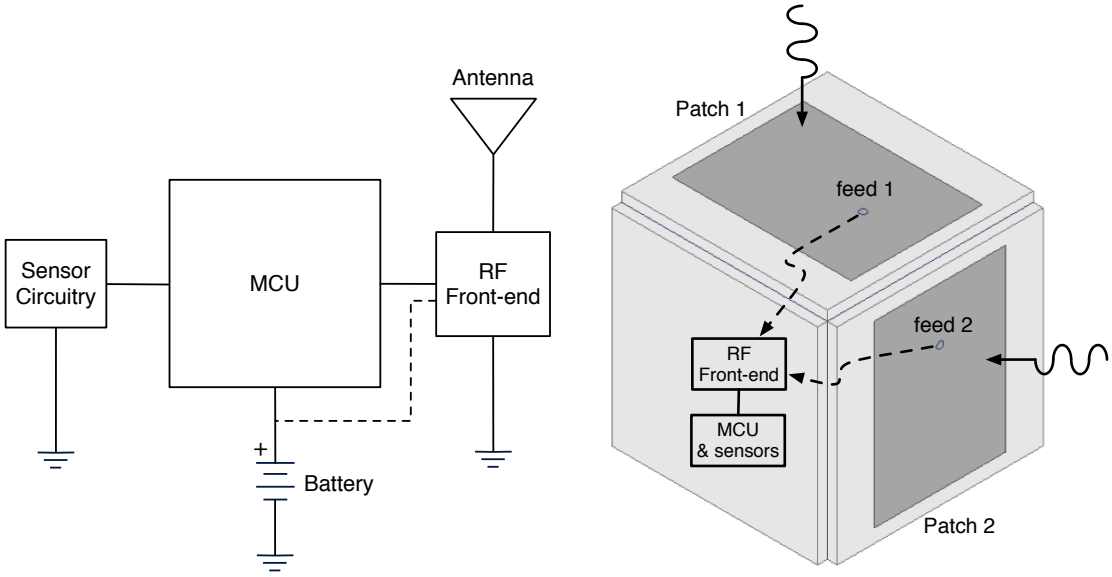

Figure 1.2: Left: Sensor block diagram. Right: 3D cube with on-package antennas and enclosed RF electronics.

the effect of changing the induced signal's amplitude, or phase, or both. That way, the signal is modulated and reflected (scattered back) from the same antenna. The backscattered signals are captured by a receiver (reader) which demodulates and decodes information from each tag/sensor (Fig. 1.1).

Although backscatter radio is not a new idea (first principles presented in 1948), its use has been mainly limited to radio frequency identification (RFID) applications, for identifying people or products in supply chains. However, this communication scheme is also valuable to WSNs and the IoT, since communication can be achieved with minimal RF front-ends requiring one to a few transistors. That way, both the energy requirements and monetary cost of a sensor node are minimized, which facilitates large scale sensor deployments, in contrast with existing radio technologies.

1.2 Integrated IoT Sensors

The general form of an integrated sensor comprises a central computation unit in the form of a low-cost microcontroller (MCU), an RF front-end for communication and RF energy

harvesting, a power source such as a battery, and the sensing circuitry (Fig. 1.2-left). These sensors are targeted for large-scale outdoor or indoor scenarios that require an easy deployment, e.g. spreading compact, rugged-packaged sensors with random orientation within a large area. In such deployments, communication or harvesting might be compromised if the node's antenna does not face to the direction of the central station for conveying data or receiving power wirelessly. Employing novel fully 3D structures, such as a cube, allows for the easy placement of (planar) antennas on multiple faces, enabling simultaneous harvesting/communication over different and potentially real-time reconfiguring (e.g. "origami") orientations (Fig. 1.2-right). RF waves from totally orthogonal planes can be exploited for harvesting and backscatter communication, enhancing the total system efficiency when multiple sources/gateways are present. Such a system can also benefit in the case of a single source that lies in an unknown direction: two orthogonal antennas increase the probability of capturing the source-emitted plane waves, compared to a single antenna facing to a single direction that can only capture RF signals from multipath reflections.

1.3 Prior art

Backscatter radio, i.e. communication by means of reflection rather than radiation, although not a new idea (first principles presented in [15]), has only recently been utilized widely for certain applications. The most prominent commercial use of scatter radio is in radio frequency identification (RFID) applications, for identifying people or products in supply chains. Commercial standards have been developed for RFID, albeit focusing on identification/supply chain applications only [16]. However, this communication scheme can be valuable to other scenarios as well, such as in wireless sensor networks (WSNs) and Internet of Things (IoT) systems. Because communication can be achieved with a single radio frequency (RF) transistor front-end, scatter radio can minimize both energy requirements and monetary cost of each sensor node; this allows then for large scale sensor deployments. Such networks are critical for high-density networks, e.g. for smart

home applications, with tens or hundreds sensing devices in a house or office environment. Moreover, the advent of ubiquitous wearable technology will direct the use of low-power communication for battery conservation. Recent work has shown proof of concept systems that can be used in dense scatter radio (a.k.a. backscatter radio) networks. All those systems are built with low-cost and low-energy principles in mind [13, 17–20], and many utilize energy harvesting, from dedicated or ambient energy sources [21–24].

Extended field coverage is a key characteristic in many WSN applications. This means that the communication range between the sensor *tags* and a *reader* has to be maximized. However, for typical RFID applications, the achieved ranges are inherently limited due to power-up link limitations, since *passive* tags are used, which require energy harvesting to power their electronics. Commonly, these tags rectify a continuous wave (CW) signal, transmitted by the reader. Thus, the achieved range is limited by the so-called "power-up link" [25]. Another major limiting factor is the *monostatic* architecture; the reader box consists of both the transmitter that emits the wave needed for backscatter communication and the receiver that decodes the tag-modulated signals. This means that typical RFID systems suffer from round-trip path loss; specifically SNR at the receiver drops with the fourth power of reader-to-tag distance [26] or the eighth power of the distance, for a two-ray propagation model [27, 28]. In monostatic setups, the tags that lay close to the reader are benefitted from the small distance, while tags that lay far are difficult to be "heard" from the reader. This causes a circular area around the reader, where coverage is limited.

For classic monostatic RFID, there are examples in the literature that suggest various improvements for the tag-to-reader communication. Work in [29–31] focuses on the microwave parameters of the RF tag that impact tag-to-reader communication performance, such as the antenna load selection and the antenna-RFID chip matching. In [32, 33] the authors provide theoretical analysis of multiple input multiple output (MIMO) receivers for the monostatic RFID system. These systems use multiple antennas on the reader to exploit channel diversity for BER reduction. On the other hand, work in [34] utilizes multiple tag

antennas to improve the link performance of a 5.8GHz backscatter radio system and [35] studies the multipath fading in such a system. By exploiting multiple tag antennas, the operating ranges are increased up to 78%.

In the new network topology developed in [1], the carrier emitter is detached from the reader and is reduced to a simple carrier generator of minimal cost, while the reader employees a receive chain only. This *bistatic* architecture effectively creates a coverage cell around the carrier emitter that illuminates the tags within its radius, while the cell might reside at very long distances from the receiving-only reader. To increase the coverage around the field, more sensor cells are created by placing additional low-cost emitters, which cost significantly less than a full monostatic reader. Moreover, when tags employ additional energy sources (batteries, or solar cells), the forward link limitation is relaxed significantly. It is noted that prior art has largely bypassed bistatic architectures and rather focused on industry-standard monostatic reader architectures. An example towards the bistatic direction is [36] which suggests using a single carrier emitter with multiple receiving-only readers (listeners) that cooperate to decode simultaneously emmiting tags, in an attempt to mitigate interference. Another example of a receiving-only reader is given in [37], where a monitor for commercial-standard Gen2 RFID tags is presented. That work exploits heuristic methods of counting pulse durations to determine the transmitted bits and is centered around the industry-standard FM0 modulation scheme [16].

By dislocating the carrier emitter from the receiver, new and more flexible topologies can be set up. Carrier emitters may come in the form of an oscillator and a power amplifier only, and can thus be two orders of magnitude cheaper than the receiver/reader. The reader is a low-cost software defined radio (SDR), which offers the flexibility of processing multiple, arbitrary tag/sensor modulation schemes. A single centralized reader is present on a field, while multiple low-cost carrier emitters are placed randomly around a field with scattered sensors. That way, the emitter-to-tag path loss can be statistically reduced, since it is more likely for a tag to lay close to a carrier emitter. Thus, the overall field cover-

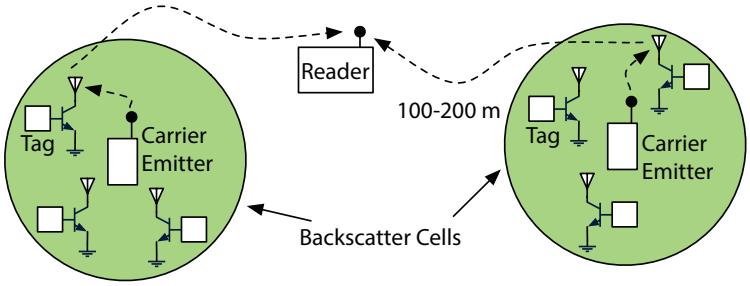

Figure 1.3: Backscatter sensor network topology (100–200 m range) [1].

age is extended, as more emitters are placed around. Such an architecture can be seen in Fig. 1.3, with multiple carrier emitters and one centralized reader, which has been prototyped and experimentally verified to achieve tag-to-reader ranges of 100–200 m, with derived non-coherent on-off keying (OOK) and frequency shift keying (FSK) detectors, custom backscatter tags, and 20 mW of transmitter power.

The topology developed in [1] has significantly boosted the network-aspect of coverage, which is complemented by the non-conventional RF tag front-ends that have been developed throughout this doctoral work.

In prior art, the architecture of most backscatter modulators for radio frequency (RF) tags (e.g. radio frequency identification - RFID) has followed the same pattern; alternating the tag antenna termination between two passive load values to achieve modulation by modifying the reflection of radio waves. Active components (transistors, RF switches, diodes) are introduced to the tag RF front-ends, but are just utilized as mechanisms to switch the antenna load between two states for achieving backscatter modulation. The trend of switching between two load values only has been recently challenged in [38, 39], but the loads used are still passive, limiting the RF tag *scattering efficiency*. Scattering efficiency refers to the amount of power a tag can reflect for a given induced power level, in order to perform tag-to-reader communication [31].

When aiming for long communication ranges of several tens of meters, minimization of the tag bit-error-rate (BER) at the reader is required, which is associated with the tag-scattered signal's signal-to-noise ratio (SNR). The tag-signal's energy is proportional to

$|\Delta\Gamma|^2 \triangleq |\Gamma_1 - \Gamma_0|^2$, where Γ_0, Γ_1 are the complex reflection coefficient values for the two load values a backscatter tag modulator is using. In [31], it has been stated that maximization of $|\Delta\Gamma|$ is required for improving the RF tag scattering efficiency and minimizing the BER at the reader, regardless of the binary modulation scheme utilized. All modulation schemes can benefit from that efficiency increase; amplitude shift keying (ASK) waveforms will have higher amplitude values, phase shift keying (PSK) waveforms will employ signal bases with the maximum possible phase difference, and frequency shift keying (FSK) waveforms will feature an increased waveform amplitude, positively affecting signal demodulation at the reader. The efficient tag demodulation at the reader is translated to an uplink (tag-to-reader) communication range boost, which can be further enhanced by utilizing other-than-monostatic reader architectures. Because RF tags typically utilize passive components for their load modulators, they achieve reflection coefficients Γ_0, Γ_1, with magnitude values less or equal to unity. Thus, all typical load modulators' performance is upper-bounded by $|\Delta\Gamma| \leq 2$, with the equality achieved for coefficients with maximum magnitude (unity) and phase difference π or 180° (antipodal points on the Smith chart). This upper bound is limiting backscatter signal SNR maximization and non-conventional tag designs have to be exploited to override this bound. To achieve values of $|\Gamma| > 1$, active topologies are required that have a *reflection gain* rather than reflection loss.

A reflection amplifier has been previously proposed for 5.8 GHz RFID tags, to amplify the backscattered signal towards the reader by achieving a reflection coefficient higher than unity at one modulation state ($|\Gamma| > 1$) [40]. In that work, the modulation at the amplifier output is achieved by controlling (switching on and off) the amplifier bias; as it will be discussed later, that operation is suboptimal. Moreover that amplifier has been designed without setting strong constraints for the dissipation, and requires a few milliamperes for operation. More recent work in [41] has proposed an amplifier in the same frequency range, which exploits the tunneling effect of diodes and requires a low bias power of 45 μW. In [42] an active 24 GHz tag was proposed, that achieved up to 15 m by transmitting pseu-

dorandom sequences generated by active antennas with integrated oscillators. However, that system was *radiating* signals towards a reader rather than *reflecting* reader-emitted signals and it required 2.5 V and 26 mA for operation. In [43] a 34.45 GHz tag based on a switched injection-locked oscillator was designed, that achieved up to 11.5 m range. It is noted, though, that the front-end incorporates a low-noise amplifier (LNA), power amplifiers, (PAs) and complex circuitry for phase locking. The system requires 3 V for operation and its current consumption reaches up to $40 \sim 50$ mA, which leaves room for dissipation improvement. More recently, active tag loads that show reflection gain with microwatt-level power consumption have been presented [44]. These loads are exploiting the interesting properties of tunnel diodes, which are relatively high-cost discrete components, but are slowly gaining increased popularity in the industry.

In dense IoT/WSN deployments, minimizing the utilized bandwidth (BW) per tag is required to fit a large number of sensors in a dedicated frequency band and also guarantee low out-of-band interference for regulatory reasons. Each tag's backscattered signal spectrum has to decay fast with regard to frequency so that the signal's harmonics are suppressed and do not interfere with nearby sensors, without compromising the signal detection performance. Active radio systems typically utilize pulse shaping techniques to modify the waveform characteristics of the transmitted signals and adapt them according to the requirements of bandwidth, data rate, etc [45, 46]. Although conventional radio utilizes complex electronic components to achieve shaping, backscatter radio typically utilizes minimal RF front-ends consisting of only one or a few nonlinear devices (switches, transistors, diodes) that switch between discrete states [25]. However, this should not be a strongly-limiting factor for getting away from conventional on-off keying (OOK) modulation on sophisticated sensing RFID tags that already employ computational units, such as microcontroller units (MCUs), at the core of their system. Examples of such computation-enabled tags include: a) [18] where a MCU-based tag is built that implements the Gen2 industrial RFID protocol [16], b) [19, 47] where MCU-based tags are built to implement

custom backscatter communication schemes including OOK and frequency-shift keying (FSK) in non-conventional long-range bistatic architectures presented in [1, 48], c) [49] where MCU-based tags are used in a special case of bistatic architecture named ambient backscatter, d) [38, 50] where tags exploit multiple load values and RF multiplexers to achieve high-order modulation constellations, e) [51] where a MCU tag is operating in harmonic mode to backscatter data at the second harmonic of the reader signal. All these examples utilize rectangular pulses for communication and thus require extended bandwidth.

Although works in the field of backscatter radio/RFID have included components that are capable of varying-impedance, they have not exploited the characteristic of continuous load modulation; instead, they have limited the operation to discrete states and rectangular pulses. Examples include [52], where PIN diodes have been utilized for communication, and [53], where photo diodes have been utilized for sensing. In the first example, the PIN diodes are biased with discrete current levels for a certain duration (symbol period) and therefore the backscatter pulses have a rectangular shape with increased bandwidth occupancy. Moreover, due to the architecture of the circuit, only a small portion of the Smith Chart can be utilized for the antenna load, significantly limiting the backscattered signal-to-noise ratio (SNR). In the second example, a sensor utilizes a photo diode as the antenna load and detection is based on the differential radar cross-section (RCS) of the sensor. The differential RCS is calculated from two distinct load states, i.e. that sensor also backscatters rectangular pulses.

In this thesis, the feasibility of generating non-rectangular waveforms with a backscatter tag RF front-end comprising a single non-linear component is demonstrated, by exploiting a continuous variation of the antenna load instead of switching between two discrete values, as in typical backscatter/RFID tags. Appropriate non-linear components include diodes, field-effect-transistors (FETs), and any other components that feature a voltage-controlled or current-controlled impedance characteristic. Such components are widely used and are

available in either discrete semiconductor packages, or they can be implemented on integrated circuit (IC) dies [54].

Another prominent challenge that determines scalability of IoT systems and WSNs is power sufficiency, and recent efforts in the area of radio frequency (RF) energy harvesting promise to overcome the need for manual battery replacement. This is achieved by either utilizing RF harvesting for autonomous sensor operation, or for automatic battery recharging on-site [55, 56]. There have been numerous efforts related to rectenna design, such as for example ones addressing multiband operation [57–59]. Also, a large amount of power rectenna arrays have been considered [60–62]with broadband, dual band, circular or linear polarization characteristics. One of the challenges in designing rectenna arrays has been the trade-off between combining the output of the individual antenna elements in RF forming directive antenna arrays or in dc, forming non-directive rectifier arrays. The combination in RF results in directive systems able to focus towards a specific transmitter. Recent examples of dc-combining rectifiers include [63–65].

Finally, a crucial aspect to accommodate the massive nature of IoT systems is the cost-effective fabrication of all the modules. Additive manufacturing technologies (AMTs) have been proven to be efficient for diverse device implementation, including but not limited to sensors, RFIDs, antennas, passives, and active components [13, 14]. The fabrication flexibility enabled by AMTs, such as inkjet printing, provides a new implementation framework for energy-aware and low-cost IoT modules, with the potential of mass fabrication in roll-to-roll processes with a low material cost and minimized waste. Multiple examples exist for printed passives, since inkjet printing allows the deposition of both conductors and dielectrics, effectively forming capacitors and multilayer inductors on thin flexible substrates [66, 67]. Electromagnetic structures can also be realized, such as transmission lines and waveguides on low-cost paper [68], along with antennas and printed arrays [69, 70]. Recently, 3D printing has been effectively utilized for RF structures and packaging, putting it on the map for high frequency-compatible manufacturing processes. There are success-

ful efforts of combining 3D printing with inkjet printing to form complex 3D electromagnetic structures that will boost the applications that can be realized with AMTs. Also, non-conventional "origami" concepts have been applied to make those structures reconfigurable through shape-changing, which will allow on-the-fly reconfiguration of operation frequency, bandwidth, and directionality [71, 72].

CHAPTER 2

BACKSCATTER FRONT-ENDS FOR INCREASED TAG RANGE

2.1 Increasing Scattering Efficiency

When aiming for long communication ranges of several tens of meters, minimization of the tag bit-error-rate (BER) at the reader is required, which is associated with the tag-scattered signal's signal-to-noise ratio (SNR). In [1], where the complete backscatter radio signal model is derived by accounting for both communication theory and microwave theory, it can be seen that the tag signal SNR at the reader is:

$$\mathrm{SNR} \triangleq \frac{E_b}{N_0} = \frac{P_{\text{tag}}\, T_b}{N_0} \propto |\Delta\Gamma|^2\, T_b. \tag{2.1}$$

E_b is the bit energy, P_{tag} is the average power of the received tag signal at the reader, T_b is the bit duration, and N_0 is the noise power spectral density. The tag-signal's energy is proportional to $|\Delta\Gamma|^2 \triangleq |\Gamma_1 - \Gamma_0|^2$, where Γ_0, Γ_1 are the complex reflection coefficient values for the two load values a backscatter tag modulator is using. In [31], it has been stated that maximization of $|\Delta\Gamma|$ is required for improving the RF tag scattering efficiency and minimizing the BER at the reader, regardless of the binary modulation scheme utilized. All modulation schemes can benefit from that efficiency increase; amplitude shift keying (ASK) waveforms will have higher amplitude values, phase shift keying (PSK) waveforms will employ signal bases with the maximum possible phase difference, and frequency shift keying (FSK) waveforms will feature an increased waveform amplitude, positively affecting signal demodulation at the reader. The efficient tag demodulation at the reader is translated to an uplink (tag-to-reader) communication range boost, which can be further enhanced by utilizing other-than-monostatic reader architectures [1]. Because RF tags typically utilize passive components for their load modulators, they achieve reflec-

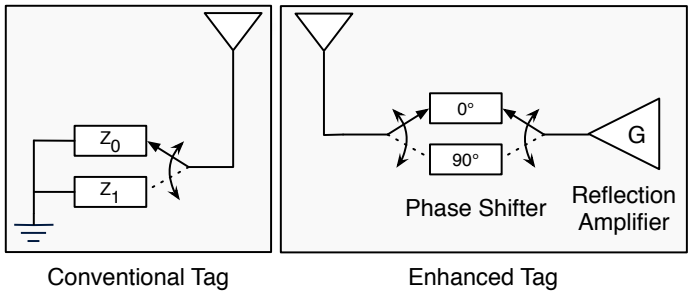

Figure 2.1: Left: conventional backscatter RF tag modulator. Right: proposed tag with reflection amplifier and binary phase shift modulator.

tion coefficients Γ_0, Γ_1, with magnitude values less or equal to unity. Thus, all typical load modulators' performance is upper-bounded by $|\Delta\Gamma| \leq 2$, with the equality achieved for coefficients with maximum magnitude (unity) and phase difference π or 180° (antipodal points on the Smith chart). This upper bound is limiting backscatter signal SNR maximization and non-conventional tag designs have to be exploited to override this bound. Specifically, to achieve values of $|\Gamma| > 1$, active topologies are required that have a *reflection gain* rather than reflection loss.

A typical backscatter radio modulator connected to an antenna with input impedance Z_a is switching the antenna termination between two load values Z_0, Z_1 (Fig. 2.1-left) for bits '0' and '1', respectively [25]. In that way, two different reflection coefficient values

$$\Gamma_0 = \frac{Z_0 - Z_a^*}{Z_0 + Z_a}, \quad \Gamma_1 = \frac{Z_1 - Z_a^*}{Z_1 + Z_a} \tag{2.2}$$

are achieved and the amplitude and/or phase of the backscattered signal are altered [31,73]. The load value selection will affect the reflection coefficient values and different modulation schemes can be achieved: ASK, PSK, or hybrids. Switching between the two loads multiple times per bit period can yield an FSK signal [1], while switching between M load values can yield high-order modulation schemes, such as M-QAM [38]. The backscattered signal constellation is directly related to the points of Γ_0, Γ_1 on the Smith chart. For example, $\Gamma_0 = -1$ and $\Gamma_1 = 1$ would correspond to BPSK modulation, since only the phase

of the backscatter signal changes for the two states, while the amplitude remains the same. The same holds for any two antipodal points on the unitary circle (Fig. 2.2). Notice that for any *passive* load Z_x, the corresponding system reflection coefficient will always have magnitude $|\Gamma_x| \leq 1$. The limitation of $|\Gamma_x| \leq 1$ can be overriden by utilizing a reflection amplifier, which is a negative resistance oscillator [74], sub-biased in a way that no oscillations occur.

The antipodal load modulator in a classic backscatter radio tag (Fig. 2.1-left) that maximizes $|\Delta\Gamma|$ switches between two reflection coefficients Γ_0, Γ_1. These reflection coefficients and their difference magnitude are given by

$$\Gamma_0 = 1\ e^{j\theta}, \tag{2.3}$$

$$\Gamma_1 = 1\ e^{j\theta + j\pi} = -1\ e^{j\theta} = -\Gamma_0 \tag{2.4}$$

$$|\Delta\Gamma| = |e^{j\theta} + e^{j\theta}| = 2, \tag{2.5}$$

with $\theta \in [0, 2\pi)$. This well-known case is depicted on a Smith chart in Fig. 2.2, where both coefficients lie on the unitary circle. Notice that passive tags (e.g. RFIDs) that employ antenna-matched harvesters (that is, the harvester input impedance is $Z_{\text{harv}} = Z_a^*$ to maximize power transfer from the antenna to the harvester module) will switch between a matched and an unmatched state, that is $\Gamma_0 = 0$ and $\Gamma_1 = 1\ e^{j\theta}$, achieving a distance $|\Delta\Gamma| = 1$.

Next, consider a system that consists of a reflection amplifier with power gain G directly interfaced to the antenna (as in [40]). The amplifier is switched on and off to achieve ASK modulation. When the amplifier is off, the equivalent circuit seen by the antenna port is a passive load. The system reflection coefficient will have amplitude $B \leq 1$ and arbitrary phase ϕ_0. When on, the amplifier shows a reflection voltage gain $\sqrt{G}$ and applies a phase

ϕ_1 to the incoming signal. Thus,

$$\Gamma_0 = B\, e^{j\phi_0}, \tag{2.6}$$

$$\Gamma_1 = \sqrt{G}\, e^{j\phi_1}. \tag{2.7}$$

Such two reflection coefficient points are shown in Fig. 2.3. The reflection coefficient difference amplitude is

$$|\Delta\Gamma| = |\sqrt{G}\, e^{j\phi_1} - B\, e^{j\phi_0}|. \tag{2.8}$$

The distance $|\Delta\Gamma|$ is maximized (best case) when $B = 1$ and the line that connects the two points crosses the axis origin $(0, 0)$. This is achieved when $\phi_1 = \phi_0 + \pi$. Then,

$$|\Delta\Gamma| = |\sqrt{G}\, e^{j\phi_0 + j\pi} - e^{j\phi_0}| = \sqrt{G} + 1. \tag{2.9}$$

Similarly, the distance is minimized (worst case) when $B = 1$ and $\phi_1 = \phi_0$. Then,

$$|\Delta\Gamma| = |\sqrt{G}\, e^{j\phi_0} - e^{j\phi_0}| = \sqrt{G} - 1. \tag{2.10}$$

For the proposed system of Fig. 2.1-right, consider a reflection amplifier with a gain G that applies an arbitrary phase ϕ_1 to the incoming signal. If the amplifier is constantly on, then its complex S_{11}-parameter is

$$S_{11}^{\text{amp}} = \sqrt{G}\, e^{j\phi_1}. \tag{2.11}$$

Also, consider a 2-port phase shifter modulator that can selectively shift the phase of the

passing RF signal by 0 or $\pi/2$ by directing it through a delay line, that is

$$S_{21}^{\text{mod}} = \begin{cases} 1\ e^{-j\pi/2}, & \text{State 0,} \\ 1, & \text{State 1.} \end{cases} \tag{2.12}$$

Then the total system input reflection coefficient will be

$$S_{11}^{\text{system}} = S_{21}^{\text{mod}}\ S_{11}^{\text{amp}}\ S_{21}^{\text{mod}} = \begin{cases} -\sqrt{G}\ e^{j\phi_1}, & \text{State 0,} \\ \sqrt{G}\ e^{j\phi_1}, & \text{State 1.} \end{cases} \tag{2.13}$$

Thus, the two reflection coefficients are

$$\Gamma_0 = -\sqrt{G}\ e^{j\phi_1}, \tag{2.14}$$

$$\Gamma_1 = \sqrt{G}\ e^{j\phi_1} = -\Gamma_0, \tag{2.15}$$

which both have an (equal) amplitude greater than unity and, thus, both lie away from the unitary smith chart circle (Fig. 2.4). Also, they are diametrically opposed, and the maximum possible reflection coefficient distance for a given amplifier gain is achieved

$$|\Delta\Gamma| = |\sqrt{G}\ e^{j\phi_1} + \sqrt{G}\ e^{j\phi_1}| = 2\sqrt{G}. \tag{2.16}$$

In practice, the phase shifting modulator will have a power transmission coefficient $0 < T < 1$, and the achievable distance will be

$$|\Delta\Gamma|^{\text{lossy}} = \sqrt{T}\ |\Delta\Gamma|\ \sqrt{T} = 2\ T\sqrt{G}. \tag{2.17}$$

When the factor T is kept high (low insertion loss), the use of an amplifier-phase shift modulator system will yield a higher $|\Delta\Gamma|$ than an on-off amplifier system. When compared

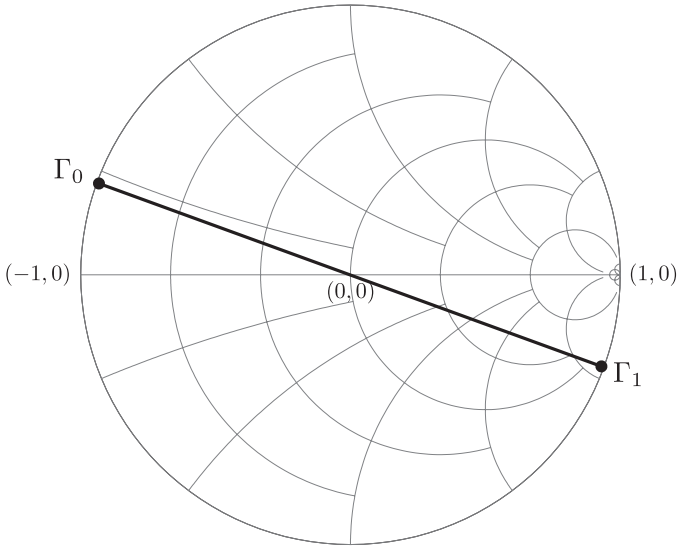

Figure 2.2: For a tag with a conventional load modulator, both reflection coefficient points lie in the Smith chart. In the ideal case, Γ_0 and Γ_1 are antipodal.

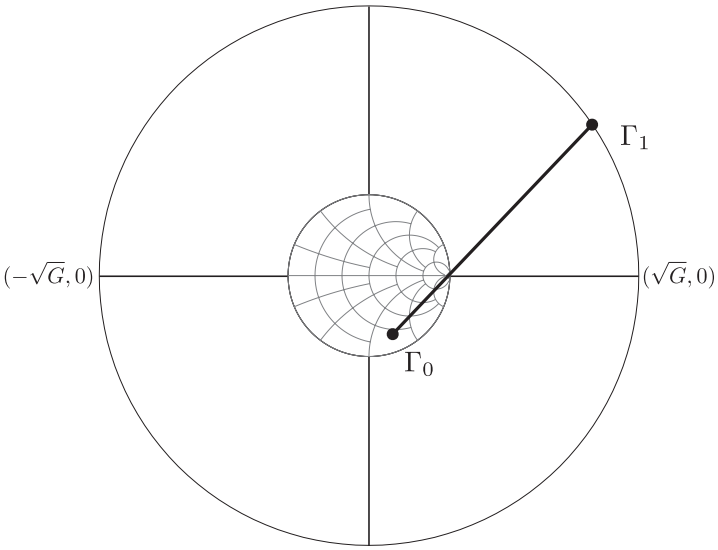

Figure 2.3: For a reflection amplifier tag that switches the amplifier on and off, Γ_0 ('off'-state) lies inside the Smith chart, while Γ_1 ('on'-state) lies away from the unitary circle (reflection gain).

with the best-case on-off amplifier, a system of the proposed architecture is preferred when

$$2\,T\,\sqrt{G} > \sqrt{G} + 1 \Leftrightarrow T > \frac{1}{2} + \frac{1}{2\sqrt{G}}, \tag{2.18}$$

i.e. the insertion loss $10\log_{10} T$ of the phase shifter has to be low. In Fig. 2.5 the maximum

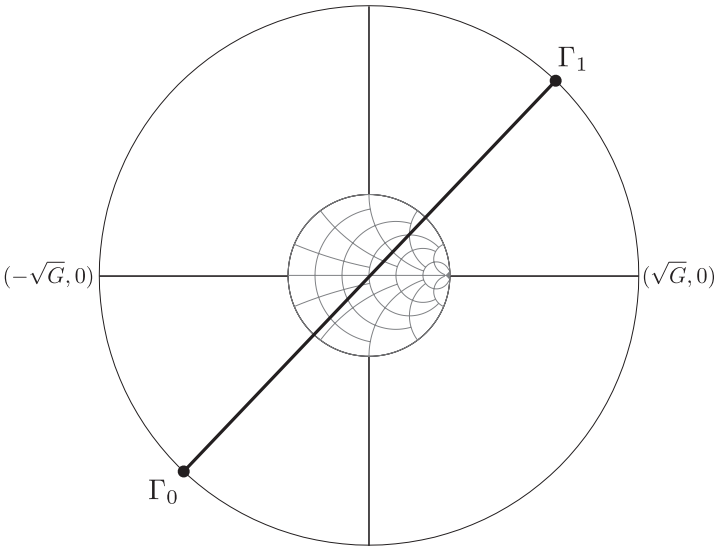

Figure 2.4: For a reflection amplifier tag that utilizes a phase shift modulator, Γ_0 and Γ_1 can both lie far from the unitary circle. Maximum distance between Γ_0 and Γ_1 can be achieved when these are diametrically opposed.

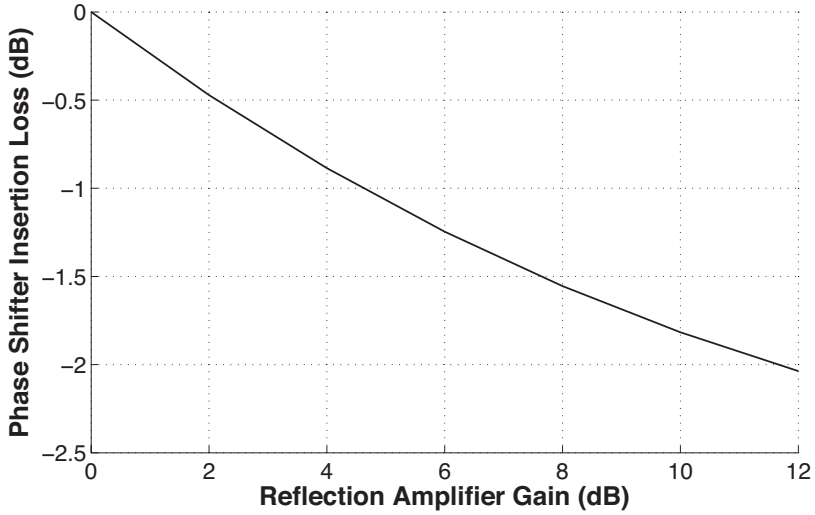

Figure 2.5: Maximum acceptable phase shifter loss for given reflection amplifier gain, to achieve tag SNR gain over conventional tags with load modulators.

acceptable insertion loss of the phase shifter is plotted versus the amplifier reflection gain. Intuitively, as the amplifier gain increases, the loss level that can be tolerated becomes higher. As an example, for an amplifier reflection gain of 10 dB, the maximum acceptable insertion loss is -1.82 dB.

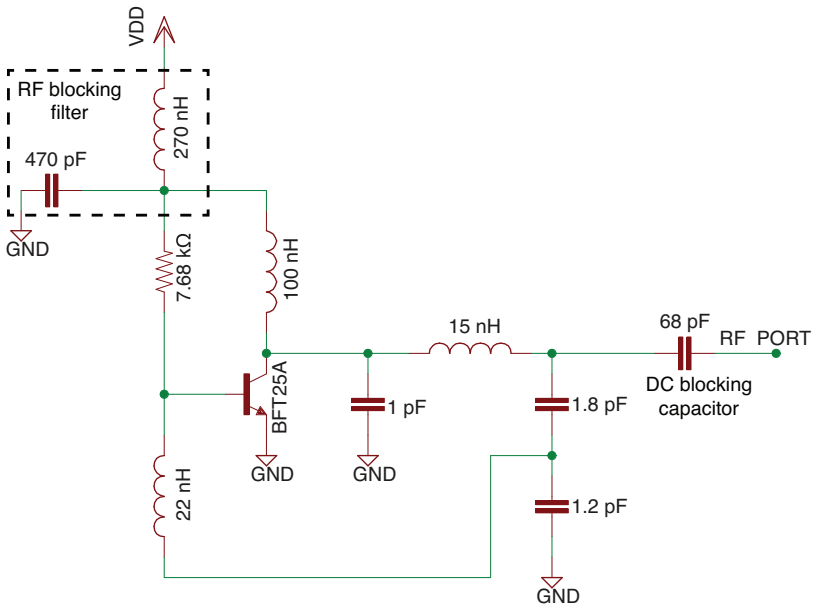

Figure 2.6: Reflection amplifier schematic: Negative resistance amplifier topology with a common input/output terminal (RF PORT). The amplifier is biased with a low DC voltage to prevent oscillations. An RF blocking filter is utilized at the bias point to prevent RF leakage to the DC supply.

2.2 Reflection Amplifier Design

The design of reflection amplifier circuits is similar to oscillator design, because the desired amplifier gain is obtained by generating a negative resistance without however fulfilling oscillating conditions. In this work, emphasis is placed in minimizing the dissipated power and maximizing the efficiency of the reflection amplifier, and for this reason its design was based on a Class-E oscillator topology. A Class-E oscillator is created by introducing appropriate feedback in a Class-E amplifier circuit which leads to a high DC-RF efficiency. In [75], an active antenna oscillator powered by a solar cell was proposed, based on the Class-E oscillator topology of [76]. The circuit had a 43% efficiency at 905 MHz for an output power of 2 mW. The device was biased at 1.5 V with a collector current of 3.2 mA. Harmonic balance simulation was used to ensure the oscillating condition and optimize the output power and efficiency of the circuit. This topology was used as a starting point in order to implement a reflection amplifier. The collector bias of the BFT25A device has

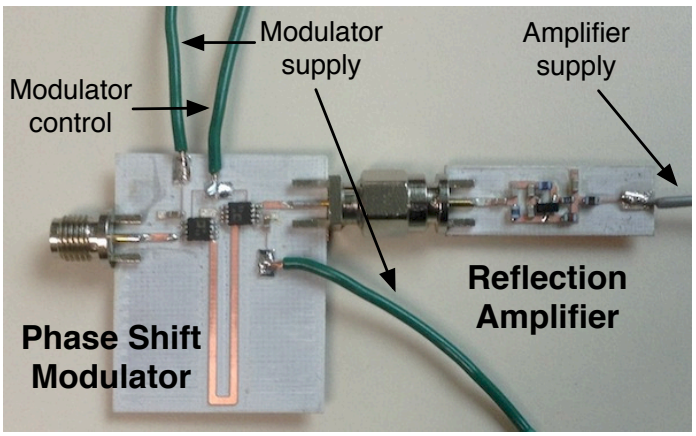

Figure 2.7: Fabricated prototypes. Left: phase shift modulator. Right: reflection amplifier.

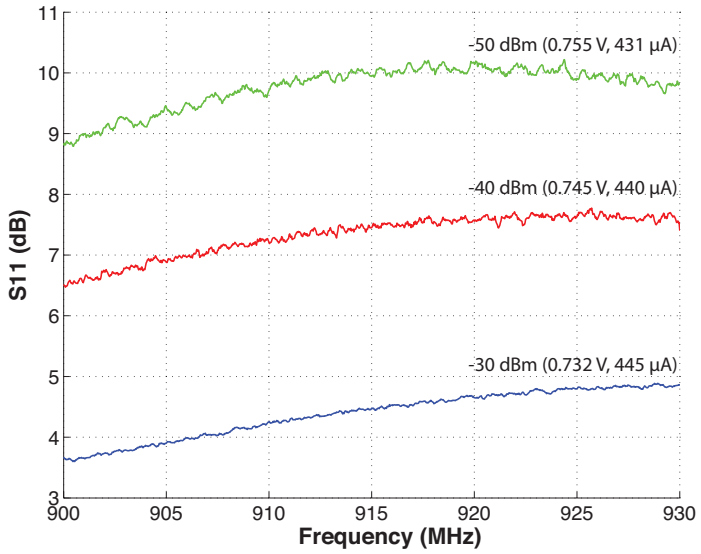

Figure 2.8: Reflection amplifier gain measurements for different input power levels and DC bias voltage values.

been reduced until the oscillation is extinguished while maintaining a negative resistance in order to ensure amplifier gain. The circuit schematic of the amplifier with the component values is shown in Fig. 2.6, while a photo of the fabricated prototype on Rogers RO4003C substrate is shown in Fig. 2.7. Because the amplifier is targeting very long-range applications (order of $50 \sim 100$ m, as in [1]), it has been tuned to maximize its gain at very low input power levels, below -30 dBm. The frequency region of operation is the ultra high frequency (UHF) industrial-scientific-medical (ISM) band of 900–930 MHz.

The reflection gain of the amplifier has been measured with a vector network analyzer

Table 2.1: Reflection Amplifier Consumption.

Input Power (dBm)	Bias Voltage (V)	Current Draw (μA)
-30	0.732	435
-40	0.745	440
-50	0.755	431
no input	0.745	306

(VNA) for several input power levels and bias voltages. The maximum bias voltage used is 0.755 V. In Fig. 2.8, the obtained reflection gain values (S_{11}) for different bias points and input power levels are shown. It is important to note that the input power levels shown in Fig. 2.8 correspond to the highest input power that can be injected to the amplifier for a given bias voltage without starting any oscillation; i.e. if this input power level is exceeded, an oscillation will occur. A maximum gain of 10.2 dB is achieved for an input power level of -50 dBm, when the amplifier is biased at 0.755 V. For lower input power levels, the reflection gain remains on the same level, while the measured current consumption is 431 μA, resulting in 0.325 mW of dissipated power (Table 2.1). This low power level could be supplied by low-cost solar cells, even in low light illumination conditions. For the same bias voltage and a higher input power level of -40 dBm, the gain will be slightly reduced by ~ 1-dB. During lab experiments, it was observed that at a power level of -40dBm a gain of more than 9 dB can be achieved, but spontaneous interference in the 900–930 MHz band will instantaneously increase the power injected to the amplifier, which starts oscillating. Such interference exists due to nearby RFID readers in the building and other active transmitters in the ISM band. However, in an interference-free environment (e.g. outdoor sensor network deployments, far from domestic infrastructure) a stable operation could be guaranteed. To immune the system from interference and eliminate the probability of starting an oscillation at -40 dBm, the bias voltage has been decreased to 0.745 V.[1] The maximum gain in this case is ~ 7.7 dB and the current consumption is 440 μA. For an input power level

[1]One solution to eliminate oscillation is to reset the bias of the amplifier once an oscillation is detected. This can be implemented by sensing the current which the amplifier draws, as the onset of oscillation is marked by an increase in the drain current and dissipation power of the amplifier.

of -30 dBm and an even more reduced bias voltage of 0.732 V the gain reaches 4.9 dB and the consumption is 445 μA. The consumption remains on the sub-milliampere region even for higher input power levels (up to 0 dBm); however, since the amplifier is optimized for low input power operation, the reflection gain for such power levels decreases significantly. Finally, it is noted that the quiescent current when no RF power is applied at the amplifier's input is 306 μA. Notice that while the input power increases, the amplifier experiences a gain compression. This effect is anticipated and it has been previously reported in [77].

2.3 Phase Shift Modulator Design

A phase shift modulator is designed as a 2-port device that selectively delays the signal by 90° between port 1 and port 2, or passes the signal from port 1 to port 2 with no delay. As expressed mathematically in Sec. 2.1, in round-trip the reflected signal will be shifted by 180° or 0°, achieving a BPSK modulation.

A delay line of total length $\lambda/4$ is designed in the Agilent ADS microwave software and simulated with Agilent Momentum, by including the substrate parameters. The line length of $\lambda/4$ at the center frequency of 915 MHz corresponds to a delay of 90°, compared to a zero-length line which corresponds to 0° (practically, on the order of $3 \sim 5^\circ$). For selecting between the zero-length line and the delay line, two single-pole double-throw (SPDT) switches are utilized (Fig. 2.9). The SPDT switches will introduce a slight phase change, which however does not affect the result, since the phase change introduced will be approximately the same for both paths. In that way, the delay line path will always be 90° shifted compared to the zero-length path.

The phase shift modulator is implemented on Rogers RO4003C double copper-clad laminate with dielectric constant $\epsilon_r = 3.55$ and loss tangent $\tan\delta = 0.0021$ (Fig. 2.7). The substrate thickness of 20 mil helps keeping the microstrip lines in reasonable widths on the order of 40 mils for 915 MHz. Two ADG918 SPDT switches are used, which are operated with microampere current consumption at 1.6 V. The switches have been tested

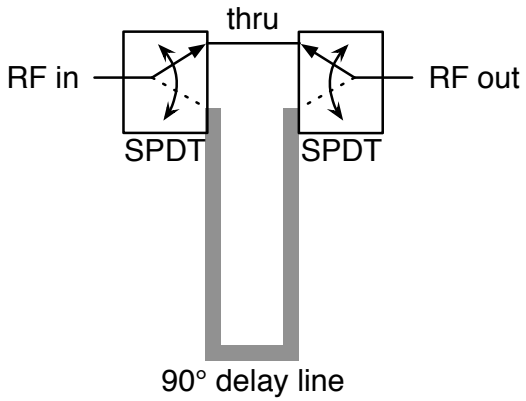

Figure 2.9: Delay line phase shift modulator block diagram.

for use with voltages on the order of $1 \sim 1.2$ V with a penalty of slightly higher insertion loss. The SPDTs are controlled by a single pin with a voltage that can be as low as 0.8 V.

The phase shifter transmission coefficient S_{21} is measured with a VNA to characterize the insertion loss and phase shifting in the two modulator states. In Fig. 2.10 it can be seen that $|S_{21}| \approx 0.79$, and the phase difference between the two states is $\sim 87^\circ$. The performance of the phase shift modulator is acceptable, while the transmission coefficient amplitude could be increased by using lower insertion loss switches. The return loss and the insertion loss for both modulator states can be seen in logarithmic scale in Fig. 2.11. The insertion loss for both states is approximately 2 dB (the two states differ by less than 0.1 dB), while the return loss is better than 21 dB for both states, indicating a good matching. Notice that from Fig. 2.5, for the reflection amplifier gain of 10.2 dB, the implemented phase shifter loss on the order of 2 dB is marginally acceptable. Nevertheless, the modulator is sufficient for the purpose of demonstrating the proof-of-concept of a reflection amplifier–phase shift modulator, and the insertion loss can be minimized by using lower-loss SPDT switches, and utilizing a single-board design to eliminate the SMA connector losses.

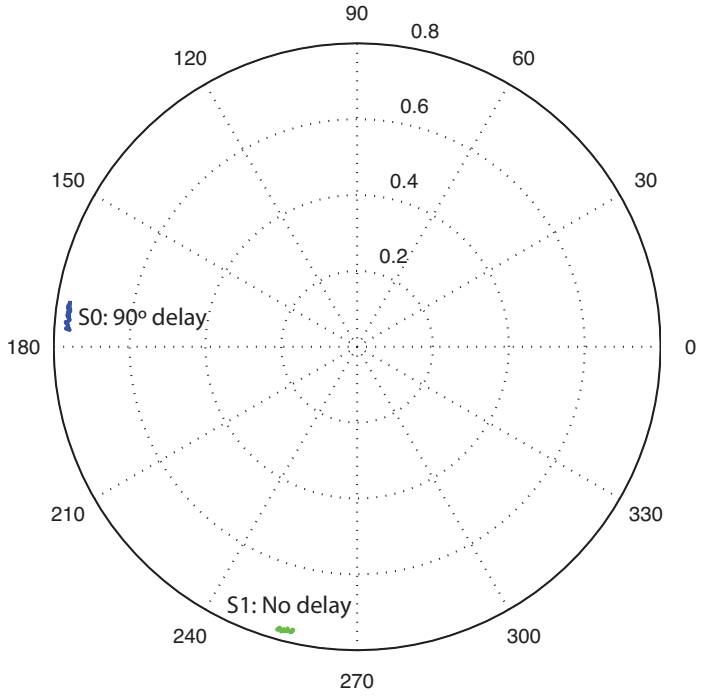

Figure 2.10: Transmission coefficient values of the implemented binary phase shift modulator. State 0: 90° delay. State 1: No delay.

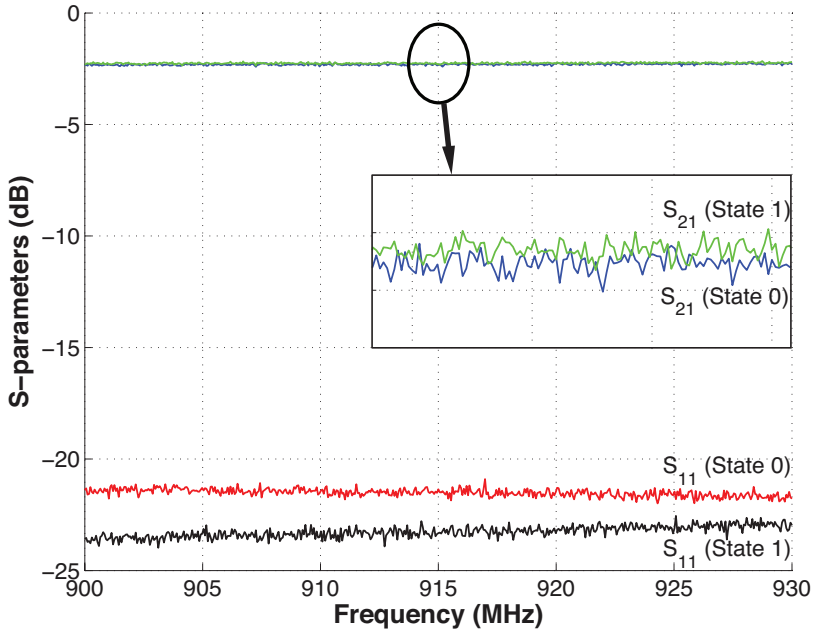

Figure 2.11: Measurements of phase shift modulator insertion loss and return loss for State 0 (90° delay) and State 1 (no delay).

2.4 System Characterization

The amplifier-phase shift modulator system is characterized by connecting the two elements (Fig. 2.7) and measuring the reflection coefficient for the two states. Fig. 2.12 shows the two reflection coefficients between 900 and 930 MHz for the amplifier-equipped tag, at a system input power of -40 dBm. At State 0, the reflection coefficient around 915 MHz is approximately $2\angle 15^\circ$, while at State 1, the reflection coefficient is approximately $2.1\angle 197^\circ$. The corresponding phase difference is 182°. The reflection coefficient amplitude variation across the 900–930 MHz band is on the order of 5%, which is sufficiently low for not affecting the antipodal constellation.

For comparison, a modulator-only tag has been tested, by shorting port 2 of the modulator and measuring the reflection coefficient at the two states. The points can be observed inside the unitary circle, having an amplitude of approximately 0.5 for State 0 and 0.6 for State 1. The phase difference of the two states is approximately 185°, corresponding to a BPSK constellation, with significantly lower SNR than the amplifier-equipped tag constellation. The reflection coefficient difference is plotted across the frequency band in Fig. 2.13 for the amplifier-equipped tag and the modulator-only tag. It can be seen that the amplifier-equipped tag achieves a $|\Delta\Gamma| \approx 4.1$ at 915 MHz, while the modulator-only tag achieves a $|\Delta\Gamma| \approx 1.1$.

Because the tag SNR is proportional to $|\Delta\Gamma|^2$ ([1, 24]), this translates to an SNR gain of the proposed tag over the modulator-only tag of $(4.1/1.1)^2 = 13.89 \rightarrow 11.43$ dB.

A setup consisting of a signal generator, a spectrum analyzer, and a circulator is used to test the backscattering of the implemented tag. The signal generator outputs a continuous wave (CW) at 915 MHz at -40 dBm. The tag is attached to the circulator so that it is excited by the generator CW, and its backscattering is captured by the spectrum analyzer.

Notice that measuring the carrier (central frequency) power level with and without an amplifier is not sufficient for characterization due to a) leakage of carrier power towards

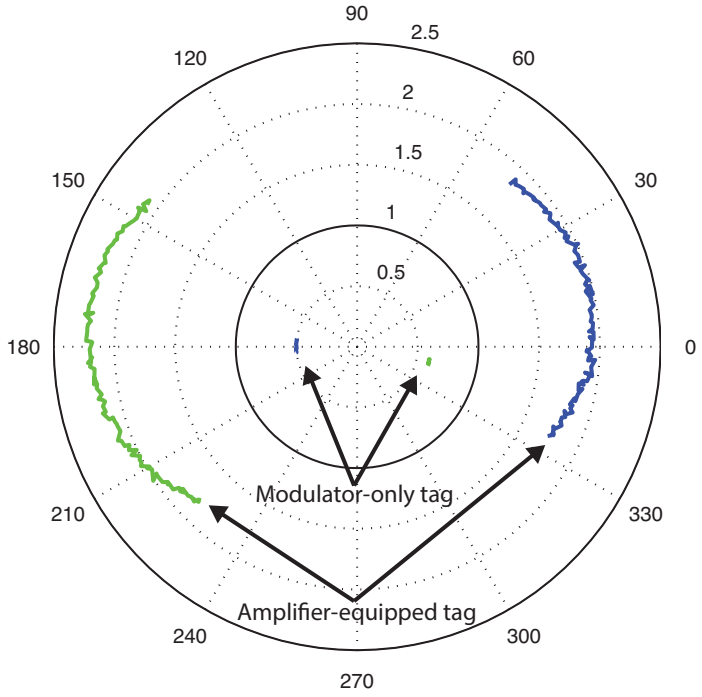

Figure 2.12: Measured antipodal reflection coefficient values (S_{11}) for the two tag modulation states (-40 dBm input power).

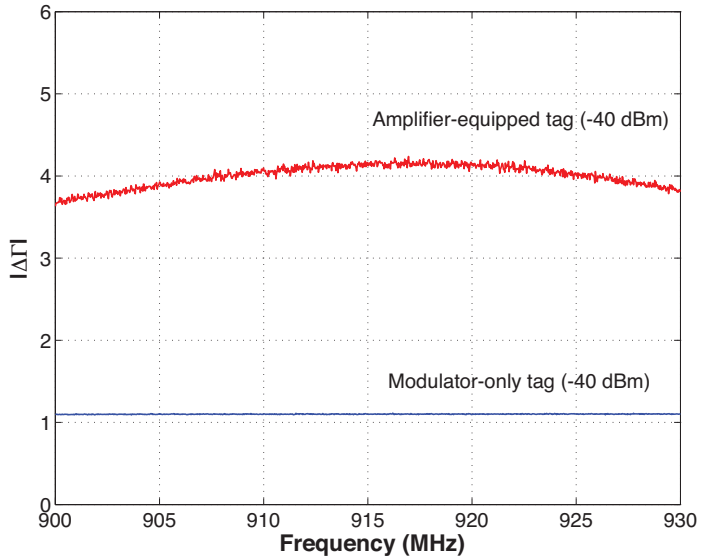

Figure 2.13: Comparison of reflection coefficient distance between the two tag states for a conventional modulator-only tag and an enhanced backscatter efficiency amplifier-equipped tag (-40 dBm input power).

the spectrum analyzer due to low circulator isolation, and b) the tag reflection at the carrier frequency may have such a phase that will create a destructive addition with the carrier

signal from the generator. This can lead to a wrong assessment of the system backscattering efficiency. For that reason, a square waveform is applied to the modulator control pin, switching between the 0° and 180° states with a rate of 250 kHz. Then, the tag backscatters a subcarrier 250 kHz away from the carrier (915.25 MHz), whose power level is measured without and with the amplifier. The power level of the subcarrier is directly related to $|\Delta\Gamma|^2$, as shown in the backscatter signal model in [1].

In Fig. 2.14 the spectra of the two cases can be seen. Notice that the subcarrier power level increases by 8 dB when the amplifier is present compared to the modulator-only case. This gives a proof of the system operation in low input power. The noise floor has been measured to increase by 1 dB on average. This results to a subcarrier SNR increase of $8 - 1 = 7$ dB. An SNR increase of 7 dB can have a significant impact in the tag demodulation by the reader. For example, in [1] it can be seen that for backscatter FSK, an SNR value of 0 dB corresponds to a BER value of 33%. In practice, this tag's information is lost by the reader. However, with a 7 dB increase in SNR, the BER drops down to 6%, which is significantly lower.

Furthermore, notice the low-frequency non-linearities around the carrier peak, which could cause interference if the tag signal spectrum is close to the carrier. In practice, the frequency region around the carrier is heavily affected by RF clutter due to low-frequency multipath reflections from the surrounding environments and electronics non-linearities [19]. The non-linearities introduced by the amplifier will further contribute to the RF clutter, which is a frequency region that should be avoided, due to the increased noise floor. Experiments in [9] have shown that the RF clutter might occupy a bandwidth of up to 100 kHz, and low-SNR tag signals in that frequency region may be completely 'hidden' from the reader. Properly selecting high subcarrier values can move the tag signal away from the carrier clutter, and guarantee efficient demodulation of low-SNR tag signals.

The theoretical range increase given an SNR increase of 8 dB can be approximated by using a far field two-ray path loss model that accounts for a line-of-sight path and a strong

reflection from the ground with the formula [78]

$$\mathrm{PL}(d) = G_T + G_R + 20\log_{10}\left(\frac{h_T\, h_R}{d^2}\right), \tag{2.19}$$

where G_T, G_R are the tag antenna and reader antenna gain values, respectively, h_T, h_R are the heights of the tag and reader antenna placement with respect to ground, and d is the distance between the tag and the reader. Considering a reader that transmits power P_T towards a tag placed at a distance of d_1 meters, the received backscattered power due to round-trip path loss is

$$P_R = P_T + 2\ \mathrm{PL}(d_1). \tag{2.20}$$

Consider also a tag with increased backscattered power by 8 dB that is placed d_2 meters away from the reader, and the reader receives the same backscattered power level

$$P_R = P_T + 8 + 2\ \mathrm{PL}(d_2). \tag{2.21}$$

Then it can be calculated that the tag-to-reader range relation between tag 1 and tag 2 is

$$d_2 \approx 1.26\ d_1, \tag{2.22}$$

i.e. a range increase of up to 26% can be achieved in *heavily-cluttered* environments with ground reflections.

The modulator-amplifier system has been interfaced with a microcontroller unit (MCU) to form a prototype tag and test the BER performance of the system and the range increase in a lab environment. The MCU generates a binary FSK waveform and outputs it in a digital pin as a varying frequency square pulse train. The voltage pulses drive the control input of the modulator, and thus the system alternates between Γ_0 and Γ_1 with two dif-

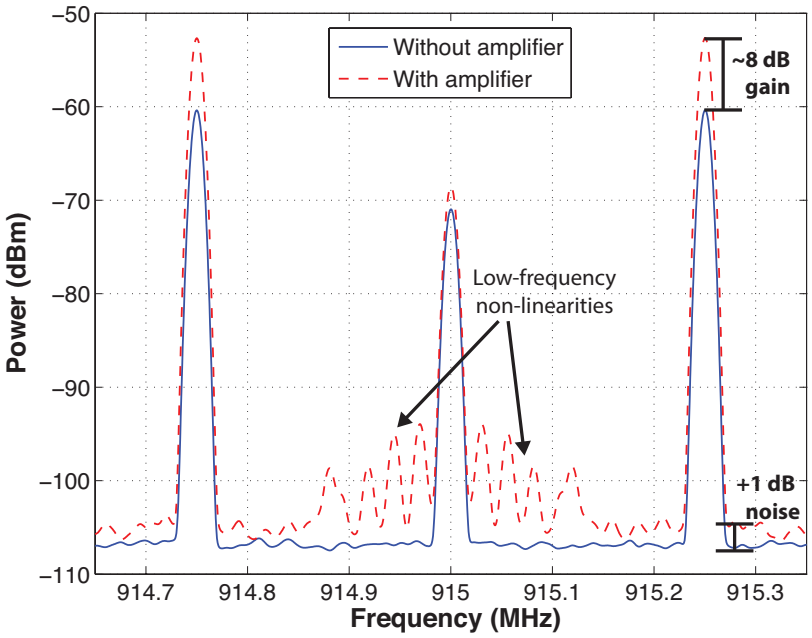

Figure 2.14: Measured backscattered spectrum of a conventional tag without a reflection amplifier and an amplifier-equipped tag. Both tags are excited with a 915 MHz CW and continuously switch between two modulation states with a 250 kHz rate, thus backscattering a 250 kHz subcarrier.

ferent rates F_0 and F_1, respectively. When the system is illuminated by a 915 MHz CW, this results in a backscattered signal spectrum with subcarriers at $\pm F_0$ and $\pm F_1$ (instead of just $\pm F_0$ as in Fig. 2.14). Both the prototype tag and the SDR reader utilize *omnidirectional* antennas with 3 dBi gain.The backscattered binary FSK signal is captured with a commodity software defined radio (SDR) and the digitized signal is processed on a host PC. The receiver implemented in software is based on the receiver in [1] and while decoding, it reports BER values of the demodulated backscatter signals. The modulator-only tag (MCU+phase shifter only) and the reader are moved away from each other, until an average BER value of 15% is reported. This corresponds to a distance of 1.39 m in the multipath- and interference-heavy lab environment with a power level of approximately -35 dBm induced at the tag antenna. When the reflection amplifier is interfaced to the tag, the BER drops to 6%, due to the increased backscatter signal SNR. The amplifier-enabled tag and SDR reader are moved away again, to achieve a BER value of 15%. The dis-

tance in that case is 1.7 m, corresponding to $\sim$30 cm range increase. Although this is an indicative example of a 22% increase, the range increase will be different in indoor and outdoor environments with different channel behavior and will vary in heavy interference environments such as buildings with RFID readers, GSM repeaters, etc. However, the lab environment example serves as the proof-of-concept for the range increase capabilities of the phase shifter-reflection amplifier architecture.

CHAPTER 3

BACKSCATTER FRONT-ENDS FOR INCREASED SPECTRAL EFFICIENCY

3.1 Arbitrary signal backscattering

In contrast with prior art, this work demonstrates mechanisms that allow for backscattering of arbitrary signals, instead of discrete-state signals, which are common in OOK/ASK tags. Instead of hard transistor switching, smooth backscattered pulses can be created, that feature a significantly reduced bandwidth occupancy (Fig. 3.1). This will greatly benefit sensor/RFID deployments, in terms of

- regulatory limitations: out-of-band emissions are suppressed with pulse shaping, and thus the developed techniques facilitate tag designs that conform to spectrum regulations,
- network density: reduced bandwidth-per-node has a direct impact on the number of nodes in the sensor/RFID network,
- communication scheme flexibility: generating and backscattering arbitrary waveforms enables the use of diverse communication schemes, datarates, modulation formats, and increased spectral efficiency,
- lower-complexity readers: readers require significantly lower sampling rate at the receiver chain, since the reduced backscatter signal bandwidth affects the minimum required sampling rate (Nyquist rate).

An extensive presentation is given of the concepts behind backscatter pulse shaping and arbitrary signal generation, the mechanisms and the front-end implementations, the processing required, as well as the power constraints of utilizing minimal, simple RF front-ends. Although these front-ends consist of a single active component, they can effectively

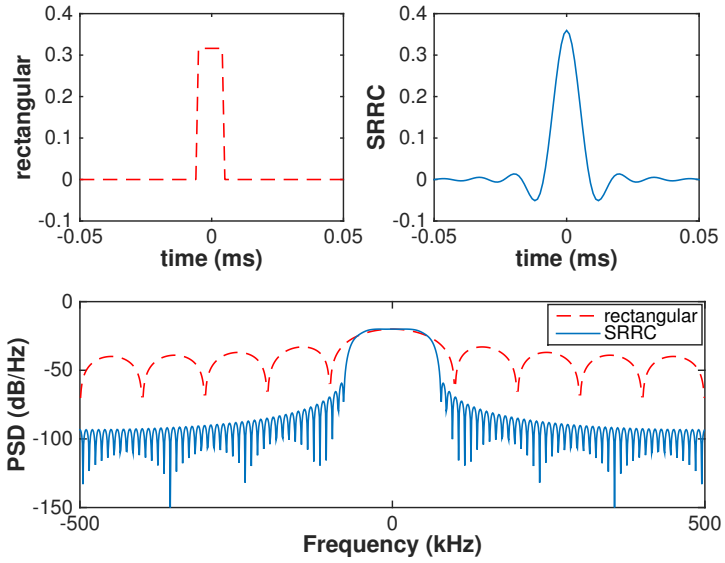

Figure 3.1: Spectrum comparison of 100 kbps rectangular pulses (typically used in backscatter radio) and square root raised cosine (SRRC) pulses of the same energy. Using pulse shaping for backscatter radio significantly reduces the required bandwidth per RFID tag or backscatter sensor.

break the limitations of rectangular waveforms and high bandwidth occupancy found in conventional RFID. Theory, simulations, and proof-of-concept front-end implementations and characterizations are offered with lab setups. Moreover, to showcase the practicality of the proposed designs on low-cost sensor nodes, the system is implemented on commodity microcontroller platforms. Despite these platforms' low computational ability, this work's mechanisms are successfully demonstrated to be fully operational, opening a new direction for low-power sensors and computational RFID. This work offers a *missing piece* to make backscatter radio a *complete* communication scheme, while maintaining an extremely lower energy footprint compared to active radio.

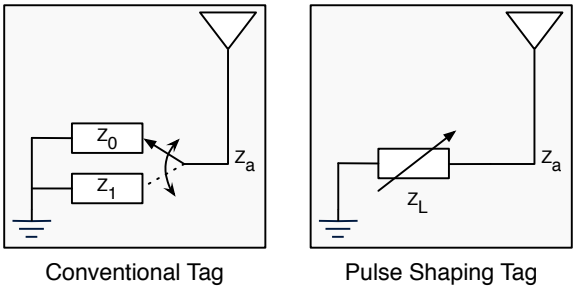

Figure 3.2: Left: Conventional tag switching between two discrete impedance loads. Right: Pulse shaping tag with variable impedance load.

3.2 Signal Model

The antenna-load system reflection coefficient for a backscatter modulator is [31, 73]:

$$\Gamma = \frac{Z_L - Z_a^*}{Z_L + Z_a}, \tag{3.1}$$

where Z_L and Z_a are the load and antenna impedance, respectively. From [1], the received complex baseband signal at the reader has the form

$$y_{\text{BB}}(t) = a_{\text{dc}} e^{j\phi_{\text{dc}}} + a_{\text{mod}} e^{j\phi_{\text{mod}}} \Gamma(t - \tau). \tag{3.2}$$

The term $a_{\text{dc}} e^{j\phi_{\text{dc}}}, a_{\text{dc}} \in \mathbb{R}, \phi_{\text{dc}} \in [0, 2\pi)$ corresponds to the compound unmodulated (dc) components of the received signal, i.e. the reader-emitted carrier continuous wave (CW) and the tag's unmodulated structural scattering. The term $a_{\text{mod}} e^{j\phi_{\text{mod}}}$ scales the received modulated tag signal by $a_{\text{mod}} \in \mathbb{R}$ and rotates it on the complex plane by a phase $\phi_{\text{mod}} \in [0, 2\pi)$. The terms $a_{\text{dc}} e^{j\phi_{\text{dc}}}$ and $a_{\text{mod}} e^{j\phi_{\text{mod}}}$ also include the impact of a static/quasi-static environment, i.e. channel attenuation and multipath effects. The tag signal is a direct function of Γ over time, delayed by a time constant τ that depends on the wireless channel propagation. Notice that all amplitude and phase terms are unknown at the reader, and the received baseband signal after timing recovery $y_{\text{BB}}(t + \tau)$ is equal to the tag-modulated signal $\Gamma(t)$ after unknown offsetting, scaling, and rotation on the complex plane.

Backscatter modulation is achieved when $\Gamma(t)$ changes over time, due to changes of the modulator's load impedance $Z_L(t)$ over time. Typically, backscatter load modulators utilize two load values for $Z_L(t)$ to achieve binary communication (Fig. 3.2-left). In that case, the baseband received signal $y_{\text{BB}}(t)$ features sharp changes between two values, i.e. the waveform consists of rectangular pulses. Notice that the two distinct received levels are, in general, complex. To transmit data at a data rate $R = 1/T$, where T is the bit duration, a very large bandwidth W (infinite in theory) is required in the frequency domain, since the Fourier transform of a rectangular pulse in time domain is a sinc in frequency domain (Fig. 3.1). However, according to the Nyquist inter-symbol interference (ISI) criterion in communication theory, the required bandwidth could be minimized to $W = R$ while maintaining reliable communication without ISI, which negatively affects bit detection [45]. A pulse typically used in active radio transceivers with limited bandwidth is the square root raised cosine (SRRC) pulse, which, at the expense of longer pulse duration features a significantly reduced main-lobe bandwidth [79]. The SRRC extends from $t_1 = -AT$ to $t_2 = AT$, where A is the *filter delay*, in contrary to a rectangular pulse that extends from $t_1 = -T/2$ to $t_2 = T/2$ (e.g. compare the pulse duration of a rectangular pulse and an SRRC pulse with $A = 5$ in Fig. 3.1-top). This reduces the required pulse bandwidth[1] to

$$W = \frac{1+a}{T}, \tag{3.3}$$

where $0 \leq a \leq 1$ is the roll-off factor that defines how fast the pulse spectrum decays in the frequency domain. The difference in spectrum occupancy for rectangular and SRRC pulses of the same energy is apparent in Fig. 3.1-bottom, where the power spectral density (PSD) of the two pulses is shown. Moreover, when using SRRC filters at the receiver to match-filter incoming SRRC pulses, the result is a raised cosine (RC) pulse, which satisfies the Nyquist ISI criterion, i.e. it is ISI-free, which increases the bit detection performance.

[1] "Bandwidth" here refers to the RF spectrum bandwidth around the modulation carrier (e.g. 900 MHz). The equivalent baseband spectrum would extend from dc to (1+a)/(2T) Hz.

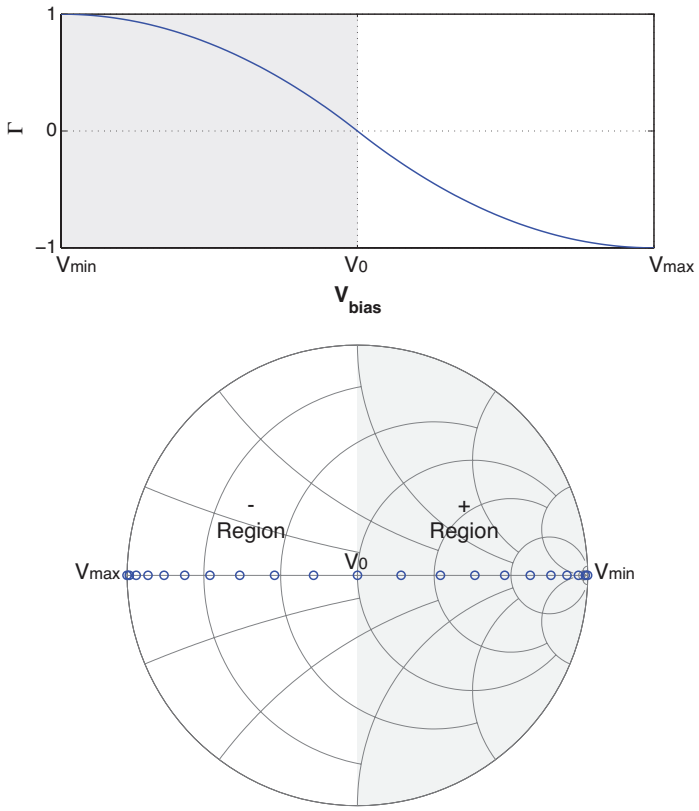

Figure 3.3: Reflection coefficient of (3.4) as a function of bias voltage in linear form and impedance representation.

Therefore, it is appealing to be able to generate SRRC pulses or other arbitrary waveforms with smooth envelopes (e.g. Gaussian pulses [45]) with a simple backscatter front-end to significantly suppress the signal spectral sidelobes, or generate multi-level waveforms to achieve amplitude modulation schemes such as M-ary pulse amplitude modulation (M-PAM), or generate arbitrary waveforms for other modulation schemes (e.g. sinusoids for analog frequency modulation (FM) or digital frequency-shift keying (FSK)). As discussed in the following sections, this can be achieved without the need of high-complexity electronics, but rather with a single active element front-end that continuously varies the antenna load in a continuous way.

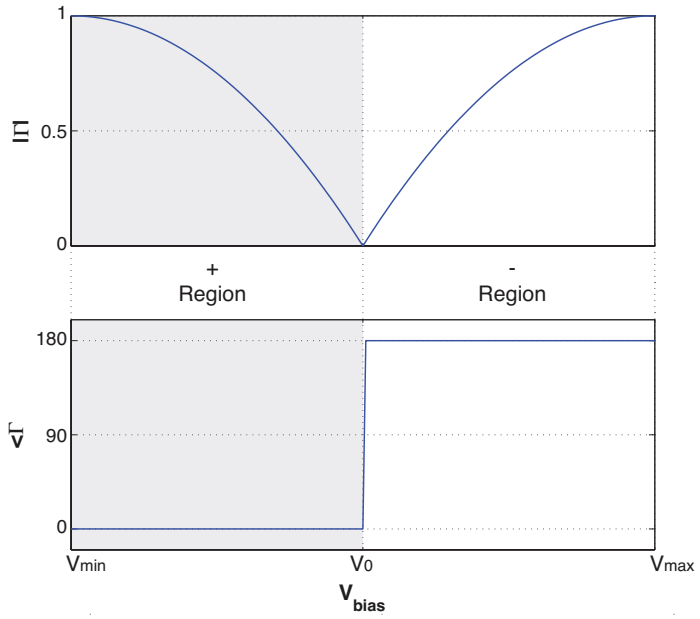

Figure 3.4: Reflection coefficient of (3.4) decomposed to magnitude and phase components, defining a positive and a negative reflected signal region.

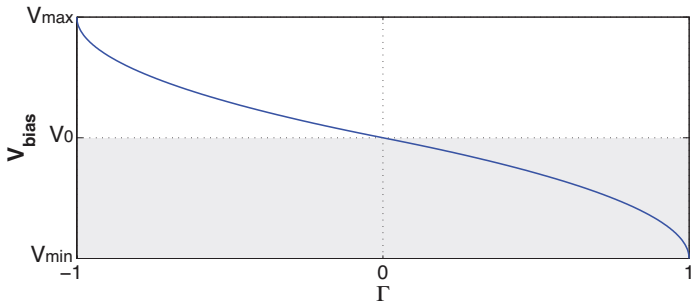

Figure 3.5: Inverted function of (3.6) providing the required bias voltage to achieve a certain reflection coefficient value.

3.3 Continuous Load Variation

The principles described in this section can be applied to any antenna that is complex-valued or real-valued, as well as any varying load that is complex-valued or real-valued, according to the general form of (3.1). However, without loss of generality, and to make the quantities easy to visualize, a purely resistive load $Z_L = R(V_{\text{bias}})$ controlled by a bias voltage V_{bias} and an antenna impedance $Z_a = 50\ \Omega$ are assumed. Then the antenna-load

reflection coefficient is

$$\Gamma(V_{\text{bias}}) = \frac{R(V_{\text{bias}}) - 50}{R(V_{\text{bias}}) + 50}. \tag{3.4}$$

and it is a real quantity with $1 \geq \Gamma(V_{\text{bias}}) \geq -1$. Let V_{min} be a low voltage level for which $\Gamma(V_{\text{min}}) = 1$, i.e. the antenna load acts as an open circuit ($R \to \infty$). Similarly, let V_{max} be the voltage level that turns the load to a short circuit ($R = 0\ \Omega$), i.e. the reflection coefficient is $\Gamma(V_{\text{max}}) = -1$. Moreover, let V_0 be the voltage that minimizes the reflection coefficient magnitude $|\Gamma(V_0)| = 0$, which occurs at $R = 50\ \Omega$.

The reflection coefficient as a function of the bias voltage is shown in Fig. 3.3 in linear scale and on a Smith chart, where it can be seen that reflection coefficient variations close to the edges of the Smith chart (high return loss) are more "dense", in contrast with the ones close to the chart's center, for equidistant variations of the bias voltage. The grey regions of the linear graph and the Smith Chart correspond to positive reflected signals and the white regions correspond to negative reflected signals. Assuming an incident RF signal to the load, a positive or negative voltage of any level between -1 and +1 can be reflected back by applying the appropriate bias value.[2]

The reflection coefficient can be decomposed to its magnitude and phase components as shown in Fig. 3.4. It can be seen that the reflection coefficient values can be split to one "positive" region and one "negative" region. Notice that the point of sharp transition in phase coincides with the point where the reflection coefficient amplitude is minimized. This decomposition is useful because even if there is a phase rotation of $\Gamma(V_{\text{bias}})$, the amplitude function will remain the same, and the two regions can still be defined, since they will have

[2]Work in [80] has offered designs that backscatter signals with reflection coefficient values $|\Gamma| > 1$. Those designs involve negative-resistance loads to amplify-and-reflect incident signals; this work assumes passive loads only, confined within the unitary circle of the Smith chart.

opposite signs. The breakpoint can be found by

$$V_0 = \arg\min_{V_{\text{bias}}} |\Gamma(V_{\text{bias}})|. \tag{3.5}$$

Then the positive region will be the $\Gamma(V_{\text{bias}})$ values for which $V_{\text{bias}} < V_0$ and the negative region will be the $\Gamma(V_{\text{bias}})$ values for which $V_{\text{bias}} > V_0$. Even if the definition of the positive and negative values is inverted, it does not alter the pulse shaping principle, since the opposite phase will just contribute an extra π radians in the already-unknown phase at the receiver (ϕ_{mod} in (3.2)). After this decomposition it becomes apparent that any signal level (from 0 to 1) can be generated with two possible signs, making it possible to generate arbitrary waveforms.

To generate an arbitrary signal, the required bias voltage to yield the corresponding reflection coefficient is needed. This involves inverting the function $\Gamma(V_{\text{bias}})$, i.e. finding the function

$$V_{\text{bias}}(\Gamma), \quad \text{for which: } \Gamma(V_{\text{bias}}(\Gamma)) \equiv \Gamma(V_{\text{bias}}). \tag{3.6}$$

Note that V_{bias} and Γ denote scalar values, while $V_{\text{bias}}(\cdot)$ and $\Gamma(\cdot)$ denote scalar functions. From Fig. 3.3-top, it can be seen that $\Gamma(V_{\text{bias}})$ is a 1-1 function, and thus invertible; the inverse $V_{\text{bias}}(\Gamma)$ function is shown in Fig. 3.5.

Assume we need to transmit an arbitrary pulse $x(t)$, e.g. the one shown in Fig. 3.6-left. The amplitude level of the pulse is first confined in the interval $[-1, 1]$ with the normalization

$$\tilde{x}(t) = \frac{x(t)}{\max|x(t)|}, \tag{3.7}$$

to yield the pulse shown in Fig. 3.6-center, which is expressed in reflection coefficient-domain values (-1 to 1). By using the $V_{\text{bias}}(\Gamma)$ function in Fig. 3.5, $\tilde{x}(t)$ can be translated to

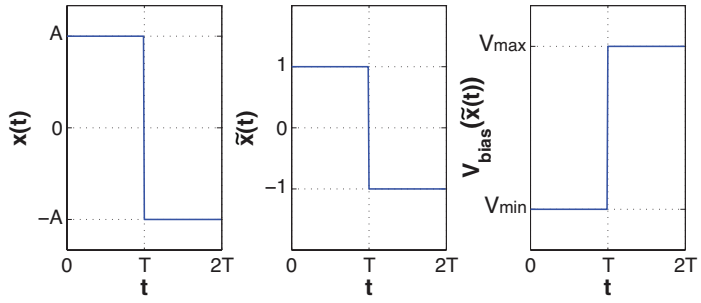

Figure 3.6: Left: pulse to be transmitted. Center: transformation to reflection coefficient values (applying (3.7)). Right: transformation to required bias voltage (applying (3.8)).

the bias voltage required to yield this reflection coefficient variation over time. The result is the bias voltage function over time

$$V_{\text{bias}}(\tilde{x}(t)) = V_{\text{bias}}(\Gamma)|_{\Gamma=\tilde{x}(t)} \tag{3.8}$$

shown in Fig. 3.6-right.

3.4 Pulse Shaping Front-end Design

Two front-end designs are presented, one comprising a PIN diode, and one comprising a FET transistor switch. Both components have a voltage-controlled resistance behavior and their impedance varies in a continuous way, instead of sharply transitioning between two values, thus making them ideal for pulse shaping front-end design. However, pulse shaping front-ends could be implemented with *any* nonlinear element or elements that show a controlled impedance behavior, not necessarily limited to voltage-controlled resistance. Moreover, in the subsequent Sec. 3.8, more options for pulse shaping front-ends are discussed, involving analog RLC filters. All presented front-ends try to exploit the full range of impedance values on the Smith chart so that they maximize the backscattered signal energy and increase the detection performance at the reader. However, this implies that at the beginning or end of every symbol, the modulator is always in a reflective state, which is challenging for RF tags that employ harvesters for powering and/or energy storage. Work

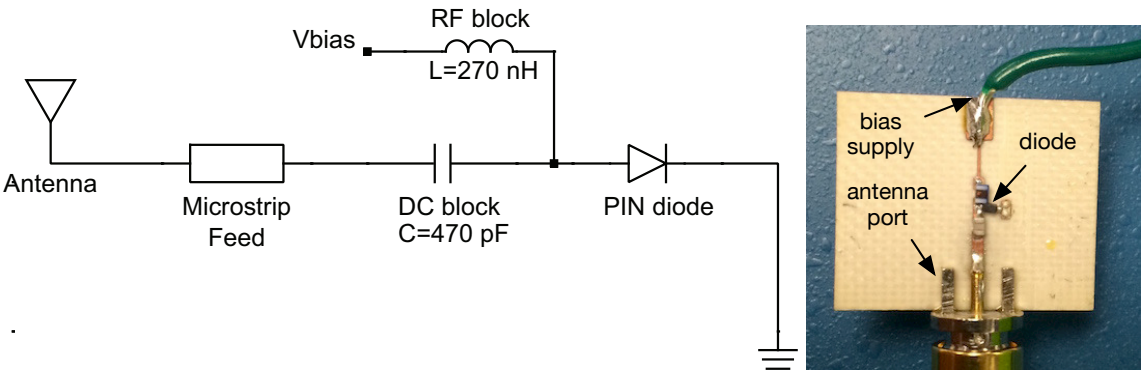

Figure 3.7: Pulse shaping front-end schematic (left) and prototype (right).

in [24] has offered solutions for hybrid 3-state front-ends that can accommodate RF harvesters along with modulators that are fully-reflective for uncompromised communication. The concepts of that work can be applied in conjunction with the pulse shaping modulators presented in this section.

3.4.1 PIN Diode Front-end

A first choice for a front-end with a single active element that features a voltage-controlled resistance behavior is a diode. Specifically, a PIN diode (Skyworks SMP1302-079LF) targeted to variable attenuator applications is essentially an RF-thru with S_{21} attenuation that depends on the applied bias voltage.

The PIN diode is terminated to a short circuit to achieve maximum reflection with a negative sign $\Gamma_{\text{short}} = -1$ when the PIN diode is fully biased and maximum reflection with a positive sign when the diode is not biased and behaves as an RF open $\Gamma_{\text{open}} = 1$. A dc bias network is connected to the diode's anode with an RF-block inductor in the bias voltage path and a dc-block capacitor in the RF path (Fig. 3.7-left). The front-end is analyzed with Keysight advanced design system (ADS) utilizing a non-linear SPICE model for the diode, manufacturer models for the lumped components, and full-wave simulation of the PCB layout and the feeding microstrip line. The simulated $\Gamma(V_{\text{bias}})$ is shown in Fig. 3.8. Compared to the theoretical plot of Fig. 3.3, the curve shows a phase shift and a small offset

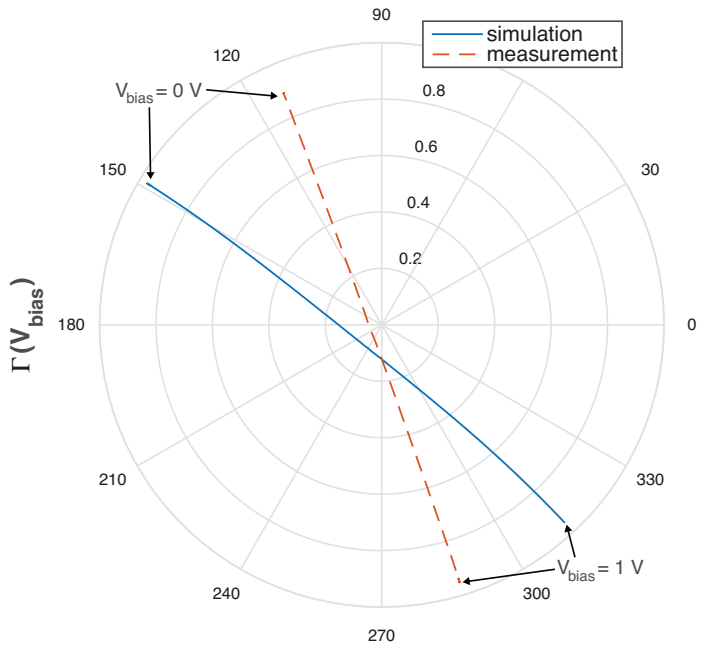

Figure 3.8: Reflection coefficient versus bias voltage level (0–1 Volts) for PIN diode front-end (913 MHz).

from the center of the polar plot, due to a) the phase introduced by the microstrip feeding line and b) parasitics of the PIN diode. These practically do not affect the received signal at the reader, since the offset will contribute to the unmodulated dc term of (3.2), and the phase shift will be absorbed by the already-present phase term $e^{j\phi_{\text{mod}}}$ that rotates $\Gamma(t-\tau)$ on the complex plane.

The front-end is implemented on a double copper-clad Rogers RO4003C laminate with a dielectric constant $\epsilon_r = 3.55$, loss tangent $tan\delta = 0.0021$, and substrate thickness 20 mil (Fig. 3.7-right) and is characterized using an automated setup of continuous bias voltage sweeping with a voltage source and S-parameter measurements with a vector network analyzer (VNA) (Fig. 3.9. The measured reflection coefficient for a bias voltage range of 0 to 1 Volts features a similar behavior with the simulated data (Fig. 3.8), with an introduced phase shift (due to the phase introduced by the SMA connector) which, as mentioned previously, does not affect the signal detection at the reader.

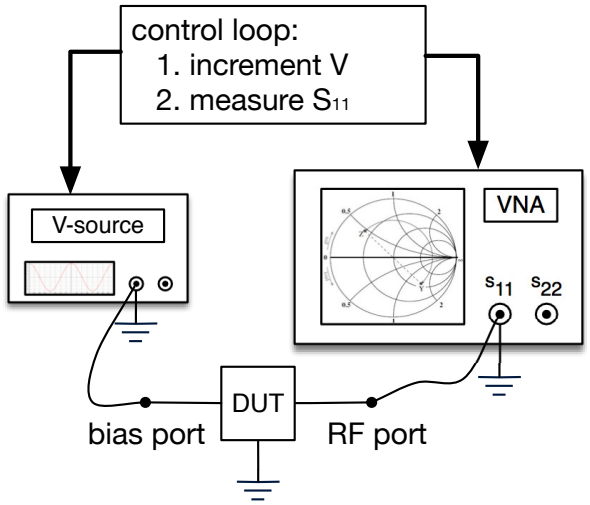

Figure 3.9: Front-end characterization setup.

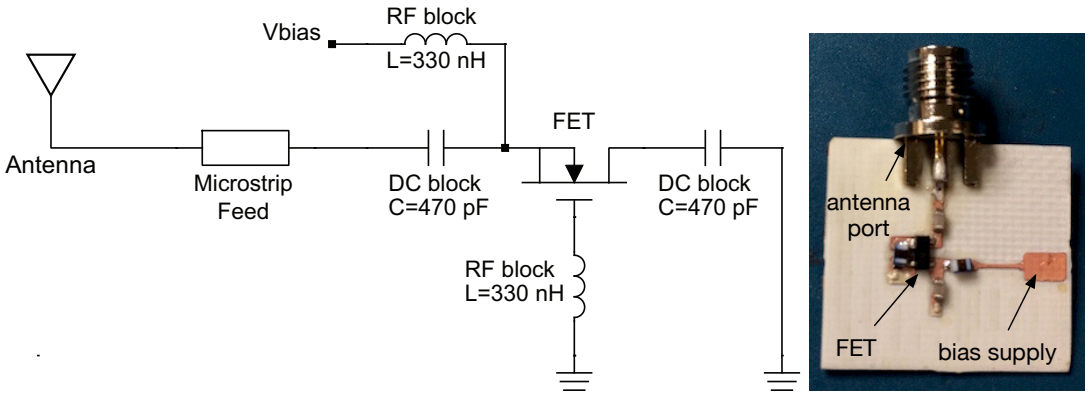

Figure 3.10: FET implementation of pulse shaping front-end schematic (left) and prototype (right).

3.4.2 FET Switch Front-end

A similar attenuation mechanism is also implemented with a field-effect transistor (FET), since it features a drain–source resistance variation that depends on the gate voltage. A front-end has been built with an RF FET (NXP BF1118) which primarily targets switching applications and has been used in previous works as a switch for binary backscatter modulation by biasing to a low or a high voltage level [20, 24] . However, when sub-biased, the FET switch acts as a voltage-controlled variable impedance and can be used for pulse shaping, since the source-drain resistance changes with the gate-source voltage (Fig. 3.10).

A n-channel depletion-type MOSFET terminated with a short is used as a variable-attenuation thru line. Since the transistor is biased with negative gate-source (V_{GS}) voltage levels, the gate is grounded ($V_{\text{G}} = 0$) and the bias voltage is applied to the FET's source ($V_{\text{S}} = V_{\text{bias}}$). Apart from the dc-block capacitor and RF-block inductor used for the biasing network, an extra dc-block capacitor is used between the FET's drain and the ground short, to prevent dc current flow from the source to the ground when the source-drain channel is 'on'. The capacitor value is high (470 pF) so that it still acts as an RF-short, not affecting the front-end's pulse shaping operation.

The FET front-end is implemented on RO4003C laminate and characterized with the measurement setup of Fig. 3.9. The measured $\Gamma(V_{\text{bias}})$ is shown in Fig. 3.11 for voltage levels from 0 to 2 Volts. It can be seen that a continuous variation of the reflection coefficient is achieved when changing the bias voltage, although the reflection coefficient variation does not cover the whole Smith Chart from end to end. This is due to the insertion loss of the FET switch at the "on" state, and will affect the backscattered signal in terms of lower reflected power. Although there is an offset from the center of the polar plot, a scaling, and a phase shift, these do not affect the signal demodulation at the reader, and proper processing steps shown in Section 3.5 can guarantee the exploitation of the full range of reflection coefficient values. Also, the effect of the small curvature close to the value $V_{\text{bias}} = 0$ will be negligible as shown in the measurements section.

3.5 Processing and Measurements

The steps required to use a pulse shaping-capable front-end for arbitrary signal generation are summarized in Fig. 3.12. After characterizing a pulse shaping-capable front-end with the setup of Fig. 3.9, the $\Gamma(V_{\text{bias}})$ function has been obtained and a series of offline processing steps are required that need to be run once. This is also facilitated by the fact that there is a very small variation of the reflection coefficient values for the UHF band from 850 MHz to 950 MHz. Fig. 3.13 shows the measured Γ values for both front-ends

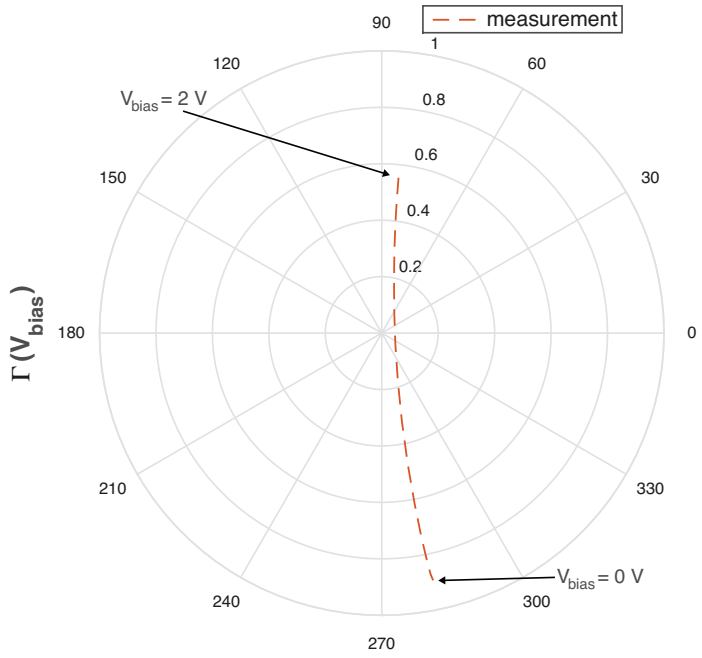

Figure 3.11: Reflection coefficient versus bias voltage level (0–2 Volts) for FET front-end (913 MHz).

in the two edge cases of 0 V/1 V for the PIN and 0 V/2 V for the FET. The calculated standard deviation is between 0.028 and 0.05 for all cases within 850–950 MHZ, which makes the front-ends suitable for broadband operation in the whole UHF band. Within the 900–928 MHz RFID band the deviation is between 0.008 and 0.015 for all cases. The result of the offline processing is used by the backscatter communicator to transmit pulse shaped signals.

3.5.1 Offline Processing

The following processing steps are intended to be run offline after the front-end characterization. They involve calculations that would take part on a computer and the individual steps are straightforward to implement in MATLAB or other software. It is noted that the steps need to be run once, assuming negligible behavior differences of the non-linear components due to manufacturer tolerances and variations.

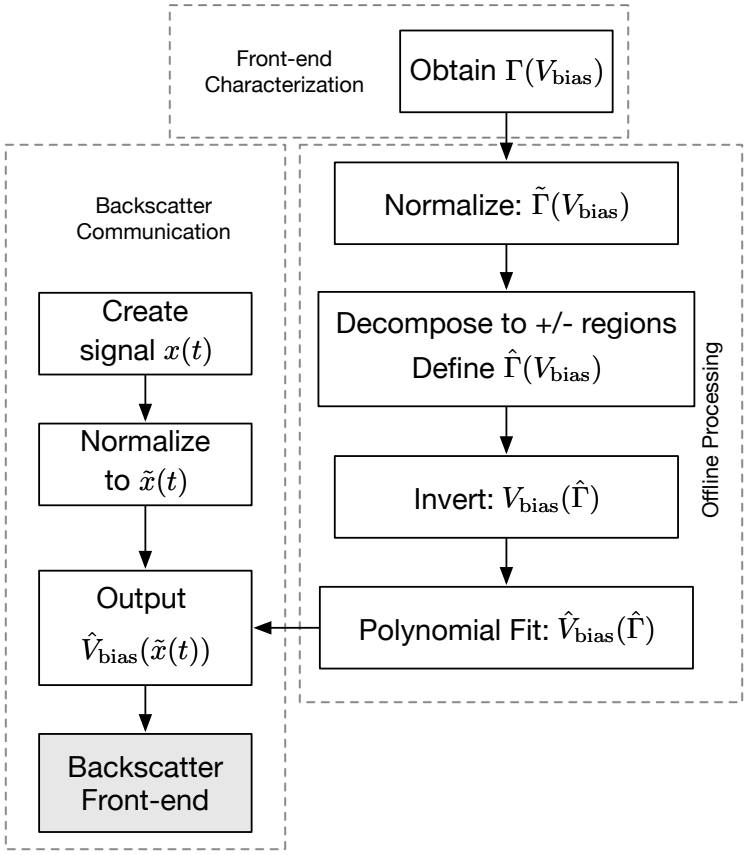

Figure 3.12: Characterization, processing, and communication steps.

Normalization

The measured $\Gamma(V_{\text{bias}})$ function for actual front-end implementations will differ from the function shown in Fig. 3.3, as it is going to be affected by offsetting, scaling, and rotation. That means that for an ideal function $\Gamma_{\text{ideal}}(t)$ that has the form of Fig. 3.3 and extends from -1 to 1, an actual front-end function $\Gamma(t)$ has the form

$$\Gamma(t) = s\,\Gamma_{\text{ideal}}(t) + c, \tag{3.9}$$

where $s, c \in \mathbb{C}$, i.e. the scaling factor s will scale down *and* rotate the $\Gamma_{\text{ideal}}(t)$ function on the complex plane, and the offset factor c will move the scaled-and-rotated function $s\Gamma_{\text{ideal}}(t)$ towards *any* direction on the complex plane. For such a function, the baseband

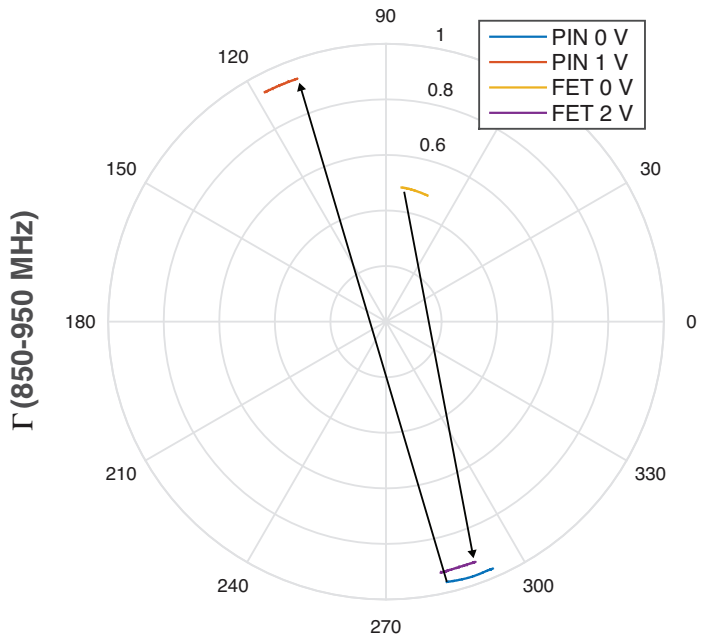

Figure 3.13: Measured reflection coefficient variation across 850–950 MHz band for PIN and FET front-ends.

received signal at the reader will be

$$\begin{aligned} y_{\text{BB}}(t) &= a_{\text{dc}}e^{j\phi_{\text{dc}}} + a_{\text{mod}}e^{j\phi_{\text{mod}}}\Gamma(t-\tau) \\ &= a_{\text{dc}}e^{j\phi_{\text{dc}}} + a_{\text{mod}}e^{j\phi_{\text{mod}}}(s\,\Gamma_{\text{ideal}}(t-\tau)+c) \\ &= a'_{\text{dc}}e^{j\phi'_{\text{dc}}} + a'_{\text{mod}}e^{j\phi'_{\text{mod}}}\Gamma_{\text{ideal}}(t-\tau), \end{aligned} \tag{3.10}$$

where $a'_{\text{dc}}e^{j\phi'_{\text{dc}}} = a_{\text{dc}}e^{j\phi_{\text{dc}}} + c\;a_{\text{mod}}e^{j\phi_{\text{mod}}}$ is the new compound unmodulated DC term and $a'_{\text{mod}}e^{j\phi'_{\text{mod}}} = s\;a_{\text{mod}}e^{j\phi_{\text{mod}}}$ is the scaling and rotating term of the modulated signal $\Gamma_{\text{ideal}}(t-\tau)$. The signal of (3.10) is of the same form with (3.2), since the DC terms and scaling terms are unknown at the reader. Therefore, any offset, scaling, or rotation of the reflection coefficient does not affect the reader processing.

Since offsetting, scaling, and rotation do not affect reader processing, it is convenient to normalize the measured reflection coefficient values to the form of Fig. 3.3 so that the subsequent steps treat reflection coefficient functions for any front-end in the same way.

The normalization operation is

$$\tilde{\Gamma}(V_{\text{bias}}) = \frac{\Gamma - \hat{c}}{\hat{s}} \triangleq \frac{\hat{s}^{*}\Gamma(V_{\text{bias}}) - \hat{s}^{*}\hat{c}}{|\hat{s}|^{2}}, \tag{3.11}$$

where $\hat{c}$ is the offset factor estimate

$$\hat{c} = \frac{\Gamma(V_{\text{max}}) + \Gamma(V_{\text{min}})}{2}, \tag{3.12}$$

$\hat{s}$ is the scaling factor estimate

$$\hat{s} = \frac{\Gamma(V_{\text{max}}) - \Gamma(V_{\text{min}})}{2}, \tag{3.13}$$

and $\hat{s}^{*}$ is the complex-conjugate of $\hat{s}$. In Fig. 3.14-top the measured reflection coefficient values of the PIN front-end can be seen for bias voltages from 0.4 to 0.82 Volts. The reason for truncating the 0–1 Volts measurements interval to 0.4–0.82 Volts is that practically any voltage level between 0–0.4 Volts yields $\Gamma = 0.9$ and any level between 0.82–1 Volts practically yields $\Gamma = -0.9$. In Fig. 3.14-bottom the normalized reflection coefficient values for the same voltage interval can be seen. Notice how the polar plot and the magnitude of the reflection coefficient are of the same form with the theoretical Fig. 3.3 and Fig. 3.4.

Decomposition to positive and negative regions

As discussed in Section 3.3, the reflection coefficient function is decomposed to a positive and to a negative region. This involves estimating the breakpoint

$$\hat{V}_0 = \arg\min_{V_{\text{bias}}} |\tilde{\Gamma}(V_{\text{bias}})| \tag{3.14}$$

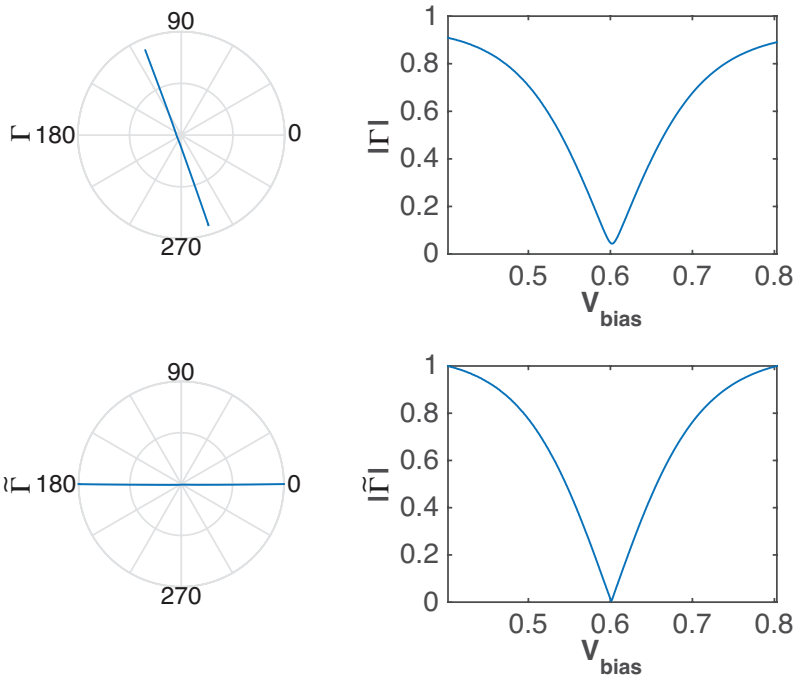

Figure 3.14: Normalization of reflection coefficient values. Measured data from PIN diode used for processing.

and then defining the function

$$\hat{\Gamma}(V_{\text{bias}}) = \begin{cases} |\tilde{\Gamma}(V_{\text{bias}})|, & V_{\text{bias}} \leq \hat{V}_0, \\ -|\tilde{\Gamma}(V_{\text{bias}})|, & V_{\text{bias}} > \hat{V}_0. \end{cases} \tag{3.15}$$

Function Inversion

The function $\hat{\Gamma}(V_{\text{bias}})$ with the two positive/negative regions is 1–1 and is inverted to obtain $V_{\text{bias}}(\hat{\Gamma})$, which can be used as a lookup function to translate signals in reflection coefficient-domain values (in $[-1,\ 1]$) to corresponding bias voltage levels.

Polynomial Fitting

A polynomial fitting step follows, which describes function $V_{\text{bias}}(\hat{\Gamma})$ with a small number of coefficients, and smooths out signal discontinuities and measurement noise. The coefficients can be used to store the function in a low-memory device such as an MCU for later

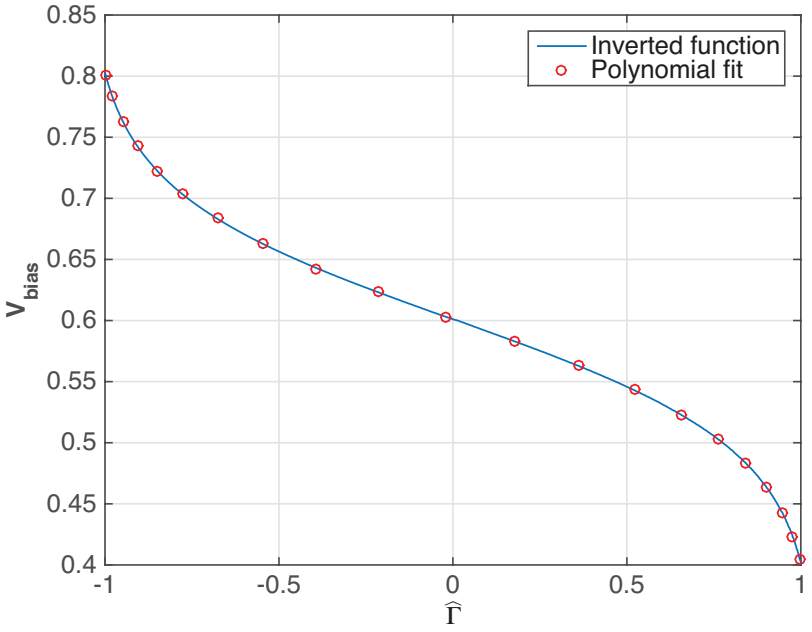

Figure 3.15: Inverted $V_{\text{bias}}(\hat{\Gamma})$ function and polynomial-fitted $\hat{V}_{\text{bias}}(\hat{\Gamma})$ points. Measured data from PIN diode used for processing.

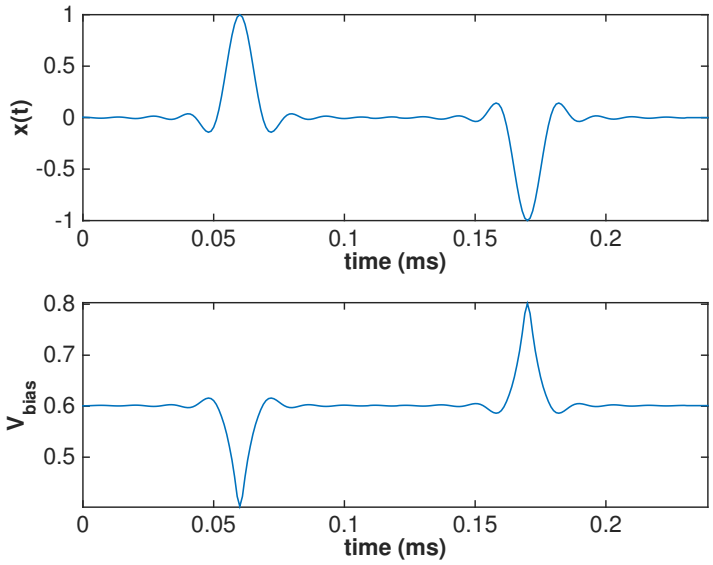

Figure 3.16: Two SRRC pulses (one positive and one negative) in reflection coefficient and bias voltage representation.Measured data from PIN diode used for processing.

evaluation, or evaluate the function in predefined steps of $\hat{\Gamma}$ and store the resulting values in a lookup table (LUT). In Fig. 3.15, the inverted function $V_{\text{bias}}(\hat{\Gamma})$ is plotted along with its evaluated polynomial-fit function $\hat{V}_{\text{bias}}(\hat{\Gamma})$.

3.5.2 Backscatter Communicator

The steps associated with the backscatter communication (Fig. 3.12), are intended to run real-time on a tag that either generates bits based on dynamic information (e.g. sensor data) or recalls static bits from its memory (e.g. identification data). The following steps are intended to run in a loop:

Signal creation

The communicator is generating an arbitrary signal $x(t)$ for transmission, e.g. a positive and a negative SRRC pulse in Fig. 3.16-top.

Normalization

The signal $x(t)$ is normalized to $\tilde{x}(t)$ according to (3.7), to constrain it to reflection coefficient-domain values, from -1 to 1.

Voltage output

The fitted function $\hat{V}_{\text{bias}}(\hat{\Gamma})$ is used to translate the signal $\tilde{x}(t)$ to the required voltage levels. This can be done by evaluating a N-degree polynomial with

$$\hat{V}_{\text{bias}}(\tilde{x}) = p_N \tilde{x}^N + p_{N-1}\tilde{x}^{N-1} + \ldots + p_1 \tilde{x} + p_0, \tag{3.16}$$

where $p_n,\ n \in N$ are the fitted polynomial coefficients obtained during the offline processing step B-4. The signal $\hat{V}_{\text{bias}}(\tilde{x}(t))$ is output to bias the pulse shaping RF front-end. Fig. 3.16-bottom shows the bias voltage levels required to backscatter the pulses of Fig. 3.16-top.

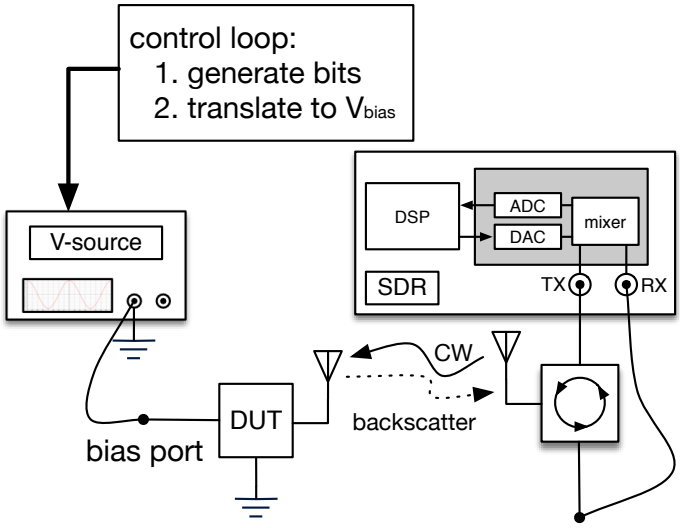

Figure 3.17: Front-end measurement setup.

3.6 Pulse Shaping Measurements

To test the pulse shaping front-ends, the experimental setup of Fig. 3.17 has been utilized, consisting of a full-duplex software-defined radio (SDR) whose transmit (Tx) and receive (Rx) ports are connected to a UHF circulator, and a voltage source that is controlled to output pulse-shaped bitstreams. The front-end is first directly wired to the third circulator port with an SMA cable. The SDR transmitter chain generates a CW at 913 MHz which excites the front-end through the circulator and the response is recorded by the SDR receiver chain. A bitstream of $N = 50$ bits is generated and pulse shaped with an SRRC pulse with rolloff factor $\alpha = 0.5$ and filter delay $A = 6$. The values were selected for moderate mainlobe width (as a increases, the mainlobe becomes wider) and moderate filter length and sidelobe suppression (as A increases, the pulse becomes longer, but with a larger sidelobe suppression). The pulse-train is normalized to the $[-1, 1]$ interval and is translated to the required bias voltage, using the $\hat{V}_{\text{bias}}(\hat{\Gamma})$ function (Fig.3.18 for the PIN front-end). The SDR implements a receiver with SRRC matched filtering, bit-level synchronization, and symbol detection to verify the accurate reception of the bitstream. For wireless measurements, the front-end is detached from the circulator and is connected to a UHF antenna. The third port

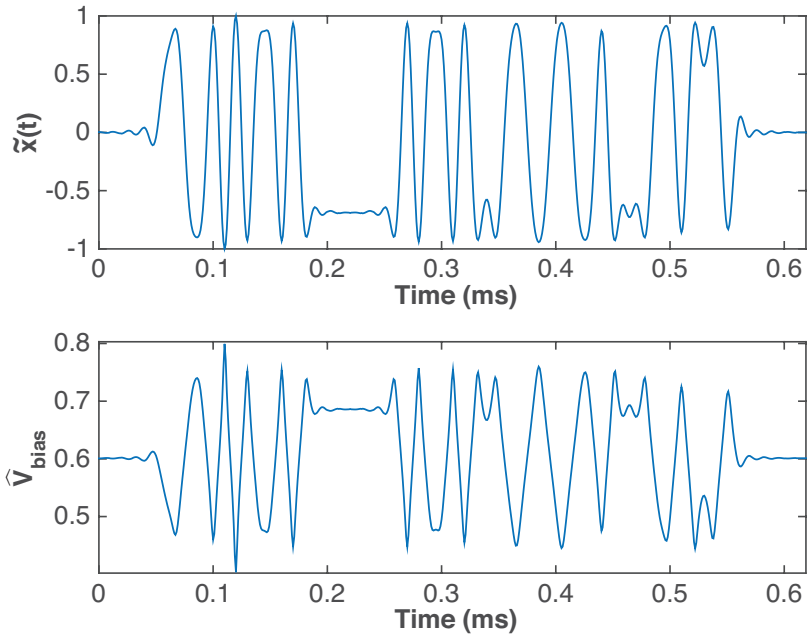

Figure 3.18: 50-bit SRRC-modulated waveform to be backscattered. Top: In reflection coefficient domain. Bottom: Translated to bias voltage domain with measured PIN front-end data.

of the circulator is also connected to a UHF antenna for wireless transmission and reception from the SDR at the 900-MHz band.

The wireless measurements have been conducted in an office environment with heavy multipath and clutter at 913 MHz with 2 dBi omnidirectional antennas for the reader and modulator, and carrier transmission power P_T = 15 dBm.

For comparison, a front-end consisting of a simple on-off RF switch is tested with the same bitstream. In Fig. 3.19-1, the bitstream is shown, modulated with conventional rectangular pulses. In Fig. 3.19-2 and Fig. 3.19-3, the SDR-received backscattered SRRC pulses from the PIN front-end are shown for wired and wireless cases, respectively. The backscattered SRRC pulses are smooth, showcasing the continuity of $\Gamma(t)$ achieved with the PIN front-end, and are successfully decoded by the SDR receiver after matched filtering. In Fig. 3.19-4, the same bitstream with SRRC pulses is shown for the FET front-end.

In Fig. 3.20, the eye diagrams of the received SRRC waveforms are shown. The top eye diagram corresponds to an ideal (simulated) SRRC pulse-train. The middle and bottom eye

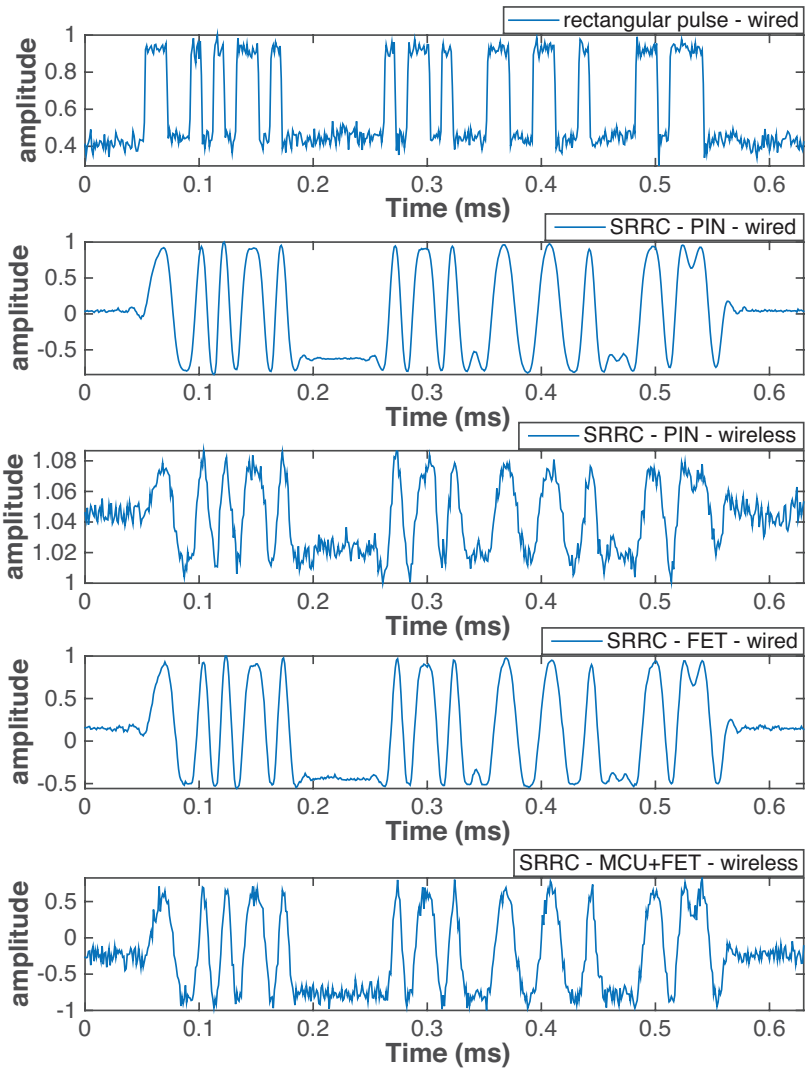

Figure 3.19: SDR-measured backscatter signals in time domain. 1: conventional rectangular pulses. 2 & 3: SRRC pulses with PIN front-end. 4: SRRC pulses with FET front-end & 5: SRRC pulses with MCU + FET front-end.

diagrams correspond to the PIN-generated and FET-generated SRRC pulse-trains. It can be seen that the actual, front-end backscattered pulses are closely following the envelope of the ideal SRRC pulses. The eye maximum height is equal to the magnitude of the difference of the reflection coefficient values at 0 V/1 V for the PIN front-end and 0 V/2 V for the FET front-end, respectively. The eye diagram is useful for quantifying the timing errors (jitter) of the pulse-shaped bits. The analyzed jitter percentage for the PIN front-end is 0.4% and for the FET front-end it is 0.35%. In Fig. 3.20-bottom, a portion of the SRRC-shaped

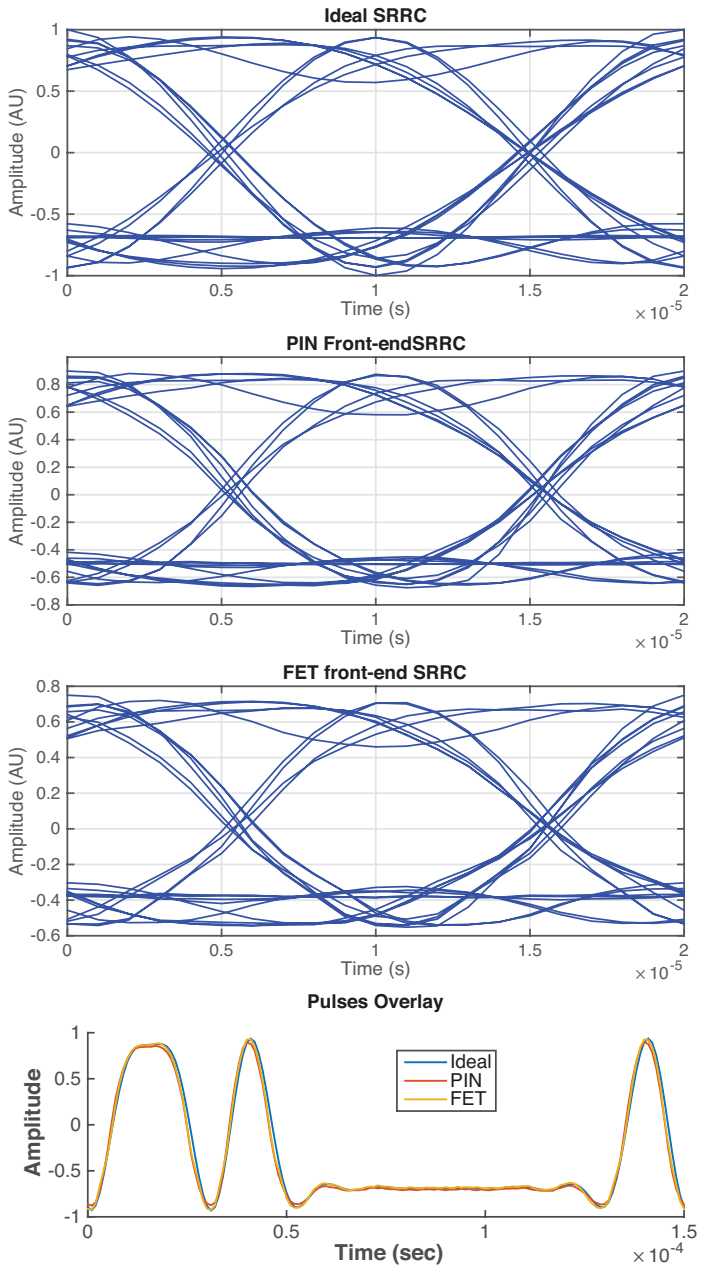

Figure 3.20: Eye diagrams for SRRC pulse transmission and received pulses overlay for ideal SRRC, measured PIN-generated SRRC, and measured FET-generated SRRC.

pulsetrain is overlaid for the ideal case and the PIN and FET front-ends. It can be seen that the SRRC envelope is followed with minor variations, and most importantly, for the FET case, the effect of the curvature of $\Gamma(V_{\text{bias}})$ (Fig. 3.11) is negligible and has not affected the pulse shape. This verifies the accurate generation of the SRRC shape, without significant signal distortion.

The spectrum of the received rectangular pulse-modulated data is shown in Fig. 3.21 across with the spectrum of the SRRC-shaped data with the PIN front-end for a data rate of $R = 100$ kbps. It is apparent that the power decay is sharper for SRRC-pulse shaped backscatter, with an out-of-band suppression of up to 35 dB, for the same received pulse energy. Moreover, the SDR-captured spectrum of the SRRC-pulse shaped data occupies a frequency window of 150 kHz, which matches with the theoretical bandwidth of SRRC $W = (1 + \alpha)R = 150$ kHz. It is noted that the spectrum around the second harmonic of the backscatter signal was monitored for reflected harmonics due to non-linearity effects, but no increased power was observed.

In Fig. 3.22, the smoothed spectrum of rectangular pulses, SRRC pulses from the PIN front-end, and SRRC pulses from the FET front-end are plotted for easy visual comparison. The two pulse-shaping front-ends feature an equal-width mainlobe, while the sidelobe suppression for the FET front-end is slightly higher (up to 42 dB) compared to the PIN front-end (up to 37 dB). The main lobe of the pulse shaping front-ends' signals is narrower than the rectangular pulse one, and sidelobe suppression is around 40 dB with a fast-decaying spectrum, in contrast with a maximum suppression of 25 dB for the rectangular pulses and a slower-decaying spectrum.

3.7 Front-end Energy Efficiency

Backscatter modulators require very low energy for communication compared to active radio transmitters used for sensor networks. For example, active radios currently in the market, such as TI CC1101, Semtech SX1232, and Murata TRC103, which all operate in the UHF ISM band, feature power consumptions ranging from 48 mW to 375 mW, which correspond to required energy-per-bit ranging from 480 nJ/bit up to 3.75 μJ/bit for 100-kbps transmissions. On the other hand, backscatter modulators require significantly lower energy, due to their minimal RF front-end structure.

For power-limited scenarios, such as those commonly encountered in practical IoT

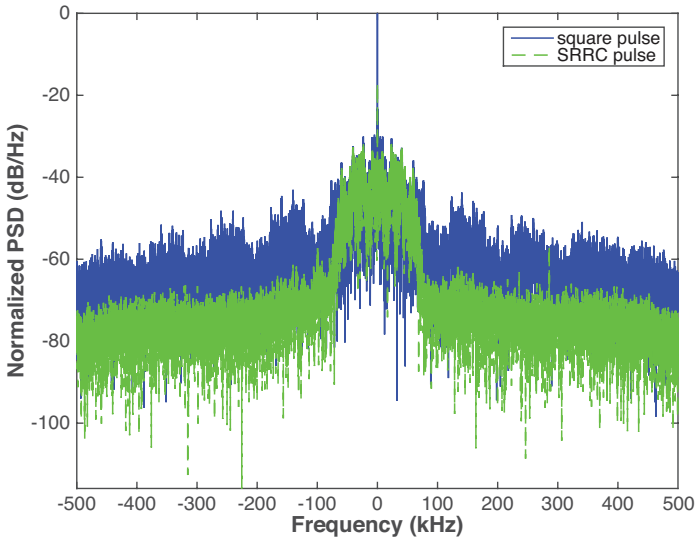

Figure 3.21: Measured spectrum comparison of wireless SDR-received backscatter rectangular pulse and SRRC pulse-shaped backscatter. The strong DC peak corresponds to the reader's CW that illuminates the backscatter modulator.

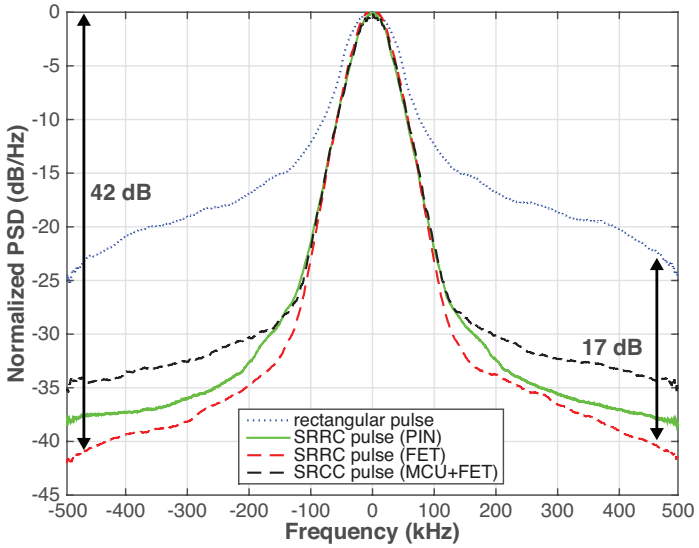

Figure 3.22: Measured spectrum comparison of rectangular pulse-modulated waveform, SRRC pulse-shaped waveform from the PIN front-end, SRRC pulse-shaped waveform from the FET front-end, and SRRC pulse-shaped waveform from the FET driven by an MCU.

sensors, it is necessary to compare backscatter front-ends with respect to power dissipation. However, since the purpose of a backscatter modulator is the communication with a reader/receiver, there are important communication parameters to be considered, such as the received signal-to-noise ratio (SNR) from a backscatter tag, the backscattered signal's

Table 3.1: Backscatter front-ends comparison. Bitrate: R=100 kbps, Receiver Bandwidth: B=R/2 (1 Sample/bit) .

Front-end & modulation	Energy per bit (Power)	$\lvert\Delta\Gamma\rvert$	Pulse Energy Loss	Rx BW Energy Loss	Energy Efficiency	Signal Bandwidth
$2\times$ PIN, 4-QAM, rect. pulses ([52])	800 nJ/bit (80 mW) (*)	0.44	0 dB	-1.1112 dB	52.7466 dB	∞
PIN, binary, SRRC pulses (this work)	$<$ 60 nJ/bit (6 mW)	1.8	-3.3475 dB	-0.4172 dB	$>$ 73.5681 dB	75 kHz
SP4T, 4-QAM, rect. pulses ([38])	14.037 pJ/bit (1.405 μW) (*)	≤ 1.55 (#)	0 dB	-0.4389 dB	111.8916 dB	∞
FET, binary, rect. pulses (this work)	$<$ 3 pJ/bit (300 nW)	1.5	0 dB	-1.1112 dB	$>$ 117.6487 dB	∞
FET, binary, SRRC pulses (this work)	$<$ 3 pJ/bit (300 nW)	1.5	-3.3475 dB	-0.4172 dB	$>$ 114.9947 dB	75 kHz
FET, 4-PAM, rect. pulses (this work)	$<$ 2.5 pJ/bit (250 nW)	1.5	0 dB	-0.4421 dB	$>$ 119.1004 dB	∞
FET, 4-PAM, SRRC pulses (this work)	$<$ 2.5 pJ/bit (250 nW)	1.5	-3.2905 dB	0 dB	$>$ 116.2359 dB	37.5 kHz

* Average power consumption is assumed
# Calculated from the manufacturer-provided insertion loss in SP4T datasheet [81] and does not include additional losses; all other rows include measured transmission line and connectors losses.

bandwidth, any signal energy losses associated with pulse shaping, and losses at the receiver's finite sampling rate/bandwidth front-end. Energy-per-bit is not a sufficient metric for comparison for backscatter tags, because in backscatter modulation the power dissipation of the front-end is not proportional to the transmitted signal's amplitude, as in active radios. In the latter, the dissipated front-end power is used towards the amplification of the RF signal that is *radiated* towards a receiver. At the receiver, the SNR is proportional to the received signal power, which is proportional to the radiated signal power, and therefore it is a function of the transmitter's dissipated power. In backscatter radio, the SNR at the reader is proportional to the received signal power, which is a function of the reflection coefficient values of the tag during its modulation states. Since for backscatter radio the modulation takes place on the tag, whereas the carrier signal radiation takes place on a reader/carrier emitter/signal generator, the modulation front-end's efficiency characterization needs to involve both the power dissipation and the reflection coefficient values. This section describes a number of parameters that need to be specified for each front-end, and gives an *Energy efficiency* metric formula for a fair comparison of front-ends under the same bitrate and finite receiver bandwidth.

3.7.1 Energy per bit E_{bit}

The energy-per-bit E_{bit} of a backscatter modulator is the amount of energy required to be spent to backscatter 1 bit of information, regardless of the modulation scheme or constellation size. It is a direct function of the front-ends power dissipation P_{dis} and the *bit* duration T_b (i.e. not symbol duration T_s).

$$E_{\text{bit}} = P_{\text{dis}}\, T_b \quad (\text{J/bit}), \tag{3.17}$$

where P_{dis} is in Watts and T_b is in seconds/bit. For a binary modulation, the bit duration equals the symbol duration $T_b \equiv T_s$, but for higher-order constellations $T_s = T_b\ \log_2 M$, where M is the constellation order, e.g. for QPSK/4-QAM, $M = 4$ and the bit duration is half of the symbol duration.

For the PIN diode front-end of this work, the *maximum* dissipation is $P_{\text{dis}} = 6$ mW, and for 100 kbps, $T_b = 10\ \mu$s/bit, therefore $E_{\text{bit}} = 60$ nJ/bit. Comparison can be made with the energy-per-bit of 400 nJ/bit for the $2\times$PIN QAM modulator of [52] on Table I

For MOSFET circuits, the power dissipation can be calculated based on the supply voltage, gate leakage current , and switching dissipation. For the FET front-end of this work, the *maximum* bias voltage is $V_{\text{max}} = 2$ V, the gate leakage current and the gate capacitance are $I_{\text{GSS}} = 100$ nA and $C = 1$ pF, and the *maximum* switching speed for 100 kbps is $f_{\text{max}} = 1/(2T_b) = 50$ kHz. Then the maximum power dissipation can be calculated as

$$P_{\text{dis}} < I_{\text{GSS}} V_{\text{max}} + \frac{1}{2} C V_{\text{max}}^2 f_{\text{max}} = 300\ \text{nW} \tag{3.18}$$

and E_{bit} <3 pJ/bit. For implementing 4-PAM with the same FET front-end, the symbol duration is $T_s = 2T_b$, and therefore the switching speed reduces to 25 kHz. Then the power dissipation is $P_{\text{dis}} < 250$ nW and $E_{\text{bit}} < 2.5$ pJ/bit.

3.7.2 Average reflected power $|\Delta\Gamma|^2$

It is known that the detection error at the reader in terms of bit-error-rate (BER) is minimized when the received SNR is maximized for the backscattered signal. From [26,31,73], the SNR for binary backscatter modulators is proportional to

$$|\Delta\Gamma|^2 \triangleq |\Gamma_1 - \Gamma_0|^2, \tag{3.19}$$

where Γ_0 and Γ_1 are the two reflection coefficient values corresponding to the two discrete load values used for modulation and $\Delta\Gamma$ denotes their difference. The difference amplitude $|\Delta\Gamma|$ has to be maximized, in order to minimize the BER at the reader. This means that the distance between the two discrete constellation points Γ_0, Γ_1 on the Smith Chart has to be maximized. For pulse shaping backscatter front-ends, the difference amplitude is defined as $|\Delta\Gamma_{\text{ps}}|^2 \triangleq |\Gamma(V_{\text{min}}) - \Gamma(V_{\text{max}})|^2$. A large $|\Delta\Gamma_{\text{ps}}|$ means a large distance on the complex plane between a positive pulse's peak value and a negative pulse's peak value. This is analogous to the maximization of $|\Delta\Gamma|$ for conventional backscatter modulators and leads to lower BER for pulse-shaped backscatter. For the PIN diode front-end, $|\Delta\Gamma| \approx 1.8$, while for the FET front-end, $|\Delta\Gamma| \approx 1.5$. Comparison of other front-ends $|\Delta\Gamma|$ can be seen in Table I, where the $|\Delta\Gamma|$ shown for the PIN and SP4T QAM modulators corresponds to the difference between two antipodal points on the smith chart, although the $|\Delta\Gamma|$ between two adjacent points is less than that.

3.7.3 Pulse Energy Loss

Typical backscatter modulators have $|\Gamma| \leq 1$, which means the reflected signal amplitude is limited to a maximum value of 1. In the ideal case, a rectangular pulse modulator with states $\Gamma_0 = 1, \Gamma_1 = -1$ will be fully reflective for the whole duration of the signal $\tilde{x}(t)$,

maximizing the signal energy

$$E_x^{\text{rect}} = \int_{-\infty}^{+\infty} |\tilde{x}_{\text{rect}}|^2 \, dt \tag{3.20}$$

which maximizes the signal SNR at the reader. When performing pulse shaping with non-rectangular pulses though, a non-rectangular signal with maximum amplitude of 1 will have energy

$$E_x^{\text{pulse}} = \int_{-\infty}^{+\infty} |\tilde{x}_{\text{pulse}}|^2 \, dt, \tag{3.21}$$

which is always be less than E_x^{rect}. The ratio

$$L_{\text{pulse}} = E_x^{\text{pulse}} / E_x^{\text{rect}} \tag{3.22}$$

is the *pulse energy loss*, and it can be calculated numerically or experimentally by generating very long sequences of bits and calculating their energy in the time domain. As an example, the calculated pulse energy loss for binary modulation with SRRC pulse shaping compared to rectangular pulses is $L_{\text{pulse}} \approx -3.35$ dB. For 4-PAM modulation with SRRC pulses the loss is $L_{\text{pulse}} \approx -3.29$ dB (Table I).

3.7.4 Receiver Bandwidth (Rx BW) Energy Loss

Receiver chains in readers have a finite bandwidth defined by the sampling rate F_s of the receiver. The baseband Rx bandwidth is $B = F_s/2$, thus the received signal spectrum at the receiver is in the $-B \leq F \leq B$ frequency band. Depending on the backscattered signal characteristics (i.e. the pulse shape) the full signal PSD can not be represented within the receiver bandwidth. Since ideal receivers with infinite bandwidth do not exist in practice (and if they did, the additive noise power at the receiver would be infinite), it is imperative to compare the signal energy loss due to Rx bandwidth finiteness. This is performed under

a reference unit bandwidth for all signals, regardless of the total bandwidth they need to be fully represented. Choosing $F_s = R$, exactly 1 sample per bit is acquired at the receiver within the unit bandwidth $B = R/2$. The Rx bandwidth energy loss is defined as

$$L_{\text{BW}} = \frac{\int_{-B}^{B} |\tilde{X}_{\text{pulse}}(f)|^2 \, dF}{\int_{-\infty}^{\infty} |\tilde{X}_{\text{pulse}}(f)|^2 \, dF} \tag{3.23}$$

and can be calculated (or approximated) numerically by computing $\tilde{X}(f)$, the Fourier transform of $\tilde{x}_{\text{pulse}}(t)$, for any pulse shape. As an example, the Rx bandwidth energy loss for binary modulation with rectangular pulses is $L_{\text{BW}} \approx -1.11$ dB, while for binary modulation with SRRC pulses it is $L_{\text{BW}} \approx -0.41$ dB. This is intuitive, due to the higher spectral efficiency of SRRC pulses compared to rectangular pulses. Other calculated Rx bandwidth energy loss values can be seen in Table I, where interesting comparisons can be made between different modulation schemes and pulse shapes.

3.7.5 Energy Efficiency

An *energy efficiency* metric shall be defined that involves a front-end's energy-per-bit and reflected power capability, as well as the respective pulse energy loss and Rx bandwidth energy loss:

$$e = \frac{|\Delta\Gamma|^2}{E_{\text{bit}}} L_{\text{pulse}} \, L_{\text{BW}} \;\; \text{(bits/J)}. \tag{3.24}$$

The formula intuitively expresses how much the energy spent for each bit is worth in terms of useful signal SNR at the reader. It takes into account the modulation scheme, constellation size, pulse shape, finite Rx bandwidth, and the front-end circuit implementation. The formula can be fairly used for direct comparisons between front-ends as in Table I, where the increased efficiency of each front-end can be seen.

It is shown that for a constellation size of $M = 4$, this work's front-end with binary modulation has an increased energy efficiency when compared to the two 4-QAM front-

ends of the same data rate, with or without SRRC pulse shaping. For the FET front-end, when binary modulation and SRRC pulse shaping is used, the energy efficiency is 2.5 dB lower compared to using the same FET with rectangular pulses. This is mainly due to the pulse energy loss, but comes at the benefit of a significantly reduced bandwidth of 75 kHz, compared to the infinite rectangular pulses bandwidth. The FET front-end shows an increased performance with higher-order constellations, e.g. compared to the SP4T 4-QAM front-end, it is 7.2 dB more efficient with rectangular 4-PAM, and 4.33 dB more energy-efficient with SRRC-shaped 4-PAM, while also featuring a reduced signal bandwidth of 37.5 kHz. From these results it can be derived that the FET pulse shaping front-end would be favorable to use for power-limited and bandwidth-limited systems.

3.7.6 Link Budgets

The received power from a pulse shaping modulator can be calculated with [26]:

$$P_R = P_T \frac{G_T G_R G_{\text{tag}}^2 \lambda^4}{(4\pi)^4 r_T^2 r_R^2} \frac{|\Delta\Gamma|^2}{4}, \tag{3.25}$$

where G_T, G_R are the gains of the reader transmit and receive antennas, and G_{tag} is the gain of the tag antenna, $\lambda = c/f_c$ is the wavelength, and r_T, r_T are the distance between the transmitter and tag and the distance between the tag and receiver, respectively. For a monostatic reader, $G_R = G_T$ and $r_T = r_R$. The received SNR from a pulse shaping modulator is

$$\text{SNR} = \frac{P_R\, K}{N_F\, N_0\, B}\, L_{\text{pulse}}\, L_{\text{BW}}, \tag{3.26}$$

where $N_0 = -174$ dBm/Hz is the noise power spectral density, $K \triangleq F_s/R$ is the number of received samples per bit (oversampling factor), B is the receiver bandwidth, and N_F is the receiver noise figure.

For the FET modulator of this work performing binary modulation with SRRC shaping,

a maximum communication range can be found for $|\Delta\Gamma| = 1.5$, $P_T = 15$ dBm (SDR output power), $N_F = 10$ dB, $B = 500$ kHz ($K = 10$ samples/bit), $G_T = G_R = G_{\text{tag}} = 2.15$ dBi, and $f_c = 913$ MHz. The threshold is set to a high SNR value of 10 dB, to achieve a minor BER value of 10^{-5} ([45]), which gives a maximum monostatic range of 45 m. However, utilizing bistatic architectures the tag-to-receiver distance can be boosted to 100+ meters [1, 47].

3.8 Practical MCU Implementation

To demonstrate the feasibility of generating arbitrary waveforms and perform pulse shaping on low computational power platforms, the backscatter communication block of Fig. 3.12 has been ported on an off-the-shelf MCU board as a proof-of-concept. The Silicon Labs C8051F120 MCU has been utilized, with a typical current consumption of 2.431 mA at 3 V, with a system clock of 3.0625 MHz [82]. The F120 incorporates a 12-bit digital-to-analog converter (DAC) that is capable of generating arbitrary waveforms with a typical current consumption of 110 μA, which corresponds to a 4.5 % power consumption increase for the MCU. Although the F120 MCU has been used as an example, other lower-consumption commercial MCUs can be utilized with the same principles.

The MCU has been set up to output 50-bit SRRC-shaped bitstreams at 100 kbps, translated to output voltage levels which are routed to the DAC unit. The DAC output terminal drives the BF1118 FET transistor front-end and the MCU effectively replaces the V-source block of Fig. 3.17. A photo of the Silicon Labs development kit and the front-end can be seen in Fig. 3.23. It is noted that no other peripherals on the board are utilized (e.g. serial transceiver IC, external crystal oscillator, etc), and therefore the system can be implemented on a single board hosting only the MCU, the FET front-end, and a connector for the JTAG programming pins and power pins, where a 3 V coin cell battery holder, or a solar cell, or a harvester's output port can be interfaced.

The wirelessly-received waveform of the MCU-modulated data can be seen in Fig. 3.19-

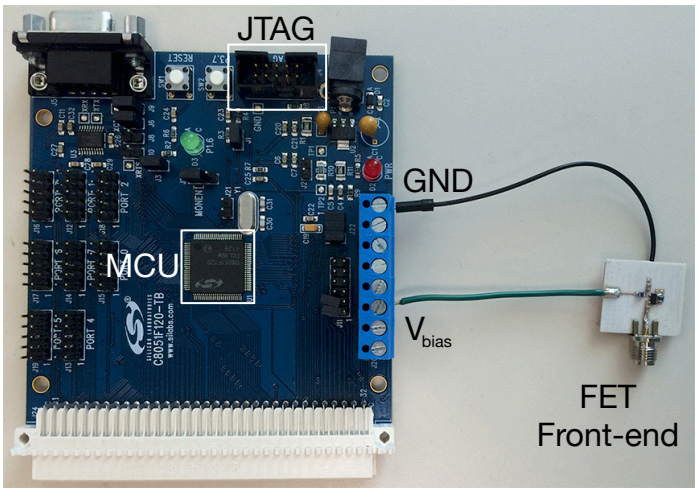

Figure 3.23: Pulse shaping FET front-end interfaced to MCU board. Only the MCU and JTAG programming connector are utilized from the development kit.

5 for comparison with the other SDR-received waveforms. The SDR-received spectrum of the FET front-end driven by the MCU can be seen in Fig. 3.22, where a sidelobe suppression of up to 35 dB is achieved. This can be further improved with the utilization of a higher-resolution DAC; detailed information on optimized DAC operation, as well as how quantization (bit resolution) affects the signal spectrum can be found in several publications and whitepapers (e.g. [83–85]). The DAC utilized for this work as a proof-of-concept has a resolution of 12 bits, a typical power consumption of 110 μA and a slew rate of 0.44 V/μs for a 40 pF load, which is more than adequate for the FET modulator since the load (FET gate) capacitance is 1 pF $<<$ 40 pF and no sharp transitions from a full-off (0 V) to full-on (2 V) level are required. The transitions are always slower than $f_{\text{max}} = 1/(2T_{\text{bit}}) = 50$ kHz and would require in maximum a slew rate of $V_{\text{max}}/(2T_b) = 2$ V/20 μs = 0.1 V/μs.

Another option for generating analog signals involves the pulse width modulator (PWM) unit available on many MCUs. A PWM outputs pulses of variable width which can be filtered with a low-pass network to to generate analog waveforms. The implementation details are MCU-specific but examples can be found in [86–89]. The main challenge with this approach is the design of the filter in terms of sharp cutoff (dB/octave) and in-band signal attenuation.

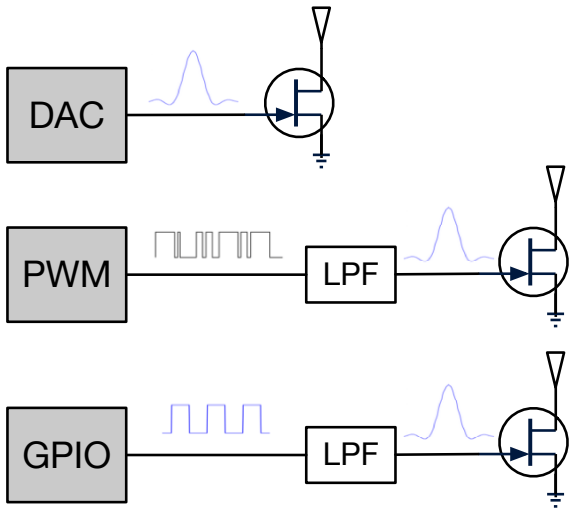

Figure 3.24: Pulse shaping implementation options.

An even more minimal approach for pulse shaping can be the utilization of a fully-passive RLC low-pass network to filter rectangular pulse-modulated bitstreams as they come out of a tag's digital port and before they drive the backscatter modulator. For example, Gaussian pulse shaping could be achieved by constructing an LC low-pass Gaussian filter to suppress the high frequency components of rectangular pulses that drive the front-end's transistor [90, 91]. The main limitation with this approach is that the pulse shape is 'hardcoded' in the circuit and thus no arbitrary waveforms can be generated; despite that, it can be an appealing practical implementation for non-MCU tags, such as the ones in [20, 43], where the only option is to switch between two impedance states and no DACs or PWMs are available. The complexity reduction by removing the need of a DAC or PWM comes at the cost of increased signal processing at the reader, e.g. in the case that Gaussian filters are implemented, the pulse-shaped bitstreams will suffer from ISI. Moreover, due to the fact that in general there is no linear relationship between the bias voltage $V_{\text{bias}}(t)$ and the reflection coefficient $\Gamma(t)$, the backscattered pulses will be distorted, which translates in additional signal processing steps at the reader (equalization), as well as undesired increase of the pulses' bandwidth.

The three options for implementing pulse shaping on a tag are summarized in Fig. 3.24.

The first (DAC) is the most flexible in terms of arbitrary signal generation, while the last (passive LPF at a digital general purpose IO pin of an MCU) gives the less flexibility, but lowest complexity and power consumption. Nevertheless, all three options can be implemented with a reasonable amount of components with low energy footprint and can effectively break the limitations of rectangular waveforms and high bandwidth occupancy found in conventional RFID tags. Tags can essentially become miniature software-defined radios to implement diverse communication schemes, spectral characteristics, or modulation formats.

CHAPTER 4

EXTREME-DATARATE BACKSCATTER FRONT-ENDS

4.1 Pushing Backscatter Radio to mmWave

Most backscatter radio implementations in the literature are targeted for 5.8 GHz, 2.4 GHz, 900 MHz, or lower frequencies (e.g. UHF) [1, 35, 49, 92]. Although design at these frequency bands is favorable because of low transmission line and active component losses, higher frequencies on the millimeter-wave (mmWave) bands can offer extensive bandwidths which can extremely boost the transmission data rates. With mmWave 5G networks going live soon, a big number of devices will benefit from high frequency bands to transmit high volumes of data, e.g. live video, real-time health data, wireless serial-link replacement, etc. However, utilizing mmWave oscillators, mixers, and amplifiers on mobile devices will directly increase their power consumption and cost, affecting battery life and market reach.

During this doctoral work, an end-to-end mmWave backscatter system for communication and sensing has been implemented and demonstrated to operate in the 24–28 GHz band. In this band, miniaturized high-gain antennas and antenna arrays can be implemented, in contrast with UHF bands, where antenna arrays can become bulky and impractical. The miniaturization that is possible in mmWave bands allows for system implementation with additive manufacturing technologies (AMTs) and direct integration with wearable and flexible electronics for mobile health, sensing, security, and short-range ultra high-speed data transmission. To achieve broadband data transmission, the backscattering operation has been leveraged in order to reflect subcarrier signals of GHz-level frequencies, which enables multi-gigabit communication with single transistor front-ends and pJ/bit energy consumption.

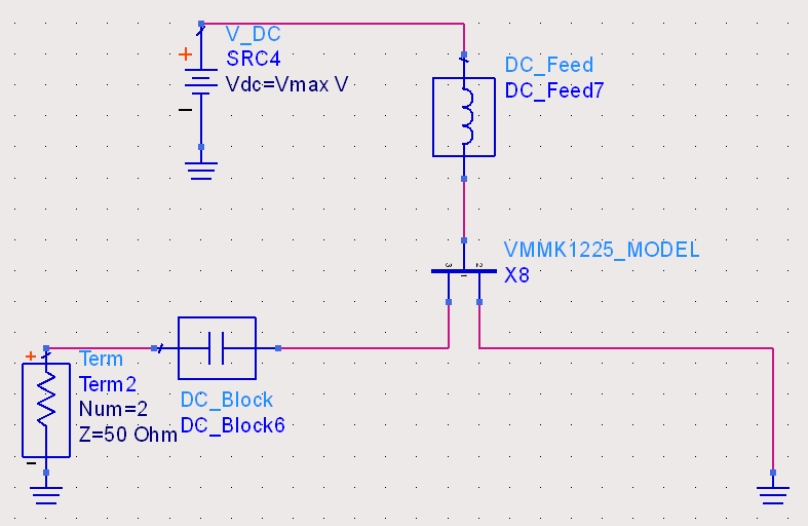

Figure 4.1: Front-end for mmWave backscatter communication.

4.2 mmWave Backscatter Front-end

The backscatter communicator/tag consists of a common-source low-power enhancement P-HEMT transistor (Avago VMMK-1225) that is directly interfaced to an antenna array through its drain (Fig. 4.1) while its gate is biased with a positive voltage (enhancement mode). The voltage pulses applied to the gate modulate the transistor's channel width and effectively modify the reflection coefficient

$$\Gamma = \frac{Z_d - Z^*_{\text{array}}}{Z_d + Z_{\text{array}}}, \tag{4.1}$$

where Z_d is the input impedance of the transistor at the drain terminal and Z_{array} is the antenna array's input impedance.

The front-end's layout can be seen in Fig. 4.2. The HEMT transistor's drain pad has been placed as close to the antenna port as possible, to minimize transmission line losses, and the bias feed (RF choke) has been implemented with $\lambda/4$-transformers, instead of parasitics-heavy lumped inductors. The rejection of the distributed RF choke that drives the gate is better than 25 dB at 24 GHz, which is the front-end's principal frequency of operation. That guarantees minimal carrier signal leakage to the gate and in turn to the bias

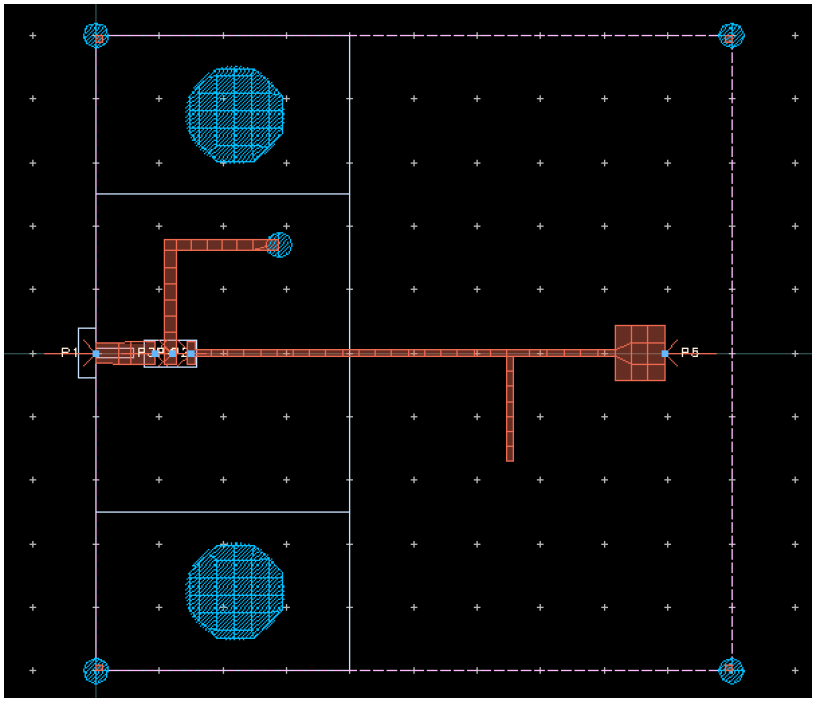

Figure 4.2: Physical layout of mmWave backscatter front-end.

source. The transistor's source has to be connected to an RF-short to achieve ideal reflection of $\Gamma = -1$ when biased and $\Gamma = +1$ when non-biased. At the same time, a dc-short is required to achieve bias signal return through the gate-source path and effectively create a $V_{\text{GS}} > 0$ bias voltage. Although the natural choice would be to place a grounded via as close as possible to the source pad, the physical dimension of the via would exceed the pad size and it would short the gate and drain. This layout issue is alleviated by connecting the transistor's source to a grounded via through two approximately-$\lambda/4$ lines in series, that guarantee an unchanged impedance (RF short). The exact lengths of the lines have been optimized to achieve a $\lambda/2$ total electrical length. Finally, the dc-block at the front-end's input has been omitted in the physical layout, since the microstrip arrays used are not dc-electrically connected between the signal layer and the ground layer. An external dc-block component is used only for the characterization of the front-end and it is taken into account during the VNA calibration.

The single-transistor front-end implemented on a thin Rogers RO4003C laminate (Fig. 4.3)

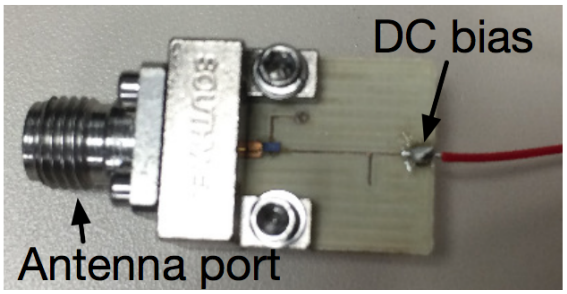

Figure 4.3: Prototype of mmWave backscatter front-end on Rogers RO4003C laminate.

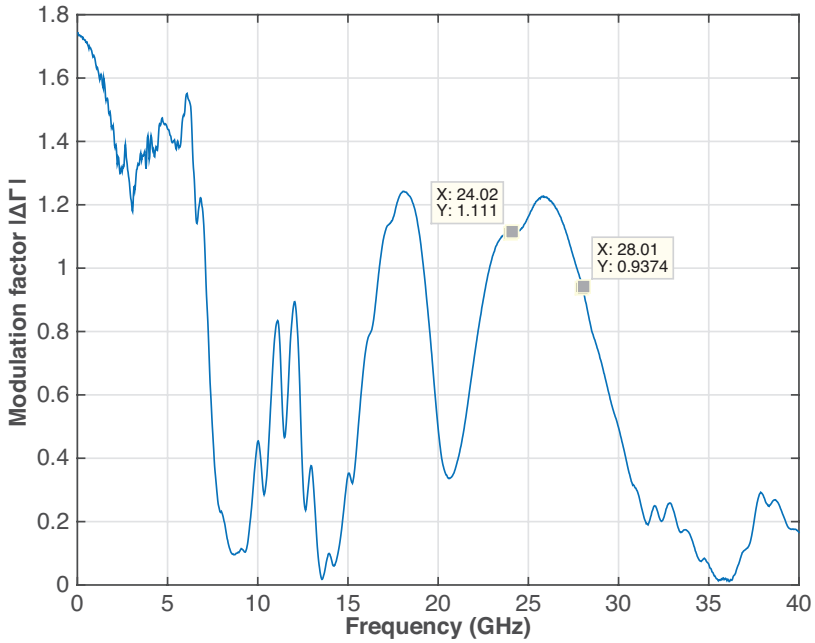

Figure 4.4: Backscatter modulation factor $\Delta\Gamma$ versus frequency for front-end DC bias voltages of 0 V and 1 V.

is used for wired characterization with a VNA for bias voltages of 0 V and 1 V. The respective reflection coefficient values Γ_0 and Γ_1 are measured up to 40 GHz and the reflection coefficient difference amplitude $|\Delta\Gamma| \triangleq |\Gamma_1 - \Gamma_0|$ is calculated, which is known as the modulation factor that needs to be maximized to optimize backscatter communication performance [26]. The measured $|\Delta\Gamma|$ shows a wideband operation around the 24-GHz band, where it remains within 0.9 to 1.2 between 23 and 28 GHz (Fig. 4.4).

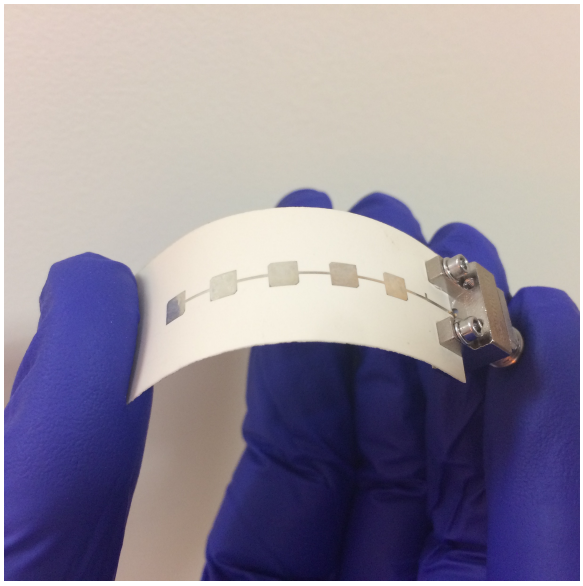

Figure 4.5: Inkjet-printed 5×1 array prototype with 2.92 mm (K) connector for VNA characterization.

4.3 Flexible printed mmWave backscatter array

A microstrip 5×1 series-fed patch antenna array is designed with a resonance frequency of 24 GHz. The substrate is 7 mil flexible liquid crystal polymer (LCP) ($\epsilon_r = 3.14, \tan\delta = 0.002$) and the metallization is inkjet-printed silver nanoparticle (SNP) ink (conductivity $\sigma = 5 \times 10^6$ S/m). The planar array is simulated with Momentum before getting fabricated with a Dimatix DMP-2830 inkjet printer (Fig. 4.5). The simulated and VNA-measured S_{11} response are shown in Fig. 4.6, where the principal resonance can be seen around 24.5 GHz, and a secondary resonance can be seen around 26.5 GHz.

The directivity (Fig. 4.7) of the array remains stable for the whole 23–28 GHz band, with a value of approximately 13 dBi. The realized gain of the array (which includes the effect of the return loss) can be seen in Fig. 4.8; the gain at the center frequency is 10 dBi, and the gain between 25.5 and 28 GHz is flat at 8 dBi. The realized gain defines the frequency regions for the mmWave backscatter operation: the carrier signal that illuminates the tag will be centered at 24.5 GHz, while the backscatter response (subcarrier) will be centered 2 GHz further, at 26.5 GHz. Both the carrier and subcarrier frequencies fall within

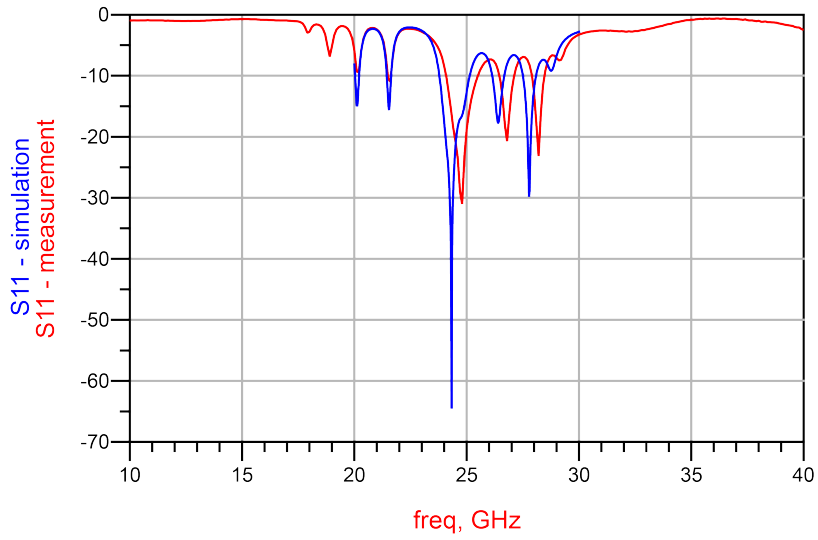

Figure 4.6: Simulated and measured array return loss (RL).

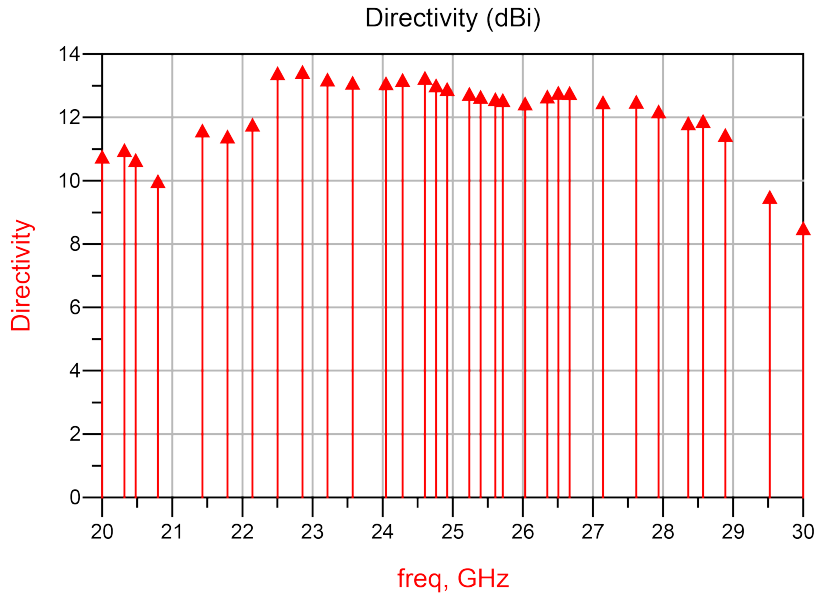

Figure 4.7: Simulated 5×1 array directivity.

the high-$|\Delta\Gamma|$ region of the HEMT front-end, which is necessary for the integration of the modulator with the array.

Since the microstrip feeds of both the modulator and the array have a characteristic impedance of $50\ \Omega$, the two layouts are directly combined on a single LCP substrate. Four layers of SNP are printed on the LCP with sharp edges (no ink "bleeding"). Details of the microstrip-to-patch transition, as well as the footprint of the 3-lead 0402 transistor SMD

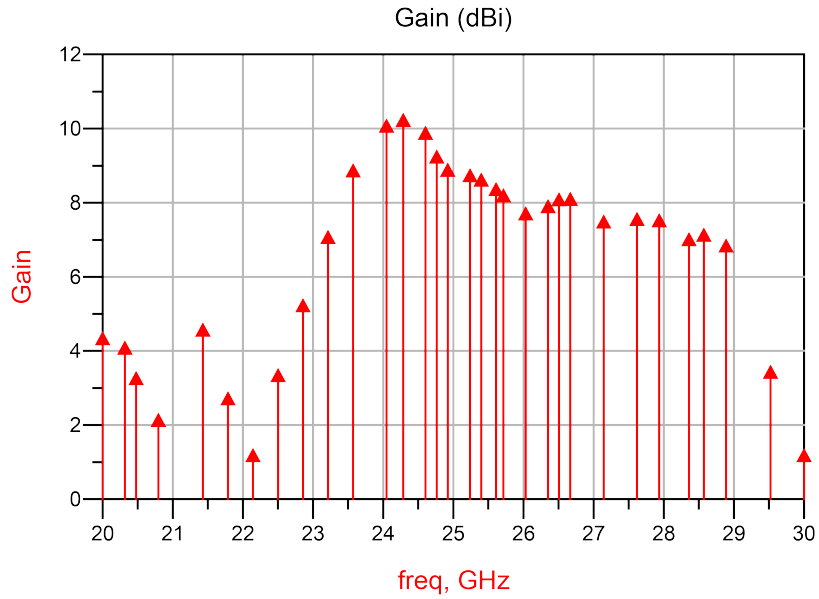

Figure 4.8: Simulated 5×1 array realized gain.

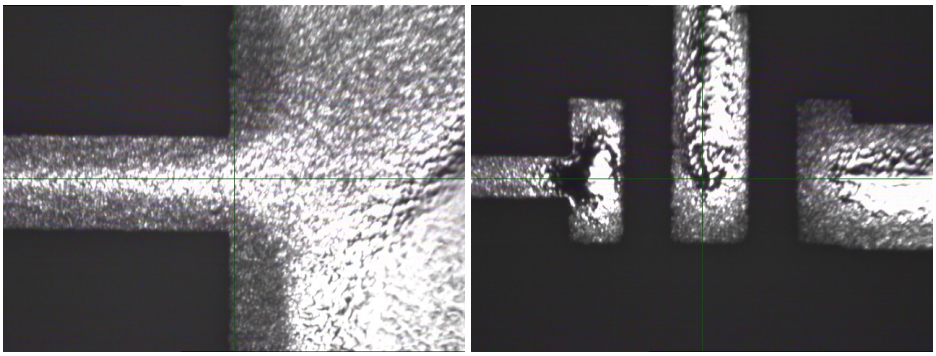

Figure 4.9: Microphotographs of inkjet-printed SNP metallization on LCP. Left: microstrip-to-patch transition. Right: 3-lead HEMT footprint (0402 SMD package).

package can be seen in Fig. 4.9. The complete modulator/array can be seen in Fig. 4.10, where the DC bias wire has been replaced with a 3.5 mm RF connector to support GHz-rate signal biasing without unwanted inductance. The total board has a length of less than 7 cm and is completely flexible with excellent silver ink adhesion (no conductor cracks while flexing).

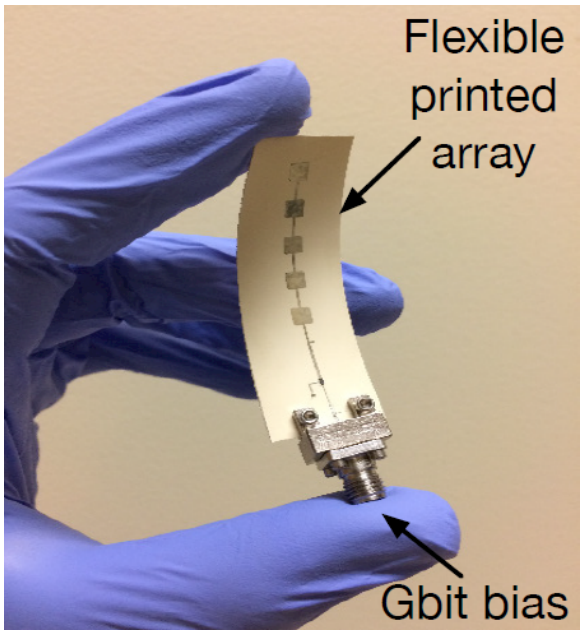

Figure 4.10: Gbit-datarate capable mmWave backscatter tag.

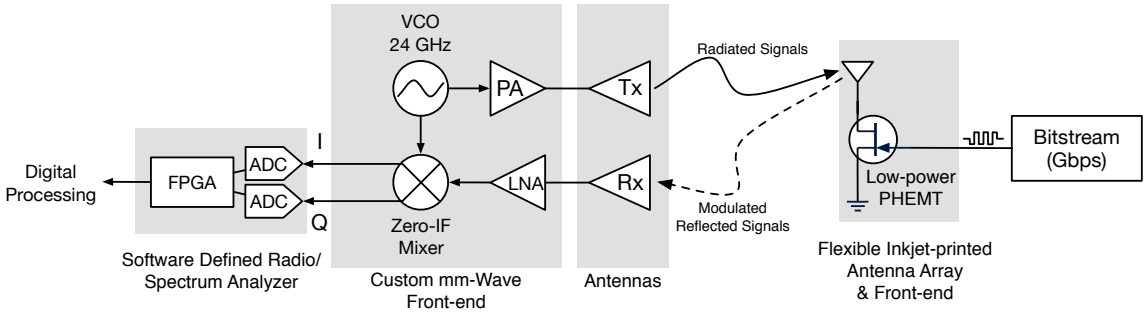

Figure 4.11: End-to-end millimeter-wave backscatter system for Gigabit communication.

4.4 End-to-end mmWave Backscatter System

A custom reader has been built that consists of a voltage-controlled oscillator (VCO - Hittite HMC739) that generates a 24-GHz continuous wave (CW) that is amplified (PA - Hittite HMC863) and radiated through a linearly-polarized transmit (Tx) horn antenna. An identical receive (Rx) horn antenna is used and the received signals are amplified with a low-noise amplifier (LNA) stage and are directly down-converted to DC with a zero-intermediate frequency (IF) mixer (Hittite HMC977). The baseband in-phase (I) and quadrature (Q) signals are routed to the inputs of a software defined radio (SDR - Ettus USRP N210) or a digital

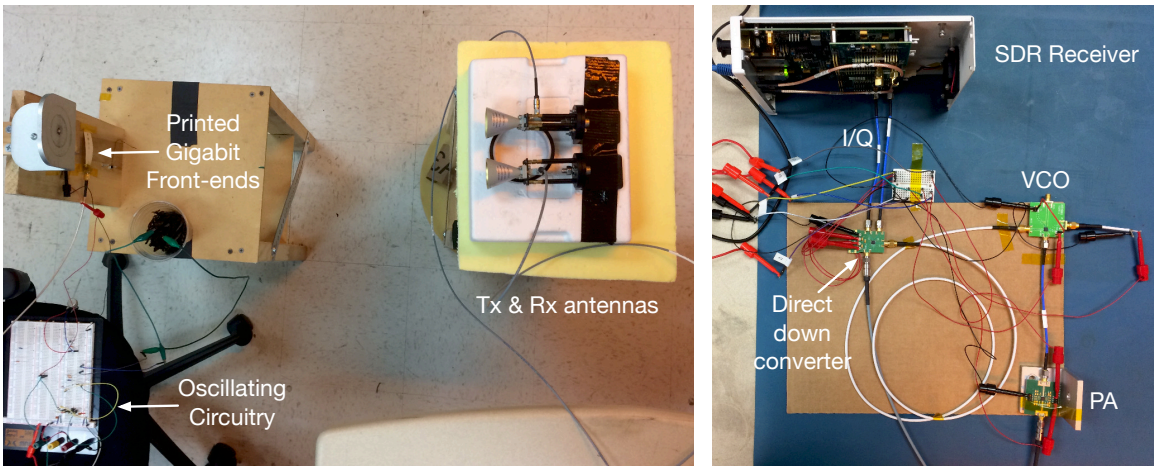

Figure 4.12: Left: Wireless backscatter testing setup. Right: Tx and Rx chains with Software Defined Radio.

storage oscilloscope for digital processing and demodulation (Fig. 4.11).

The wireless measurement setup of Fig. 4.12-left has been used with the Tx/Rx chain of Fig. 4.12-right to test the operation of the mmWave backscatter tag in sensing and wideband communication scenarios. A low-voltage oscillating circuit based on a 555 timer integrated circuit (IC) has been prototyped as a generic interface for resistive and capacitive sensors. The circuit's output is a variable-frequency pulse-train that drives the PHEMT's gate and switches the transistor on and off with a frequency F_{sub} defined by the sensors' resistance or capacitance. When a CW carrier F_c illuminates the tag's antenna, a subcarrier of frequency $F_c + F_{\text{sub}}$ is reflected towards the receiver, which can decode the sensor's information. As an example, a presence detection sensor with a resistive photocell has been implemented, that backscatters frequencies $F_{\text{sub}} = 600$ kHz away from the $F_c = 24.5$ GHz carrier in regular room lighting conditions, and around 350 kHz away, when a person is in proximity and interferes with the sensor's illumination. Also, a simple soil moisture sensor is implemented with probes whose capacitance increases when the soil is wet, and backscatters subcarriers 1.20 MHz and 1.18 MHz away from the 24.5-GHz carrier for dry and wet conditions, respectively. The received backscattered frequencies are shown in Fig. 4.13, where an operation similar to UHF backscatter oscillating sensors (e.g. [20]) can be seen.

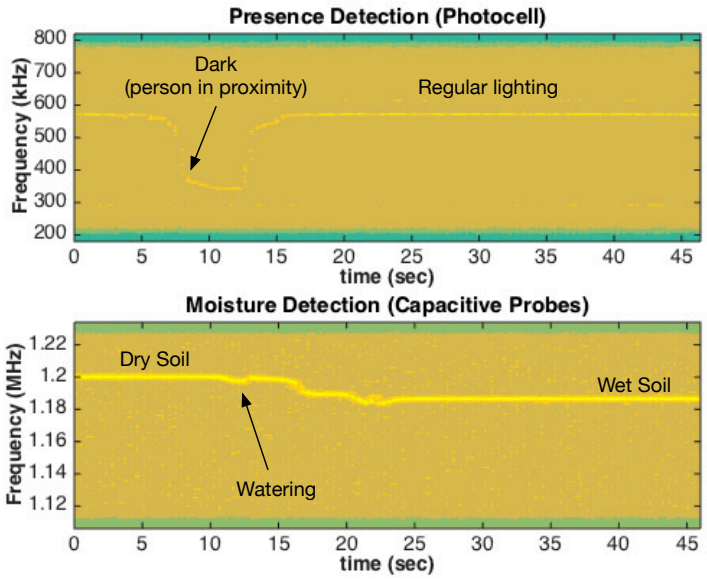

Figure 4.13: Backscattered frequency for sensing examples. Top: Presence detection with photocell. Bottom: Soil moisture detection with capacitive probes.

4.5 Gbit Backscatter Communication

The full potential of the implemented front-end is tested by biasing the tag with ultra high frequency subcarriers of several GHz, instead of the kHz–MHz-range subcarriers that are commonly used for backscatter tags in the UHF bands. Multiple tests have been conducted with ranges over 2 meters in indoor, cluttered environments and discrete frequency biasing around 500 MHz, 1 GHz, 2 GHz, 3 GHz, 4 GHz, and 5 GHz. The received subcarriers around the frequencies of 2 GHz and 4 GHz can be clearly seen in Fig. 4.14, 20–30 dB above the noise floor. A signal-to-noise ratio (SNR) estimate of the maximum versus the average channel power can be seen in Fig. 4.14-bottom, where it is apparent that a high-SNR, wideband operation can be achieved up to 3–4 GHz. This graph includes the *complete, compound* response of the *end-to-end system*, including the front-end's $|\Delta\Gamma|$ bandwidth, the printed antenna array's bandwidth, Tx chain VCO and PA efficiency, as well as Rx chain LNA and mixer bandwidth. The lower subcarrier SNR close to the 500 MHz frequency is due to the fact that clutter attributed to system nonlinearities, intermodulation

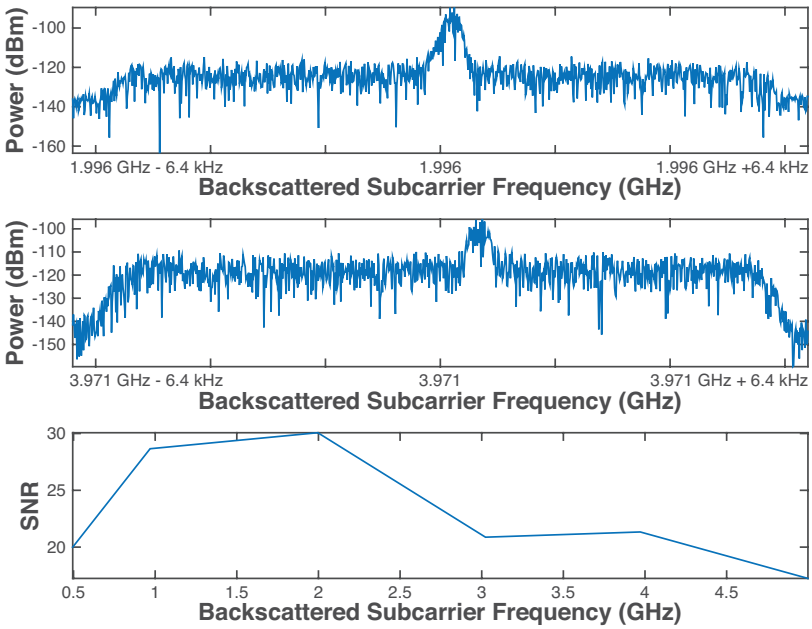

Figure 4.14: Backscattered subcarrier at 2 GHz and 4 GHz, and SNR versus subcarrier frequency.

products, low-frequency ambient scatterers, and phase noise increase while approaching the DC frequency, which is a known phenomenon in backscatter/RFID systems [1]. Nevertheless, the system shows an achievable end-to-end bandwidth of at least 4 GHz, which can enable dramatically-higher data rates, compared to the prior art, up to the Gbps-range.

To demonstrate the proof-of-concept of broadband backscatter communications, the mmWave tag has been connected to a Keysight M8190 arbitrary waveform generator (AWG) that provides the modulated bias. The reader Rx chain I and Q channels have been directed to a Keysight Infiniium S-series Digital Storage Oscilloscope (DSO) running VSA digital demodulation software and performing constellation analysis (Fig. 4.15. The AWG is first set up to output BPSK pseudorandom data with a datarate of 1 Gbps and a subcarrier of 2 GHz; that is the main lobe of the modulation bias covers the band from approximately 1.5 GHz to 2.5 GHz. Instead of performing hard level switching between 0 V and 1 V, the pulse shaping principles of Chapter 3 have been applied, and the front-end is biased with a BPSK waveform that is pulse-shaped with square-root raised cosine (SRRC) pulses with a rolloff factor $a = 0.35$ to limit the signal bandwidth. The output of the VSA software can

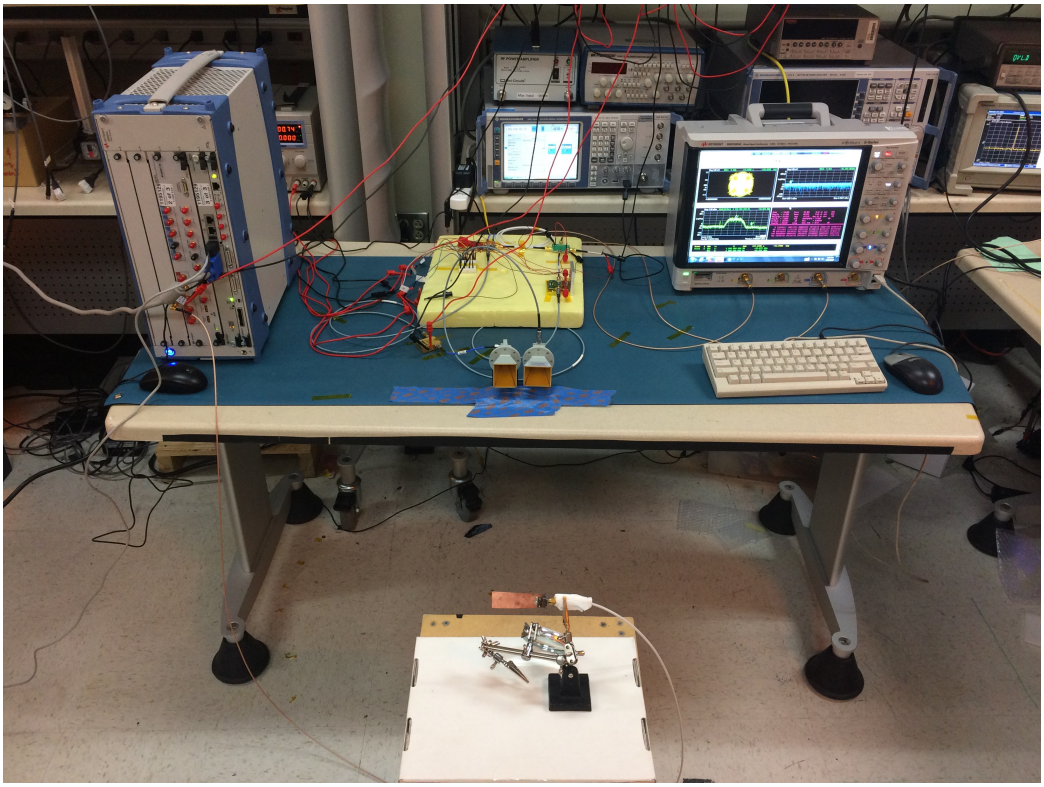

Figure 4.15: Measurement setup for Gbit-datarate mmWave backscatter.

be seen in Fig. 4.16, where the captured BPSK constellation can be seen, with an RMS Error Vector Magnitude (EVM) of 24.76%. This value corresponds to a bit error rate (BER) value of 0.2% [93] and has been achieved without any signal pre-distortion or forward error coding (FEC) at the AWG, and without equalization at the DSO/VSA. Considering the leakage gate-source current $I_{\text{GS}} = 200$ nA and maximum bias voltage of $V_{\text{max}} = 1$ V, the maximum transistor static power consumption is $P_{\text{static}} = 200$ nW. The maximum dynamic power consumption is

$$P_{\text{dyn}} = \frac{1}{2} C_{\text{GS}} V_{\text{max}}^2 f_{\text{max}}, \tag{4.2}$$

where the gate capacitance is $C_{\text{GS}} = 0.3$ pF and the maximum switching speed $f_{\text{max}} = F_{\text{sub}} + W$ is related to the subcarrier $F_c = 2$ GHz and the baseband bandwidth W of the

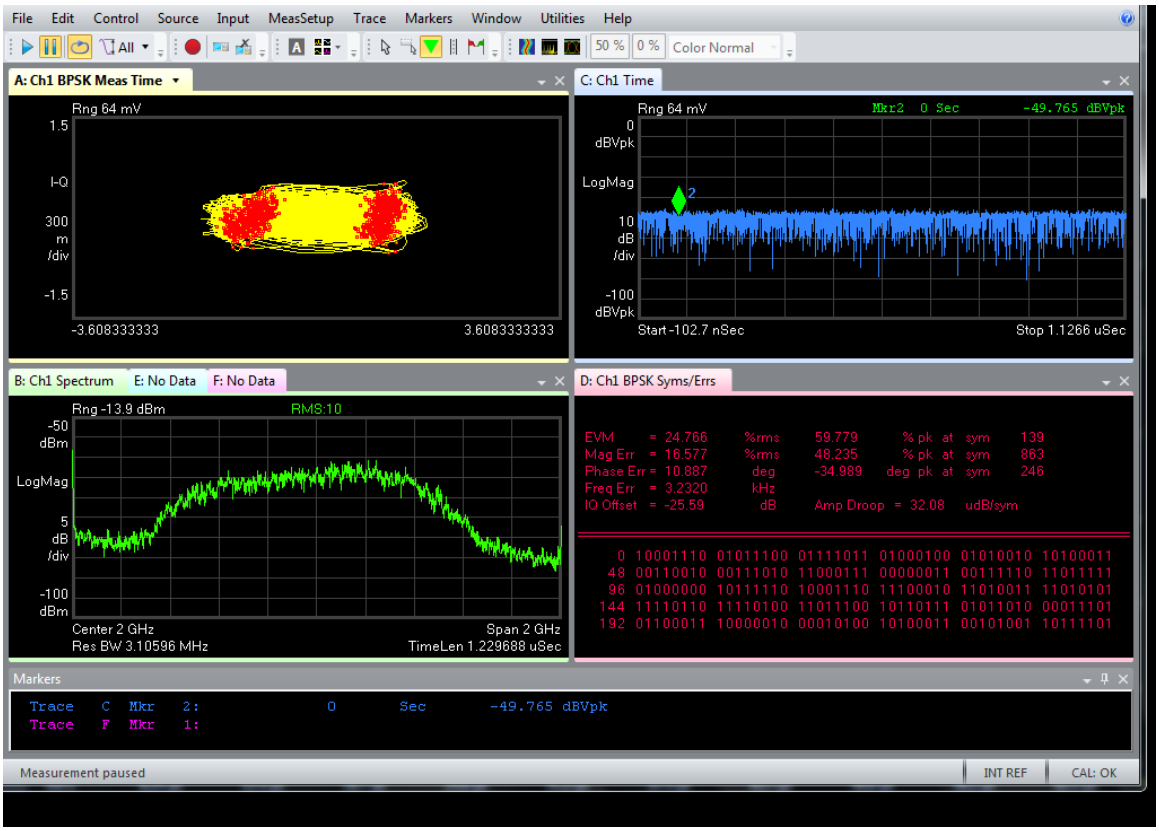

Figure 4.16: Demodulated BPSK Gbit backscatter.

SRRC pulse used:

$$W = \frac{1+a}{2\,T_{\text{sym}}} \tag{4.3}$$

In the case of 1 Gbps BPSK, $F_{\text{max}} = 2.675$ GHz, and $P_{\text{dyn}} = 401.25\ \mu$W. The energy per bit

$$E_b = (P_{\text{static}} + P_{\text{dyn}})\,T_{\text{bit}} \tag{4.4}$$

is then $E_b = 0.4$ pJ/bit.

The use of the 2 GHz subcarrier gives a very significant advantage to this backscatter system compared to the prior art. Since the modulated bias signal is pre-mixed around 2 GHz, it essentially constitutes heterodyne upconversion with a first-stage 2 GHz mixing

Table 4.1: Comparison of high-order constellation backscatter front-ends

[38]	[94]	[95]	[96]	THIS WORK
4-QAM	16-QAM	4-PAM	16-QAM	**16-QAM**
400 kbps	96 Mbps	100 kbps	120 Mbps	**2 Gbps**
12.75 pJ/bit	15.5 pJ/bit	2.5 pJ/bit	6.7 pJ/bit	**0.17 pJ/bit**

and a second, over-the-air mixing with 24.5 GHz, to reach the final subcarrier frequency of 26.5 GHz at the passband. This means that any *complex-valued* baseband signal can be upconverted to a *real-valued* 2 GHz-centered IF signal that can be used to bias the backscatter front-end. The spectrum transformation process is shown in steps in Fig. 4.17. That way, a single transistor can be used for *any* constellation size, without the need for multiple transistors ([50]) or cascaded multiplexers ([94]) used in the prior art to directly create discrete complex states. With the prior art techniques, the higher the order of the constellation, the more transistors needed to be stacked; this means that component losses are accumulated, as well, negatively affecting the backscatter SNR. To demonstrate the backscattering of high-order modulation with *a single* transistor, the AWG has been set up to generate a QPSK waveform, digitally upconverted to a 2 GHz subcarrier, and the real-valued analog signal output has been used to drive the mmWave tag. In Fig. 4.18, the demodulated QPSK constellation is shown, with an EVM of 14.75%, or BER of 0.6%. The *baudrate* is 500 MSymbols/sec, with an effective bitrate of 1 Gbps. The energy-per-bit in this case is $E_b = 0.35$ pJ/bit. In Fig. 4.19, the datarate is increased even more, with a baudrate of 500 MSymbols/sec, but with a 16-QAM constellation, boosting the bitrate to 2 Gbps, an EVM of 12.37%, a BER value of 8%, and maximum energy-per-bit of $E_b = 0.17$ pJ/bit. These are the first-ever reported Gbit-level datarates for backscatter radio, accompanied by extremely low-energy front-end consumptions, as shown in Table 4.5. The fact that this performance can be achieved with all-printed antenna arrays of a small size (5×1) shows the great potential of using mmWave backscatter for low-complexity Gbit communication, without actually utilizing mmWave modules (VCOs, mixers, amplifiers) on the sensors/IoT nodes.

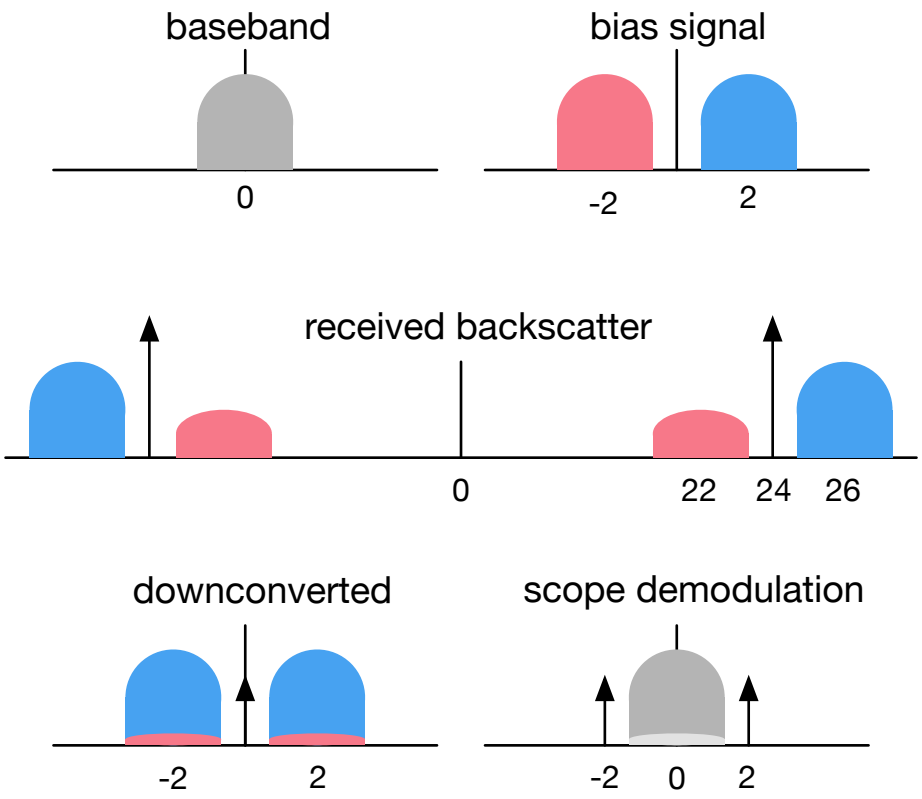

Figure 4.17: Heterodyne modulation and demodulation of Gbit-datarate mmWave backscatter. Grey lobes correspond to spectra of complex-valued signals.

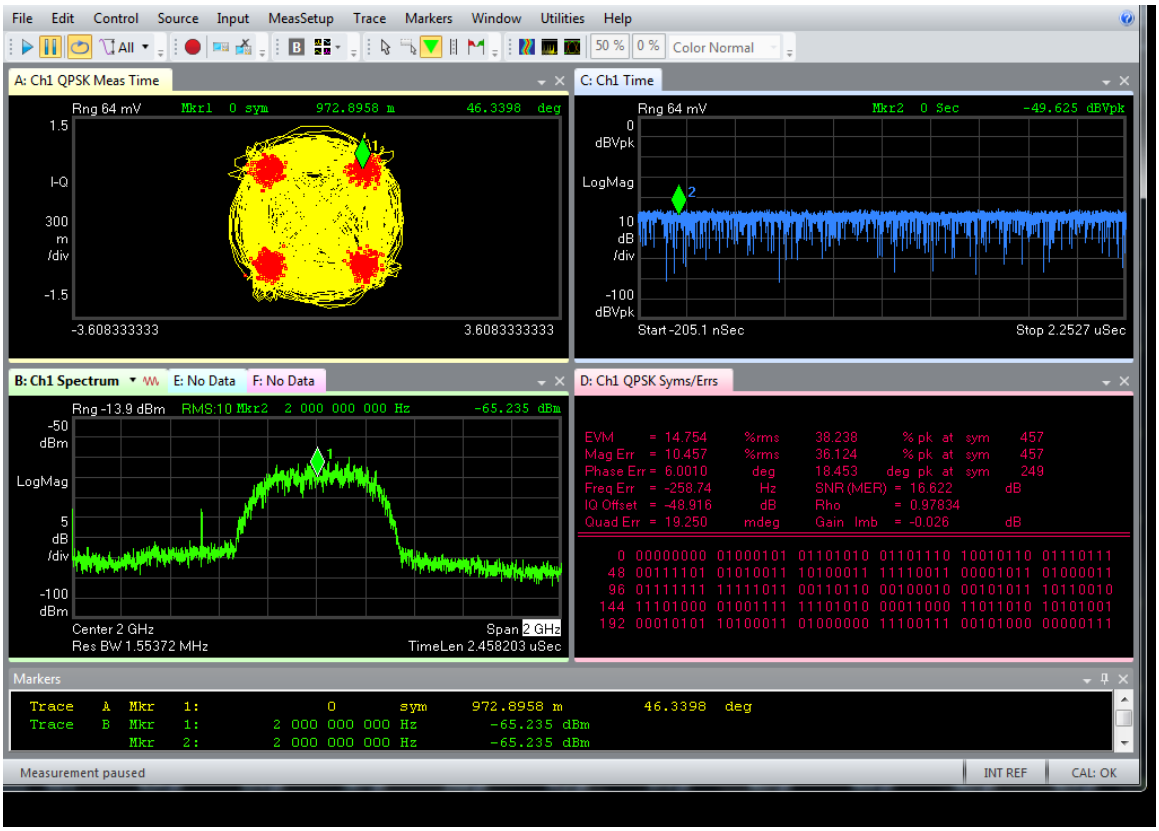

Figure 4.18: Demodulated QPSK Gbit backscatter.

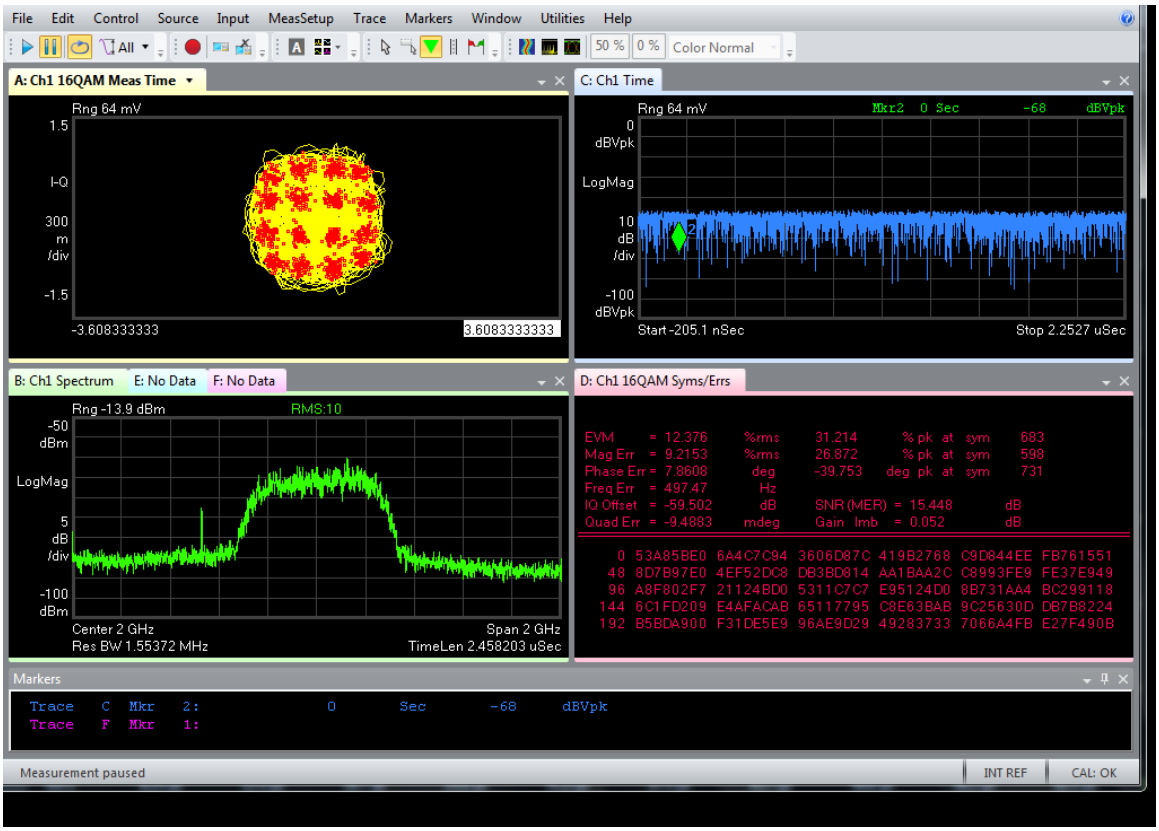

Figure 4.19: Demodulated 16-QAM Gbit backscatter.

CHAPTER 5

ORIGAMI FRONT-ENDS FOR ENERGY HARVESTING

5.1 Powering randomly-deployed sensors

Many IoT systems will require randomized sensor deployment, rather than fixed placement, exact radio channel characterization, and antenna orientation. In such random deployment scenarios, communication or harvesting might be compromised if the node's antenna does not face to the direction of the central station for conveying data or receiving power wirelessly. Typically, WSN nodes employ either wire monopole/dipole antennas, or planar patch antennas, and thus the directivity is limited to one dimension. Employing novel fully 3D structures, such as a cube, allows for the easy placement of (planar) antennas on multiple faces, enabling simultaneous harvesting/communication over different and potentially real-time reconfiguring (e.g. "origami") orientations (Fig. 5.1). RF waves from totally orthogonal planes can be exploited for harvesting and backscatter communication, enhancing the total system efficiency when multiple sources/gateways are present. Such a system can also benefit in the case of a single source that lies in an unknown direction: two orthogonal antennas increase the probability of capturing the source-emitted plane waves, compared to a single antenna facing to a single direction that can only capture RF signals from multipath reflections.

Hosting the node's antennas directly *on* the package reduces the total volume that would be required if monopole/dipole wire antennas stemming out of the package were utilized. Mechanical damage (e.g. breaking) of antennas can also be minimized since the antennas are a part of the package in this case.

A system design is presented that will benefit WSN nodes in terms of harvesting and, possibly, communication: All electronics of the WSN nodes reside inside fully 3D en-

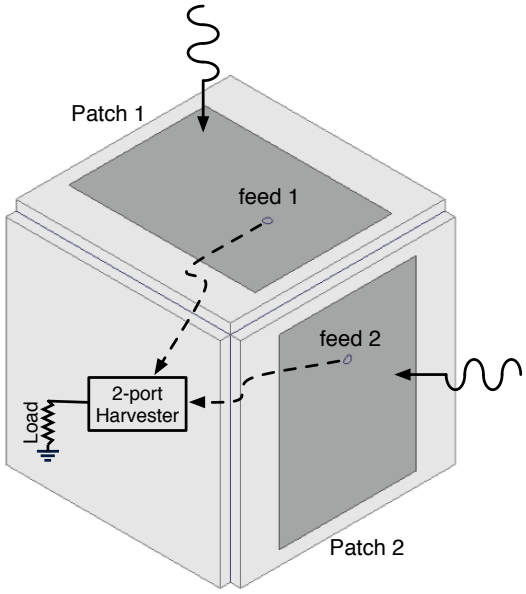

Figure 5.1: 3D cube with orthogonally-positioned on-side planar antennas on the sides and enclosed RF energy harvesting electronics.

closures, in this case a cube, that can be easily deployed on a field. Exposing only the antennas to the outer world and placing all the electronics inside the package makes the node compact, rugged, and facilitates deployment. For the fabrication of the package and its antennas, an all-additive manufacturing process is followed to facilitate prototyping and minimize the need for post-processing (e.g. connecting individual cube sides with adhesives). 3D printing is chosen for creating the plastic outer shell of the system that will a) enclose the electronics and b) host the antennas. Fabricating a cube is a straightforward process with most 3D printers; however, three main challenges appear for a packaging "smart cube" that will be used in this application:

1. The cube must be hollow, to allow for the easy and rugged placement of electronics in its interior. This typically requires the use of a supporting material that has to be removed after fabrication. For a moderately large cube size (in order to fit printed circuit boards, cables, batteries, etc) the cost of the supporting material often becomes more significant than the cost of the material used for the actual cube. Moreover the supporting material has to be typically removed with a chemical post-process, thus

adding extra steps to the fabrication process and producing waste.

2. The fabrication time for a 3D structure is mainly limited by its exterior volume. For a cube-shaped package with $2 \sim 2.5$ inch edges, the long fabrication time slows down the prototyping process.

3. The cube must have a way to open/close - preferably in real time - at least one of the sides for placing/replacing electronics in its interior.

The aforementioned challenges cannot be directly addressed with typical 3D printing techniques, and demand a non-conventional approach for the fabrication of complex 3D structures, especially with operability up to the RF frequency range.

5.2 Origami Packaging

Origami folding is the technique chosen to overcome the long fabrication time and high fabrication cost limitations by "folding" a two-dimensional structure to a three-dimensional one. The original 2D structure can be either a thin easily-foldable substrate, such as paper, a 3D-printed structure made of flexible polymer, or a hard 3D-printed "thick" planar structure with "hinging" features that allow folding [97]. The latter has the advantage of mechanical stability which is important for packaging scenarios, e.g. protecting electronics inside the origami package.

The implementation of an origami electromagnetic structure involves two phases. During the first phase, it is designed and simulated in its final 3-dimensional form. The design is optimized to achieve the desired operating performance (e.g. operating frequency), which, apart from the materials and dimensions, also highly depends on the structure geometry. The second phase involves 'unfolding' the structure to a 2-dimensional pattern that can be easily fabricated. In the case of a cube, it can be expanded to a cross-shaped planar form, shown in Fig. 5.2-top. If the cube has dimensions $a \times a \times a$ and a thickness of $b << a$, the

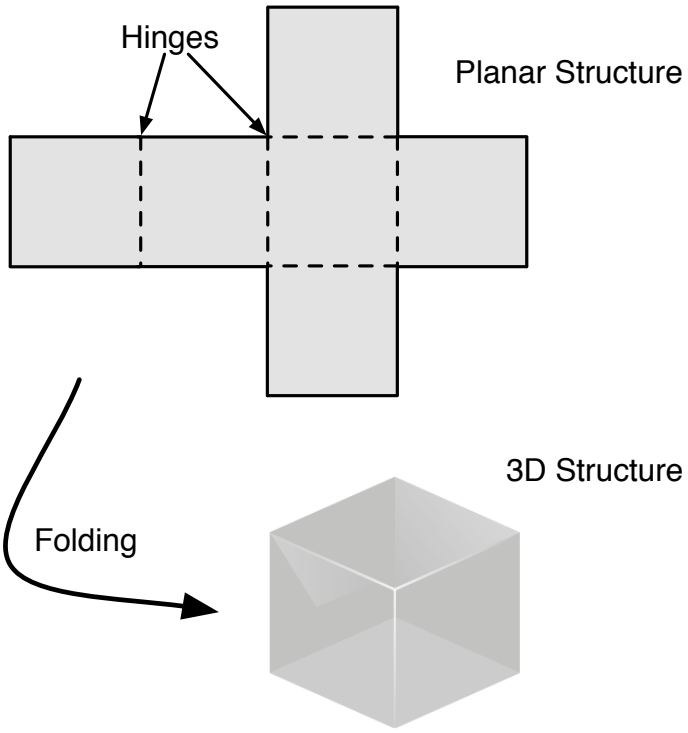

Figure 5.2: Origami folding of planar structure to realize a 3D shape.

fabrication time for a 3D cube is limited by its exterior volume

$$V_{\text{cube}} = (a + 2b)^3,$$

while for the cross shape it is

$$V_{\text{cross}} = 6 \times (a \times a \times b),$$

which is 1 order of magnitude smaller compared to the cube. Thus, the fabrication time can be significantly reduced, and the need for supporting material can be effectively eliminated.

For the metallization of the 3D-printed structure in an additive manufacturing manner, inkjet printing can be utilized. Inkjet printing has proven to be a successful process for realizing low-cost high-frequency structures accurately on a plethora of different substrates, including flexible ones [14]. Printing on 3D-printed surfaces for high frequency sensing

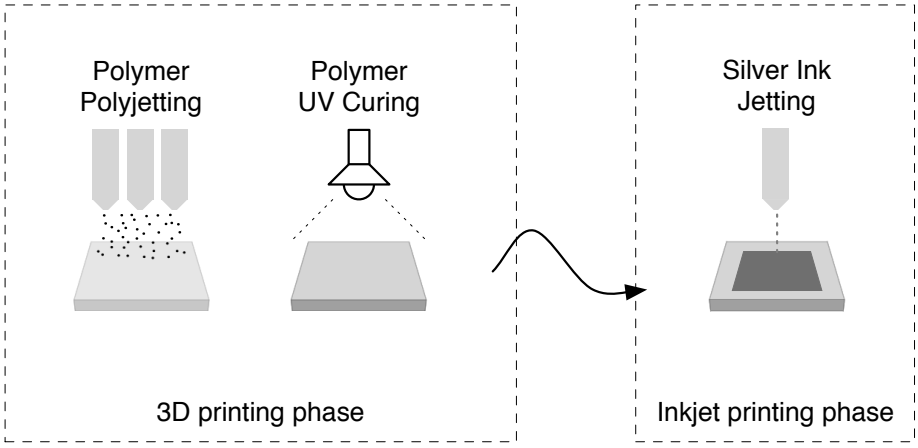

Figure 5.3: All-additive manufacturing: 3D printing of substrate and inkjet printing of conductive features.

and harvesting applications has been demonstrated in [65], showing promising results, even on challenging, rough surfaces.

The combination of 3D printing and inkjet printing can greatly facilitate rapid prototyping, as both are fully additive processes. A significant advantage of this combination is that no post-processing is required after the 3D printing phase to start the inkjet-printing phase. In principle, the two processes could be combined in the same piece of equipment capable of performing a sequence of 3D material deposition and jetting of conductive, semiconductive, or dielectric inks (Fig. 5.3).

A cubic-shape packaging structure prototype has been designed in its final 3D form and has been modeled with the ANSYS High Frequency Structure Simulation (HFSS) software to analyze the performance of its electromagnetic features in high frequencies ($2 \sim 2.6$ GHz band). Since the electronics are contained within the cube, probe-fed patches have been selected as the on-package antennas with coaxial connectors in the interior of the cube. The patches are implemented with microstrip technology, printed on the external sides of the cube, while employing metal ground planes on the respective interior sides. The directivity of patch antennas due to the ground plane limits the electromagnetic coupling between the antennas and the electronics inside the cube. Two patches have been designed on two sides of the cube, so that they face to orthogonal directions (Fig. 5.4).

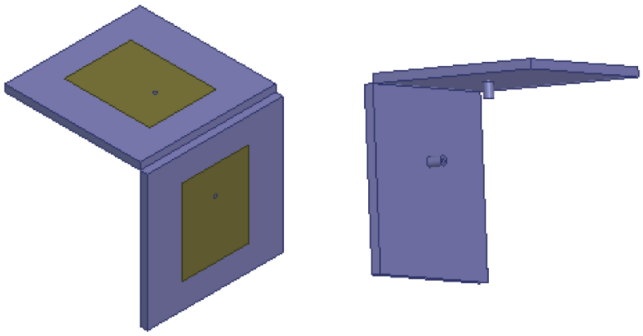

Figure 5.4: Partial views of the package exterior (left) and interior (right).

The cube sides are 5.7×5.7 cm squares and are 3 mm thick. On two of the cube sides patch antennas have been designed around the central frequency of 2.3 GHz. The patch width is $W = 2.79$ cm and its length is $L = 3.59$ cm. The probe feeding point resides 0.63 cm away from the center of the patch, along the L dimension.

Apart from the full 3D structure, a single patch on a substrate with the same dimensions as one cube's side has been simulated. The performance of the single patch and the patches on the cube has been similar, i.e. there are no significant coupling effects between the two antennas on the cube's sides that would degrade their performance (tuning/gain). In principle, an antenna could be placed on any side of the cube without a significant effect on the other sides' antennas.

It is important to note that since the feeding terminals of the two antennas are separate (no RF combining) and the two antennas show a high isolation, their operation is expected to be orthogonal in terms of radiation pattern directivity. In contrast, if the two antennas utilized a common feeding point or if there was a strong coupling, the result would be a beam steering at the far field which would not be desired for the multi-direction operation of the system in Fig. 5.1.

5.3 3D & Inkjet Origami Manufacturing

A 3D-printed packaging prototype has been fabricated using an Objet Connex 260 3D Polyjet Printer. The structural surfaces of the cube are made of the proprietary material

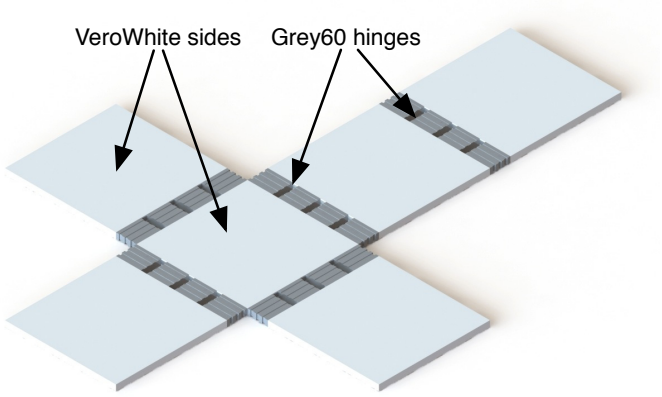

Figure 5.5: Rendering of the flat configuration of the folding package used for 3D printing.

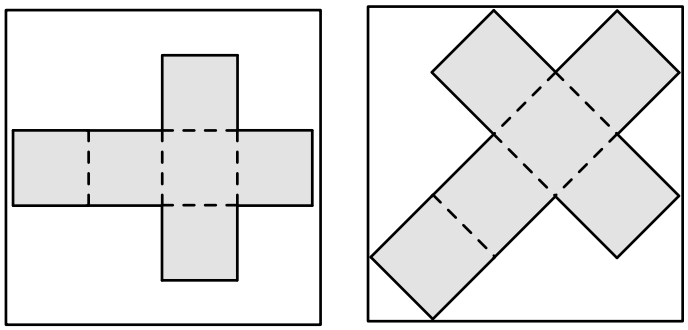

Figure 5.6: Exploitation of the full 3D printer bed for building longer-dimension structures.

VeroWhite and the hinges are Grey60, both thermoset shape memory polymers (SMP). The cube has been printed in its flat configuration to simplify the manual folding process, minimize material consumption, and reduce turnaround time. The model, which has been designed in SolidWorks and is shown in Fig. 5.5, has been printed diagonally on the printer bed to accommodate for the big length across its longest dimension (Fig. 5.6). The materials for printing were chosen to maximize part strength and minimize the required temperature for folding. A novel hinge design has also been employed to reduce material fracture during the manual folding process after heating it up.

Shape memory polymers (SMPs) are polymers that can programmatically change shape "on-demand" [98]. Typically, an SMP is manually folded from an initial primary shape to a secondary shape by applying a mechanical load above the glass transition temperature T_g. The SMP will maintain this deformed shape after subsequently lowering the temperature

below T_g and removing the externally-applied mechanical load. Upon reheating above T_g from the secondary shape, the SMP will self-fold and recover its primary shape [98]. Shape memory polymers recover at different rates (a measure of the shape recovery ratio with respect to time) and at different temperatures (T_g), so material selection is a key design step in achieving desired properties during self-folding. In the case of the folding package designed here, the primary shape is the flat printed configuration and the secondary shape is the manually-folded configuration. For 90° folding, the final shape is a box, while different shapes may result from arbitrary folding angles.

The mechanical properties for the hinge material chosen in designing the folding box are shown in Fig. 5.7. The hinges and structural surfaces of the box have been selected to be as stiff as possible amongst the available Objet materials for part strength. The structural material has been chosen to have a significantly higher T_g than the hinge material to eliminate undesired deformations during heating. The low T_g of the hinge material has also been chosen to reduce the ambient environmental impact on the assembled device during heating and cooling cycles. The T_g was determined using a Dynamic Mechanical Analyzer (DMA, TA Instruments, Model Q800) and examining the $\tan(\delta)$ (ratio of loss modulus to storage modulus).[1] For Grey60, the T_g is 55°C. For VeroWhite, the T_g is 70°C and the Young's modulus is 1.2 GPa [97, 99]. The recovery rate is important for the actuating material and is approximately 4.5 seconds for 100% recovery, as it can be seen in Fig. 5.8.

Transitioning from the flat primary shape to the cube shape is generally achieved by heating and subsequently manually deforming the part by hand. This process subjects the hinges of the folding box to irregular and random stress patterns, increasing the likelihood of part failure. To improve the damage tolerance during folding a periodic step profile was employed along the surface contour of the hinge (Fig. 5.9). Thinner stepwise sections require lower bending stress and have higher thermal conductivity, making the folding box

[1] Not to be confused with the dielectric loss $\tan\delta$. Storage modulus: measure of elastic energy of material or energy stored during sinusoidal stretching. Loss modulus: measure of viscous energy of material or energy dissipated as heat during sinusoidal stretching.

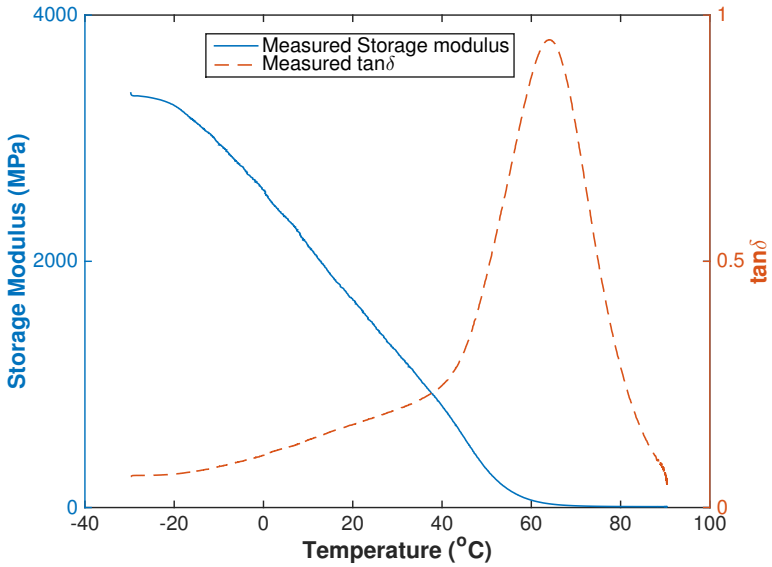

Figure 5.7: DMA (Dynamic Mechanical Analysis) of Grey60 yielding T_g of $55°$C.

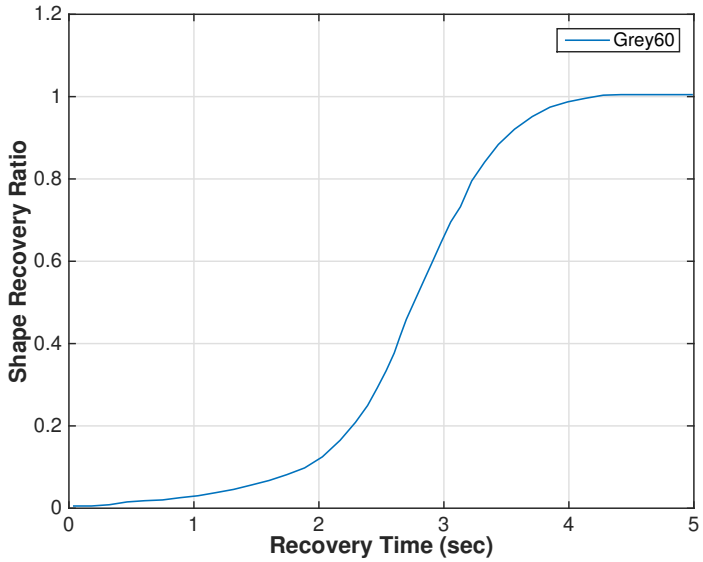

Figure 5.8: Shape recovery ratio vs. time for Grey60.

both easier and faster to fold. Additionally, the periodic profile allows for a wider range of bending motion during folding since the hinge is not subject to restrictive compressive strains. The hinges feature slots to form independent bending sections along themselves and improve their longevity in case of minor fractures (Fig. 5.9). The hinge radius has been maximized to further simplify the manual folding process. Given the dimensional

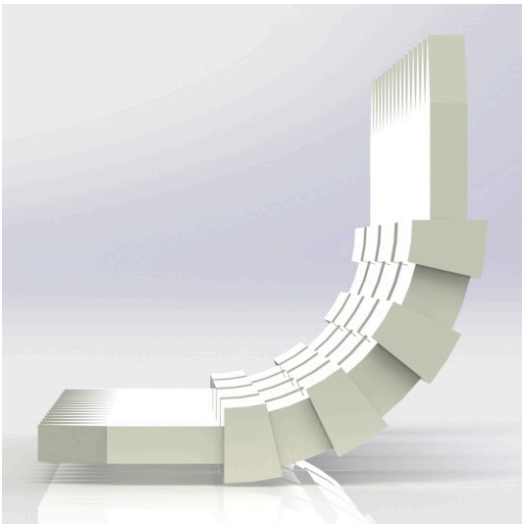

Figure 5.9: Rendering of the hinge design in a 90° folded orientation.

constraints of the structural faces of the folding box and the build volume of the Objet Connex 3D Inkjet Printer, the highest achievable bend radius of 10.5 mm was chosen.

The main challenge for the effective metallization (to realize transmission lines, printed circuits, or antennas) is the direct inkjet printing of conductive features on the 3D-printed surface before folding. This is advantageous for the simplification of the fabrication process:

1. No post-processing is required, such as surface treatment between the 3D and inkjet printing phases, or use of dielectric layers to smooth the surface before metallization. This is in contrast with inkjet printing on top of silicon integrated circuits (ICs), where the printing of supporting layers is required [100].

2. Inkjet printing while the structure is still in planar form facilitates and further simplifies printing; the conductive ink drops are deposited vertically in a conventional inkjet printing manner and no high-pressure aerosol jetting techniques are required. Moreover, the thickness of the planar structure (on the order of millimeters) allows for the easy placement of the substrate between the printing bed and printing head; most inkjet printers are limited on the maximum height of the print head since they are mainly designed to accommodate thin substrates and not high 3D structures.

It has to be stressed that the 2D inkjet printing process, that has been widely used for the printing of nanoparticle-based (e.g. silver nanoparticle-SNP, dielectrics, carbon nanotube) inks on photo paper, polyimide films, glass, and other substrates, has to be redefined to address the two main challenges regarding 3D-printed surfaces

- 3D-printed surfaces show extensive surface roughness that results in the formation of non-continuous features for a small number of SNP layers. This results in non-conductive or low-conductivity printed features, due to the discrete drop formation.

- Typically, SNP inks need to be sintered at temperatures higher than 120° C to maximize conductivity [69]. However, high temperature levels cannot be tolerated by commonly utilized 3D-printed plastics or resins, causing deformation of the structure or failure (melting).

The above constraints require a modification of the inkjet printing process, which cannot be based solely on SNP inks for the realization of conductive surfaces.

For the metallization on 3D-printed surfaces, a diammine silver acetate (DSA) ink is used that achieves high conductivity values with moderate temperature curing (ranging from room temperatures up 100°C) [101]. The low temperature range is safe for plastics, and, thus, this is the principal ink used for the fabrication process. Moreover, the DSA ink does not contain any nanoparticles; the particle formation occurs on the substrate after printing. This results in a very low-viscosity ink that spreads easily on the surface and forms continuous conductors. The measured surface tension of the DSA ink is 23 mN/m, which matches the measured surface free energy of the VeroWhite substrate, which is 22 mN/m.

To avoid over-spreading of the DSA ink, SNP ink is first printed on the substrate to form the patch area. Two layers of SNP form a mesh of discrete drops that can be seen in Fig. 5.10-(a). This is anticipated, since the measured surface free energy of the VeroWhite is 22 mN/m, while the surface tension of the SNP is between 28 and 31 mN/m [102]. Then, the DSA ink is printed on top of the SNP drops. Due to its low viscosity, it fills

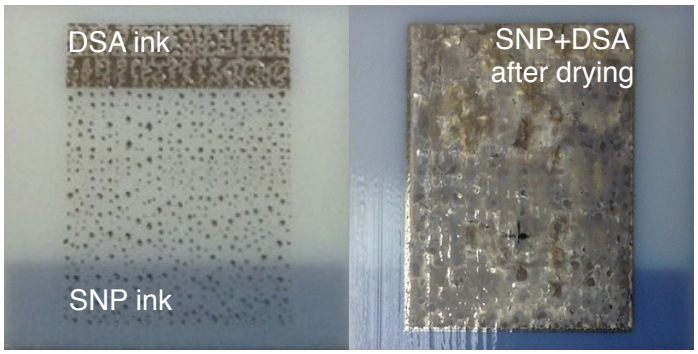

Figure 5.10: (a) Silver nanoparticle (SNP) ink layer with partial diamminesilver acetate (DSA) ink layer on top. (b) SNP+DSA patch after heat-drying.

the gaps between the SNP drops, forming a continuous conductor. Up to twenty layers of DSA are printed, to achieve high conductivity. After each layer printing, moderate heat drying follows to guarantee DSA curing uniformity. After the process consisting of printing the SNP layers and printing/drying the DSA layers is completed, the result is a uniform conductor on top of the 3D-printed surface, without any ink spreading. It is worth mentioning that no significant effect of poor adhesion between the conductive patch and the polymer substrate was observed, and thus no effects of "flaking" were experienced. A fully-cured silver patch can be seen in Fig. 5.10-(b).

In [101], the electrical performance of the DSA is analyzed. Here, a characterization is offered for conductive features formed by inkjet-printing DSA and SNP inks. To characterize the sheet resistance of the DSA ink depending on the number of printed layers, various identical geometry samples have been fabricated with different (5, 10, 15, and 20) layers of DSA, with and without the two SNP layers and the samples' sheet resistance (in Ω per square) is shown in Fig. 5.11. It can be seen that for both cases, the first 15 layers are critical for reducing the total sheet resistance, while the SNP+DSA combination always features a lower sheet resistance for the same number of DSA layers, compared to the DSA-only case. Although this might be anticipated due to the extra silver content for the SNP+DSA case, it is noted that for the DSA-only structures, more than 5 additional DSA layers are always required to achieve similar sheet resistance levels with the SNP+DSA structure. This is

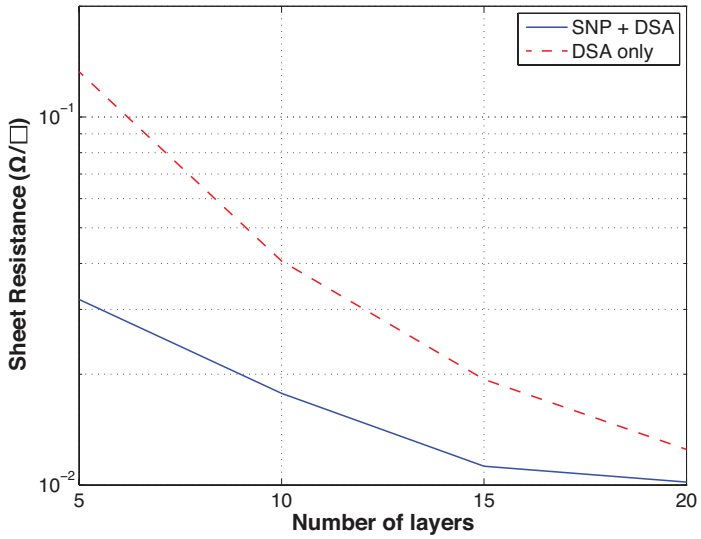

Figure 5.11: Comparison of sheet resistance between DSA-only and DSA+SNP metallization.

a significant observation, considering that the SNP layers are not fully cured to maximize their conductivity, since heating temperature is kept at levels below $100°$C.

On top of the fact that the SNP layers lower the resistance of the printed features, it has been concluded from multiple printing experiments that the SNP layers have the advantage of preventing ink "bleeding", and thus the SNP step is always favorable for the fabrication of any structure.

A proof-of-concept patch antenna prototype has been fabricated with 2 SNP layers and 20 DSA layers on a 3D-printed slab that has the same dimensions as the designed cube's sides (5.7×5.7 cm, thickness $= 3$ mm) for prototyping. On the top side of the slab, the 2.79×3.59 cm patch has been printed, which has a thickness around 20 μm. The bottom side has been covered with adhesive copper tape, to form the ground plane of the antenna for the reason of fabrication simplicity. It is noted that since the ground plane does not require an accuracy of the same level as the patch regarding its dimensions (width, length) or placement (origin point), the copper tape is a convenient way to implement it for proof-of-concept purposes. However, silver ink could be used for the ground plane fabrication as well, since it has been previously demonstrated to perform well for ground plane formation,

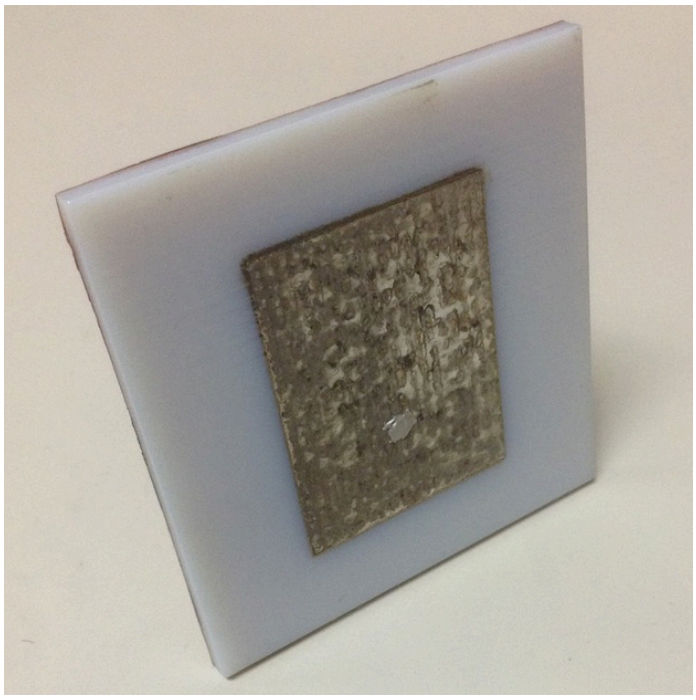

Figure 5.12: Single patch antenna fabricated on 3D-printed substrate.

even with meshed designs [103].

A 36 mil hole has been drilled 0.63 cm away from the center of the patch to accommodate the feeding pin. The hole has been drilled with a conventional drill press, and the exact drilling point has been marked by inkjet-printing a fiducial point with black ink after the metallization process. Such a fiducial point can be seen in Fig. 5.10-(b) as a black cross. An SMA connector has been mounted and its signal pin has been trimmed to match the height of the antenna plane. A conductive silver epoxy has been used to electrically connect the probe pin to the inkjet-printed silver, and at the same time provide mechanical support for the SMA connector at the backside of the plastic slab.

The same patch antenna has been printed on two orthogonal sides of the cube, to realize the multi-direction harvesting/communication system, as shown in Fig. 5.14-(a). The two antennas have been printed with the same process, apart from the drying temperature. For the first antenna, a heatgun with a temperature of approximately $80°$C has been used for 2 minutes, while for the second antenna, the heatgun is set to $50°$C. The different curing

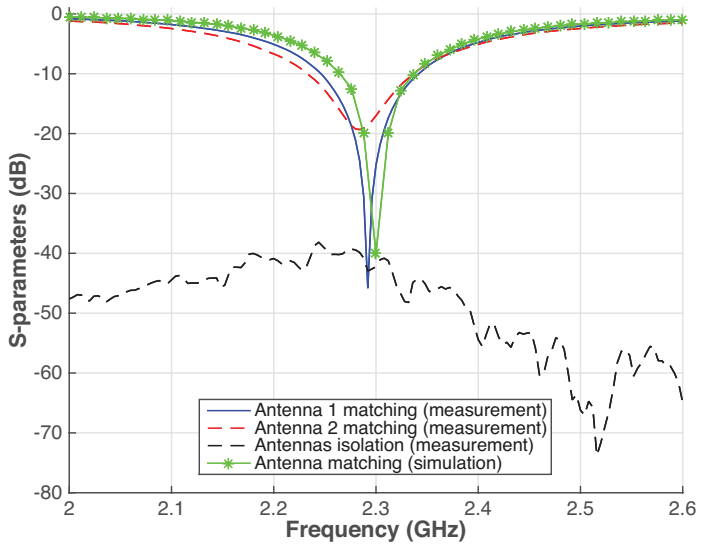

Figure 5.13: S-parameters of the patch antennas.

temperature is used to assess the effect of the temperature level on the antennas' performance. After the antennas fabrication, the structure is heated and folded to its 3D form (Fig. 5.14-(b)).

5.4 Printed Antenna Measurements

The two antennas have been characterized with a vector network analyzer (VNA) as a full 2-port system, rather than two individual antennas. The measured S-parameters are shown in Fig. 5.13. Both antennas are tuned around 2.3 GHz and exhibit the same -10 dB bandwidth of 100 MHz. It is noted that the first antenna shows a return loss (RL) of less than -40 dB at the resonance frequency, while the second antenna shows a RL of -20 dB. This is attributed to the different heatgun drying temperatures used for the antennas that affects their conductivity; the higher $80°$C temperature visibly benefits the RL. However, it is noted that even the lower temperature of $50°$C is more than sufficient for high conductivity, since 99% of the power exciting the antenna port is delivered to the antenna.

For the two antennas, a strong requirement is the isolation between them to guarantee an orthogonal operation across the frequency band. An isolation of more than 40 dB is

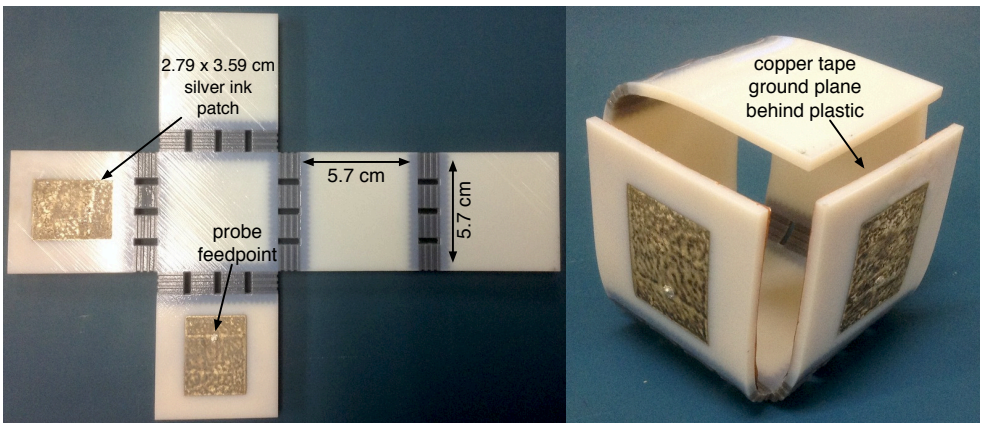

Figure 5.14: (a) Inkjet-printed patch antenna on unfolded 3D-printed cube. (b) "Origami"-folded cube after heating, folding, and cooling down.

achieved between the two fabricated patches (Fig. 5.13), and thus the effect of each antenna to the other is negligible. This is the combined result of both the geometry of the setup (the antennas are placed in perpendicular planes) and the radiation pattern (directive) of the patches.

The realized gain of each patch antenna has been characterized using a VNA and standard horn antennas in a lab environment. The measured maximum gain across the frequency band is shown in Fig. 5.15, where is can be seen that the fabricated patch achieves gain values of up to $4 \sim 4.2$dBi at the resonance frequency.

The cross-polarization isolation (comparison between horizontal polarization field and vertical polarization field) is also measured by rotating the patch by 90° with respect to its center. As it is shown in Fig. 5.16, an isolation on the order of 25 dB or more is achieved in the $2.2 \sim 2.4$ GHz antenna operation band.

5.5 Multi-source RF Energy Harvester

As a proof-of-concept demonstration of utilizing additively manufactured origami structures for RF applications, a 2-port multi-direction RF energy harvester is designed, that exploits the independent inputs from the two orthogonal on-package antennas. The constraints for the design of a harvester for such a system are:

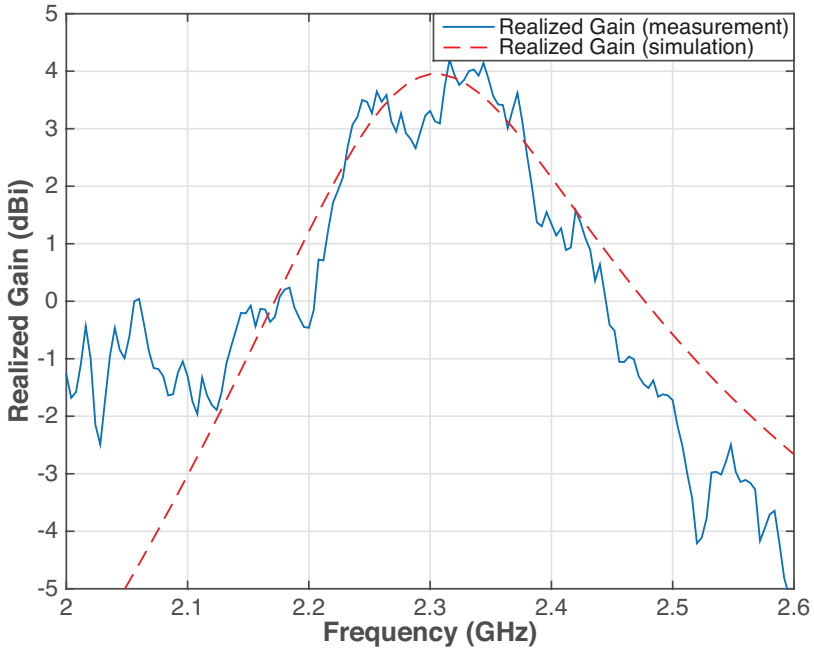

Figure 5.15: Measured and simulated realized gain of a single inkjet-printed patch.

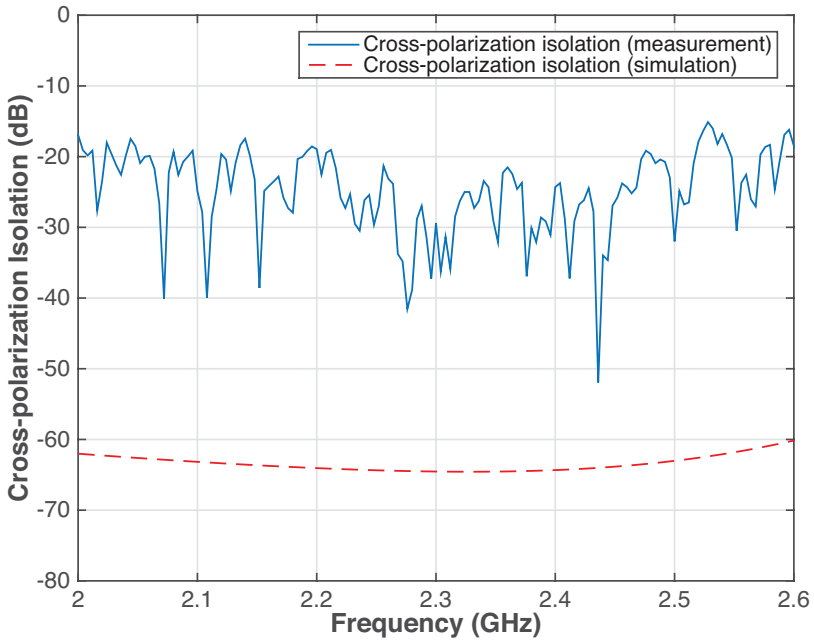

Figure 5.16: Measured and simulated cross-polarization isolation of a single inkjet-printed patch.

- The isolation between the two antennas is crucial, or else a far-field beam steering may occur for the total radiation pattern.

- The ability for the harvester to operate its two ports independently, without constraining both ports at the same time to a specific input power level, incoming signal frequency, and signal phase coherence.

The above constraints are addressed by using a dc-combining topology for the harvesting system, where each port has an individual RF-dc converter (rectifier) and the output voltage of the converters are combined to yield a higher voltage level. A dc combiner, in contrast with an RF-combining topology (e.g. an antenna array with a single RF feeding point), tends to "hide" the characteristics of the incoming RF signal at the dc output of each port's harvester. In that way, different input power/frequency/phase induced RF voltages are converted to dc voltages and combined to a single dc output.

To simplify the dc-combining topology, the outputs of the two harvesters are directly connected at the load-driving terminal without any summation network utilizing resistors, diodes, or field effect transistors (FETs). That way, the losses due to resistive elements or parasitics of the summation network are minimized. Considering a single harvester represented as a current source with output impedance R_H driving a load R_L, and two identical harvesters connected in parallel and driving the same load R_L, the voltage gain for the 2-port harvester compared to a 1-port harvester is

$$\frac{V_2}{V_1} = \frac{R_L + R_H}{R_L + R_H/2}. \tag{5.1}$$

Asymptotically, the maximum voltage gain that can be achieved for equal power RF inputs is 2, achieving double the voltage for driving the load R_L (Fig. 5.17).

The designed 3D multi-direction harvester consists of two rectification circuits with their dc outputs combined at a single dc terminal that drives the load. Whether a voltage doubler topology or a single diode harvester topology is preferable has been determined through ADS simulations. One model for each case has been designed, based on full wave circuit board simulation, non-linear diode models, and lumped component models with

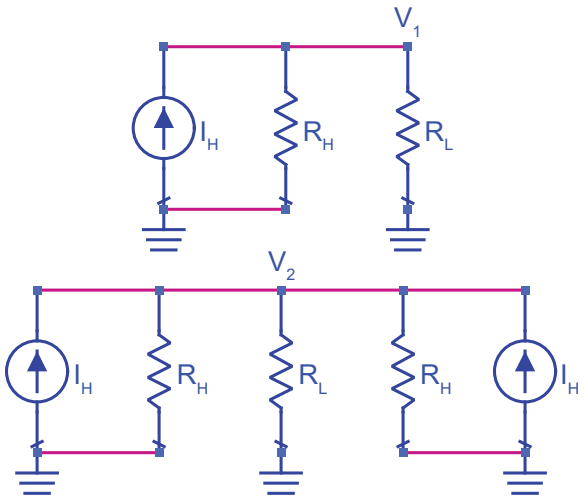

Figure 5.17: Summation of two harvesters' outputs. Top: Single harvester. Bottom: Double harvester.

parasitics. Both designs have been optimized for S-parameters tuning at the same frequency and input power level (2.3 GHz/ -15 dBm). However, while sweeping across different frequencies in the $2 \sim 2.6$ GHz band and power levels from -30 to 0 dBm, it has been noticed that in the case of the voltage doubler the resonance point occurs around 2.3 GHz with little or no shift for any power level. In contrast, for the single diode harvester, the resonance point will be strongly detuned in frequency depending on the power level. Thus, the voltage doubler topology is selected, since it can accommodate for small frequency shifts due to fabrication tolerances.

A single-stage voltage doubler is utilized at *each* antenna port for the RF-dc conversion (Fig. 5.18). Each voltage doubler uses two Avago HSMS-285 zero-bias Schottky diodes in a standard detector configuration, as described in the manufacturer's datasheet. However, any RF-dc conversion circuit could be used in the place of this voltage doubler, according to the needs of the application (e.g. increased bandwidth, different input power levels, etc). At the output terminal, a large 0.22 μF dc capacitor is used for smoothing, along with a high-frequency 6.8 pF capacitor that operates below its self-resonance frequency, and thus is effective for smoothing high frequency signals. A small load of $R_L = 2$ KΩ is driven by the harvester output. Load values of this order of magnitude can be found in devices such

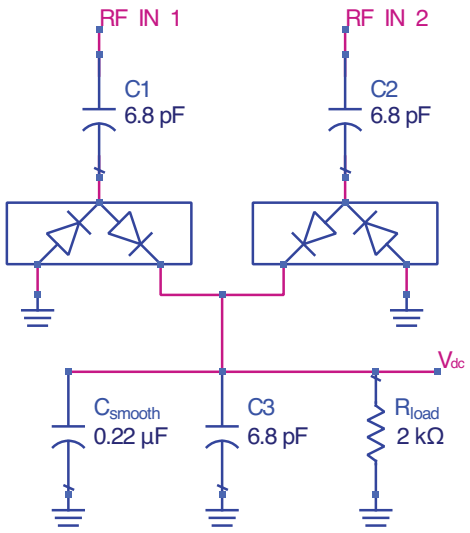

Figure 5.18: Schematic of the 2-port harvester with dc combining.

as low-power microcontrollers that can be used for various WSN node implementations featuring sensors, backscatter communicators, etc.

The 2-port harvester has been designed and simulated with the Agilent Advanced Design System (ADS) software, using large signal S-parameters (LSSP) and harmonic balance (HB) simulations. Non-linear models have been utilized for the diodes, and the passive components have been simulated with models that include parasitics. The harvester has been implemented on a thin Rogers RO4003C laminate and can be seen in Fig. 5.19. The tuning of the ports at 2.3 GHz is performed with single stub matching networks that are implemented on the same board for minimizing losses due to connectors, and to minimize the total electronics' volume. Since the diodes utilized for harvesting typically show a high impedance (and thus mismatch) for low input power levels, the matching network was designed to maximize the power transfer from the antennas to the harvester in low power levels where no power could be compromised. The input power level of -15 dBm has been selected, at which, usable output voltage levels on the order of millivolts are achieved.

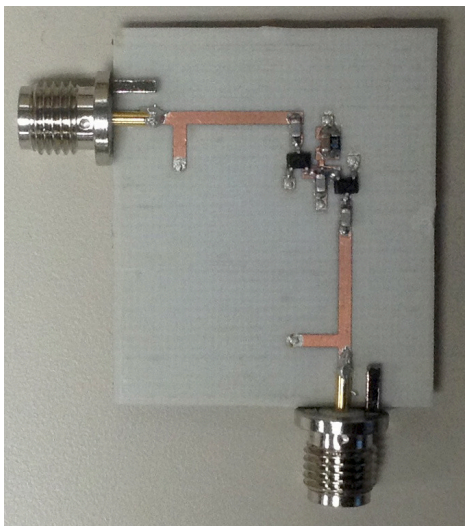

Figure 5.19: Fabricated harvester prototype with on-board matching.

5.6 Harvester Measurements

The 2-port harvester prototype has been fully characterized using a VNA across the $2 \sim 2.6$ GHz band for power levels up to 0 dBm. The matching for both ports is optimal at -14.5 dBm RF input at each port, with both ports tuned around 2.3 GHz, as it can be seen in Fig. 5.20. The -10 dB bandwidth is wider than 120 MHz and the ports show a slight resonant frequency difference between them. The isolation (insertion loss, IL) between the two ports is more than 45 dB over the entire bandwidth; the high RF isolation between the two ports, due to the dc connection point, guarantees the individual operation of the two harvesters regardless of the exact frequency and power level incident at each port.

In Fig. 5.21, the return loss of one of the harvester's ports is shown as a function of both the frequency and the power level of the incident wave on a contour plot. The resonant point at 2.3 GHz/-14.5 dBm can be clearly observed. Moreover, the "oval"-shaped contours centered centered around the resonant point show that for any given power level, the return loss minimum always occurs around 2.3 GHz, as discussed previously for the voltage doubler architecture.

In Fig. 5.22 it can be seen that across the whole frequency band and for any power

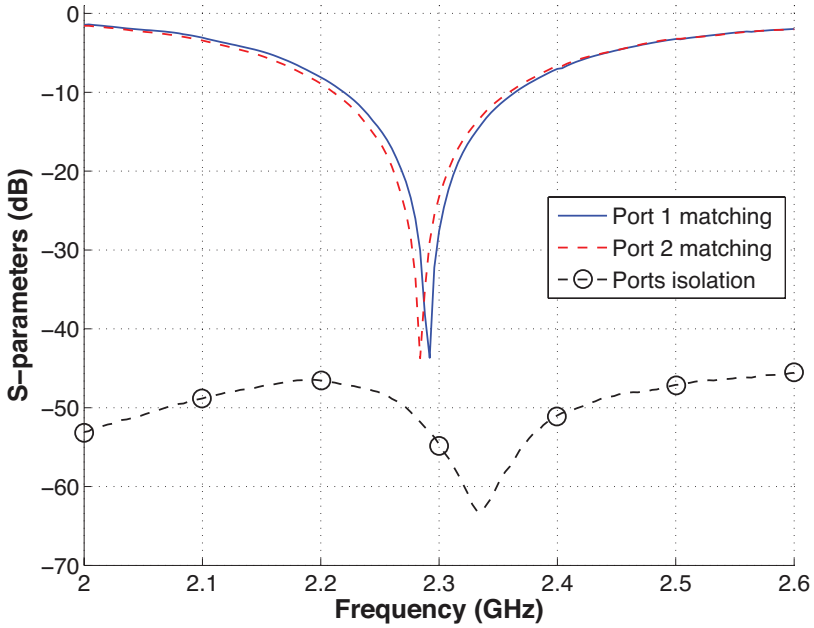

Figure 5.20: Measured harvester ports' return loss and coupling (input power level: -14.5 dBm).

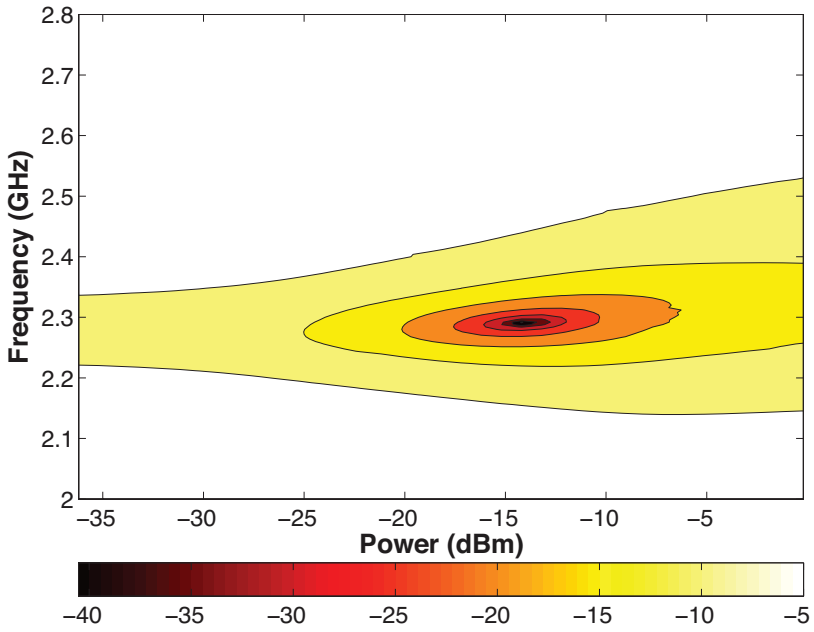

Figure 5.21: Harvester port matching across frequency band and input power levels. Resonance around -14.5 dBm/2.3 GHz.

level, the isolation between the two ports is always higher than 45 dB, with certain points reaching isolation values of 70 dB.

The device has been excited in three different scenarios to measure the output voltage:

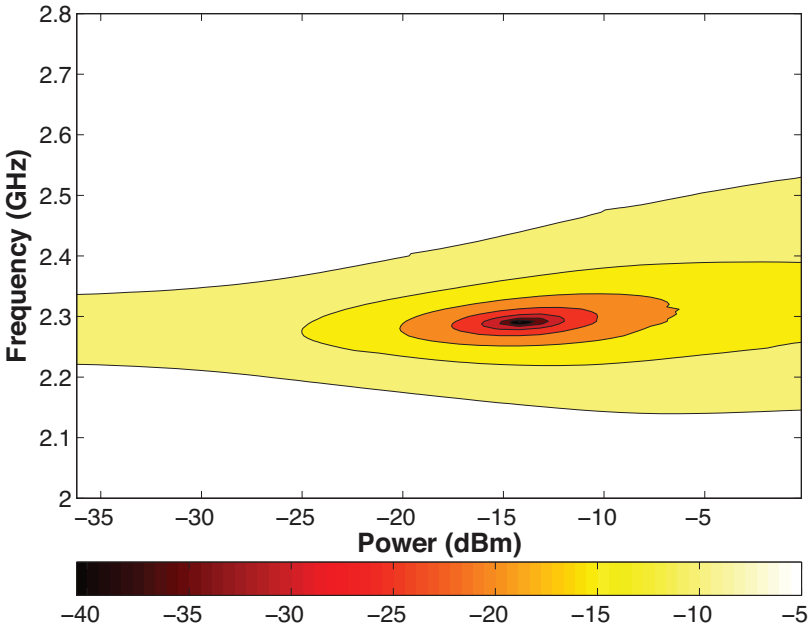

Figure 5.22: Harvester port isolation across frequency band and input power levels. High isolation (more than 45 dB) for all points.

port 1 only, port 2 only, and both ports excitation. In Fig. 5.23, the simulated output voltage for different input power levels is shown, along with the measured values in these three scenarios. The wired measurements match with the simulation results; as an example, at -15 dBm a voltage level of 100 mV is achieved for the 2 KΩ load when one port is excited. When both ports are excited, the voltage level is boosted to 150 mV. When the ports are excited with high power (0 dBm), the output voltage reaches 1.2 V, even though the harvester is not optimized for high input power operation.

After characterizing the harvester and the packaging individually, everything is connected together for an evaluation of the final system. The electronics are placed inside the cube, connected to the patch antenna ports with short, flexible coaxial cables (Fig. 5.24). Since the cables are in close proximity inside the package, the coupling between them is measured in extreme scenarios, such as twisting the pair of RF cables together, or running them in parallel. In all cases, the coupling between the cables was lower than -70 dB, and no specific setup of the cables was required in the package to minimize cross-port interference.

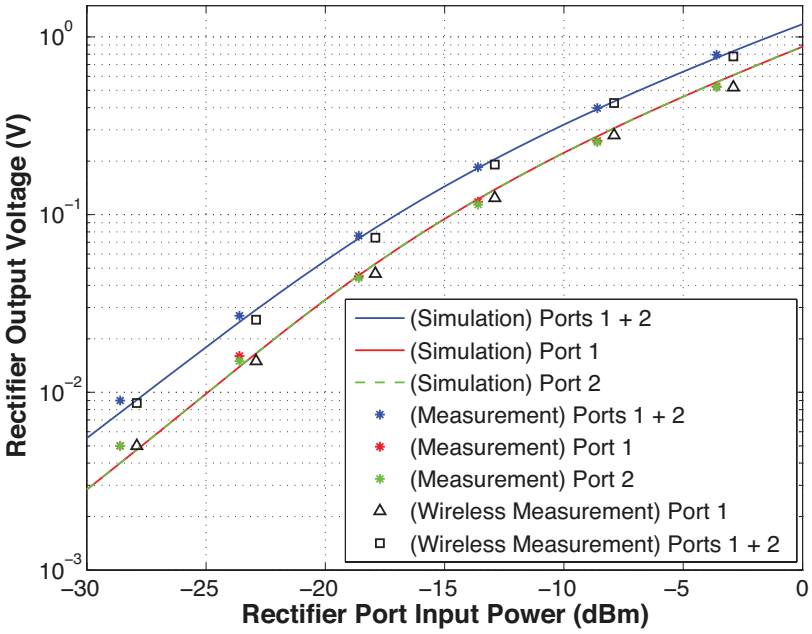

Figure 5.23: Harvester output voltage versus port input power.

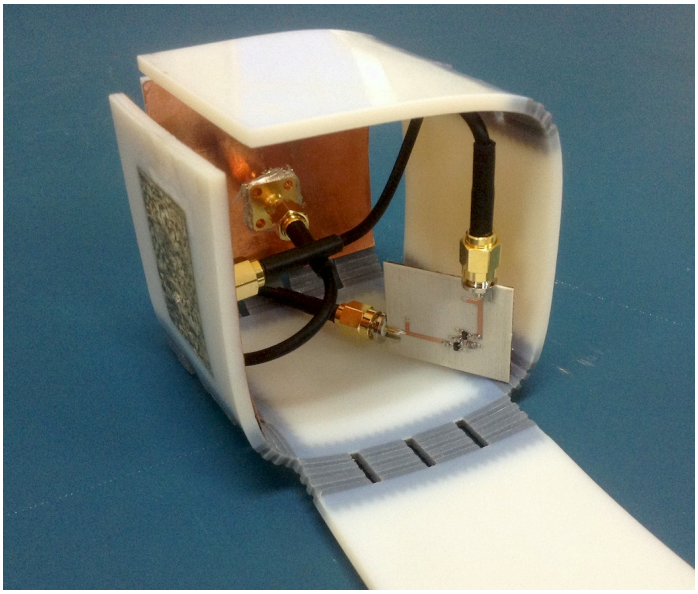

Figure 5.24: Origami package with harvester electronics inside.

A software-defined-radio (SDR) with tunable output power was set up to transmit a 2.3 GHz constant wave (CW) from two ports that were connected to two horn antennas. The horn antennas were chosen for their high directivity, to create plane waves at at specific directions in the far field, i.e. to eliminate any reflections from side- or back-lobes that could

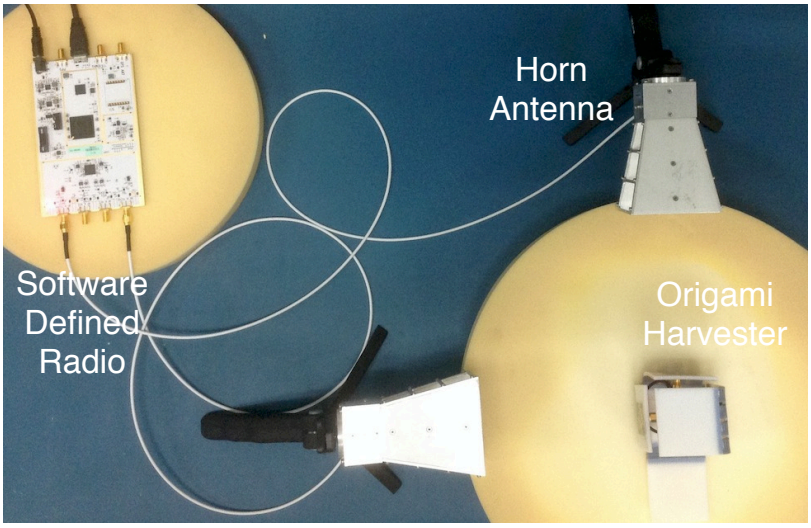

Figure 5.25: Wireless measurement setup for the origami RF harvester.

potentially excite both patch antennas instead of only the targeted one. The horn antennas were in an orthogonal configuration, to excite one patch each, and at the same distance, to keep path loss at similar levels (Fig. 5.25).

The inkjet-printed patches have been illuminated by the horn antennas at several power levels, while the power induced at each antenna's terminals has been monitored with an RF power meter to precisely monitor the input power to the harvester at each case. After connecting the harvester to the origami antennas, the output voltage has been recorded for each power level. The wireless measurements curve fits with the simulation and the wired measurements one, verifying the system operation with the inkjet-printed antenna on the 3D-printed, "origami"-folded cube (Fig. 5.23).

CHAPTER 6

FLEXIBLE PRINTED FRONT-ENDS FOR UWB HARVESTING

Typically, most wireless energy harvesters are tuned around a specific frequency to increase RF-dc conversion efficiency, which is a straightforward choice when a dedicated power source of given frequency is available. However, the high availability of stray RF signals from various emitters, with different frequencies and bandwidths offers a diverse combination of wireless power sources for small smart home devices, IoT sensors, and wearables. Wideband harvesting front-ends could then benefit a scenario where IoT devices are agnostic to the RF power sources around them. Recent publications of dual band, triple or quadruple band rectifier circuits include [59, 104, 105], and during this thesis an ultra-wideband (UWB) energy harvesting front-end is designed, with the additional requirements of miniaturization and flexible substrate implementation, for integration with wearables and conformal electronics.

A non-uniform transmission line in series with a lumped inductor L_1 was chosen to implement the impedance matching network for the introduced ultra-broadband rectifier. Non-uniform transmission lines have been traditionally used to provide broadband matching to real loads as shown in [106, 107]. In addition, they can be used to provide dispersion compensation in optical communication links [108]. Here, a series inductor is first used to provide narrowband matching and cancel the capacitive imaginary part of the rectifier impedance around a certain frequency within the band under consideration. Then a non-uniform transmission line transforms the low-imaginary-part complex impedance to the desired $50\ \Omega$ source impedance. The matching network is shown in Fig. 6.1. A microstrip line consisting of trapezoidal sections was used to implement the non-uniform transmission line, which facilitates single-layer, inkjet printing fabrication.

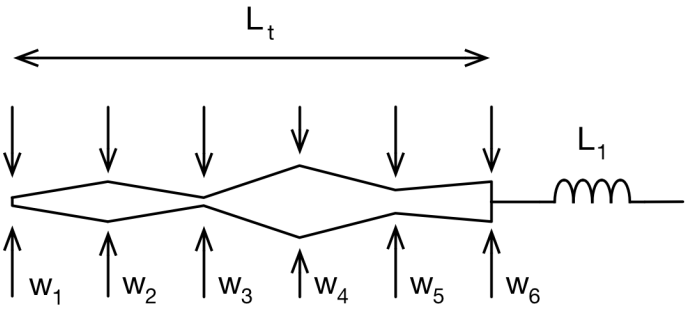

Figure 6.1: Rectifier impedance matching network consisting of a series inductor and a non-uniform transmission line.

6.1 Decade-bandwidth flexible RF harvester

The rectifier RF-dc conversion efficiency is defined as

$$\eta = \frac{P_{\text{dc}}}{P} \tag{6.1}$$

where $P_{\text{dc}} = V_L^2/R_L$ and V_L is the output dc voltage and R_L is the output load resistance. P is the available RF power at the input of the rectifier. The efficiency η is maximized over the broadest desired frequency band for a given input power P using harmonic balance optimization while optimization parameters include the non-uniform transmission line dimensions, the inductor L_1, and the load R_L.

A decade bandwidth rectifier was designed to achieve an optimal operation at 3 GHz with an inkjet printing implementation on a flexible polyimide (Kapton) substrate with dielectric constant $\epsilon_r = 3.4$, loss tangent $\tan\delta = 0.0025$, and 5 mil thickness. A two-diode rectifier is designed to drive a load of $1.3\ k\Omega$ with an input power level of as low as -10 dBm. A Skyworks SMS7630 Schottky diode was used for the design, and the circuit of Fig. 6.2-bottom was analyzed and optimized in ADS with a gradient optimization algorithm. The optimization goal was the maximization of the RF-dc conversion efficiency between 250 MHz and 3 GHz, without any target goal for the return loss. The plastic package model of the diode was used for the simulations, including the parasitic capacitance

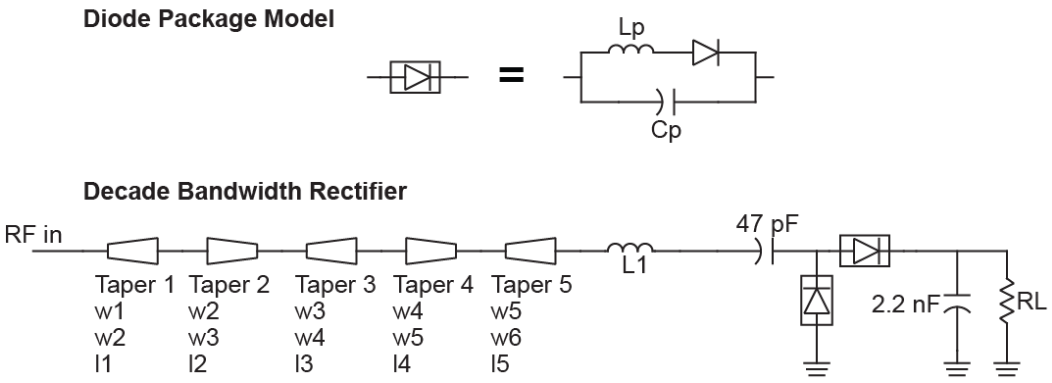

Figure 6.2: Top: SMS730 diode parasitic model. Bottom: Optimization schematic for decade bandwidth rectifier with non-uniform transmission line.

$C_p = 0.25$ pF and wirebond inductance $L_p = 0.6$ nH (Fig. 6.2-top).

A non-uniform transmission line is designed and optimized for the UWB rectifier for decade-broadband matching. The transmission line length is kept significantly low compared to the octave rectifier to minimize the losses of inkjet-printed traces that feature lower conductivity levels (5×10^6 S/m) compared to the copper cladding of standard PCBs (5.8×10^7 S/m). The microstrip line mainly targets the higher frequencies of the band, where diodes typically show low efficiency performance. The effect of matching with the non-uniform transmission line can be clearly seen in Fig. 6.3, where the simulated RF-dc conversion efficiency of the two-diode rectifier driving a 1.3 kΩ load with and without UWB matching are shown for -10 dBm input power. "No matching" refers to the case of directly feeding the RF power to the voltage doubler without the lumped inductor and non-uniform transmission line. It is apparent that with the UWB matching network, consisting of the inductor L_1 and non-uniform transmission line, the average efficiency across the band is increased, with a peak around 1500 MHz that is the center of the band. The peak has a value of 8%, while an average efficiency of 7% spans a very wide frequency region of 3 GHz. This is in contrast with conventional harvesters that are optimized for a specific power and frequency point and achieve higher efficiency values, albeit around a very tuned frequency point. This has a result of a very sharp efficiency decay when the ex-

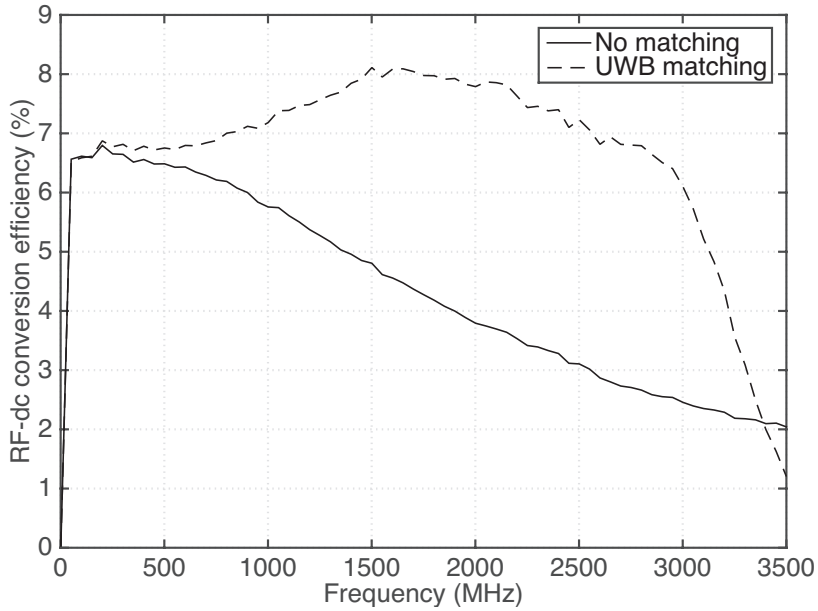

Figure 6.3: Rectifier RF-dc conversion efficiency without and with UWB matching (RF input power -10 dBm, load value 1.3 kΩ).

citation signal is slightly detuned from the precisely-tuned operating point of the harvester. The designed UWB harvester, in contrast, features a steady efficiency value across a very wide band, which can facilitate the design of additional dc-dc converters, supercapacitor charging circuits, and power management units at the output of the harvester.

6.2 Inkjet-printed Harvester Fabrication

Due to the nature of inkjet printing, where high resolution of printed features can be achieved, the smallest required width of the UWB matching line was set to be 100 μm, which can be precisely achieved with inkjet printing. Moreover, for the UWB transmission line, the tapered sections do not all feature the same length, in order to double the degrees of freedom for the design and minimize any potential conductive losses. The line sections? width (w_i) and length (l_i) values as well as the matching inductor value can be seen in Table 6.2. The total line length is less than 1.5 cm, keeping the total system (harvester circuit and line) area less than 2 cm^2.

The fabrication of the decade UWB harvester prototype board, before placing the SMD

Table 6.1: UWB Rectifier Optimization Parameters, P = -10 dBm

Parameter	Value	Parameter	Value
w_1	1.76 mm	l_2	5.95 mm
w_2	0.24 mm	l_3	4.79 mm
w_3	0.11 mm	l_4	2.12 mm
w_4	0.23 mm	l_5	0.1 mm
w_5	3.43 mm	L_t	14.22 mm
w_6	1 mm	L_1	3.6 nH
l_1	1.25 mm	R_L	1.3 kΩ

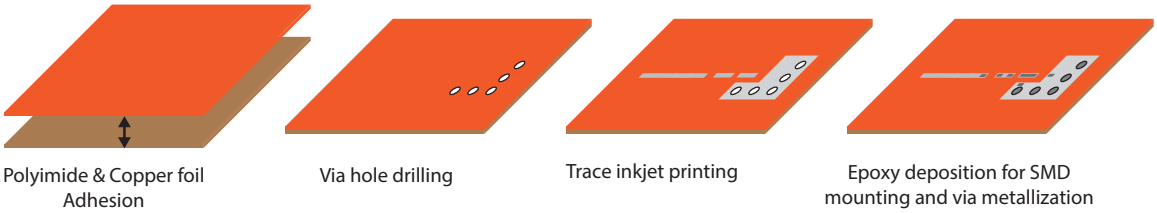

Figure 6.4: Printed board fabrication process.

components (0603 size), involves 4 steps, shown in Fig. 6.4: 1) Substrate preparation by attaching an adhesive copper foil (copper tape) under the polyimide film to form the microstrip ground plane. 2) Drilling to form the holes of the vias required for ground connections. 3) Inkjet printing of traces with a conductive silver nanoparticle ink. 4) Conductive epoxy deposition for via metallization and SMD component attachment. The holes on the substrate are drilled right after attaching the copper tape to the polyimide film and before printing the silver to avoid any cracks on the printed traces (Fig. 6.5-left). Apart from the 0.8 mm-diameter holes drilled for vias, two 2 mm-diameter holes are also drilled to mount an SMA end-launch connector. A Dimatix DMP-2800 inkjet printer is used to deposit droplets of silver nanoparticle (SNP) ink on the substrate to form the traces of the non-uniform line and the circuit component pads. Five layers of silver nanoparticle ink are deposited with 20 μm drop spacing on a 60° C-hot platen and an inter-layer printing delay of at least 300 seconds, to guarantee enough time for SNP ink solvent evaporation which will minimize ink spreading. This is crucial especially for the thinnest parts of the line, where the line width (100 ?m) consists of only 4–5 SNP drops. The board is placed in a

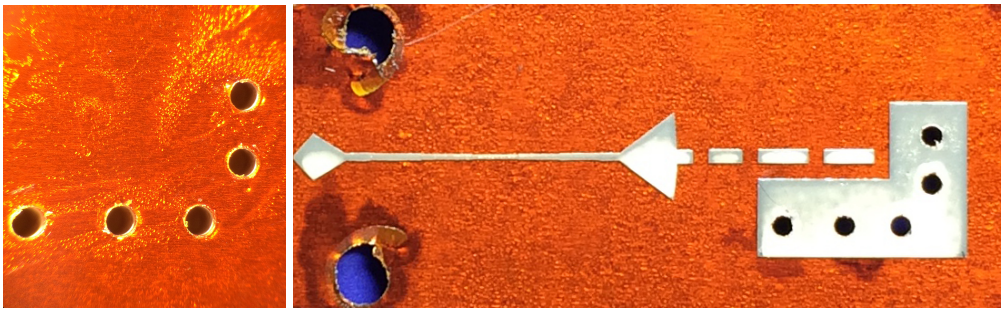

Figure 6.5: Left: Drilled via holes on polyimide and copper tape substrate. Right: Inkjet-printed board; feeding section, non-uniform transmission line, and SMD components pads.

temperature-controlled oven at 180° C for at least 60 minutes to ensure full SNP sintering that will maximize conductivity. The fully-cured board can be seen in Fig. 6.5-right, with the SNP ink printed directly on top of the vias.

It is interesting to note that printing directly on the drilled substrate creates SNP walls in the holes that electrically connect the printed silver traces with the copper ground plane. The resistance between the top silver trace and the copper ground plane is less than $4\ \Omega$. However, a low resistivity silver epoxy ($0.0007\ \Omega \cdot cm$) is used for via metallization to improve operation at high frequencies as well as for SMD component mounting. The epoxy consists of two parts that need to be mixed together to start the curing process. Due to the small SMD sizes (order of millimeters) a controlled dispensing method is needed to precisely deposit the conductive adhesive on the silver traces. A novel method is tested, inspired by solder paste deposition tools, that involves a solder paste deposition pump that applies air pressure to a syringe with a piston for micro-dispensing of paste on circuit traces. Because conductive epoxies are typically two-part materials that start curing immediately after mixing (even at room temperatures), the epoxy chosen has a long working time (4 hr), which is enough for mixing, transferring to a 10 cc syringe tube, and connecting to the deposition pump for dispensing, before starting hardening up to a non-working viscosity level. The pump pressure is set to at least 0.2 MPa to dispense the mixed epoxy with a 26-gauge tip. The via holes are filled with epoxy which accumulates on the via walls, creating shorts between the top printed traces and the copper ground plane. Drops of epoxy

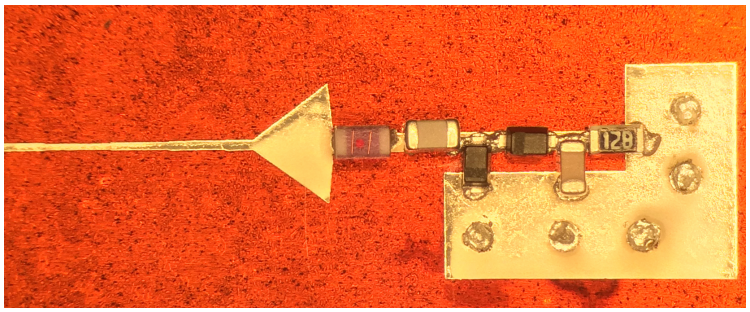

Figure 6.6: Microphotograph of assembled harvester, with SMD components and epoxy-metallized vias.

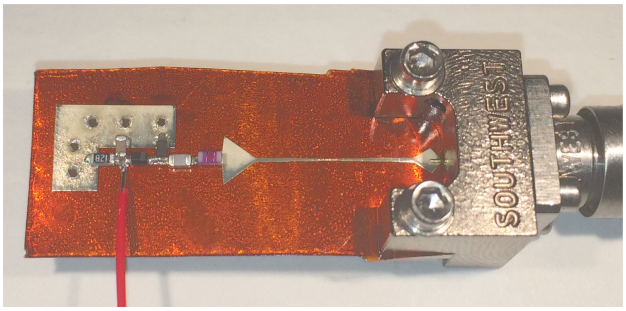

Figure 6.7: Flexible UWB harvester prototype with end-launch SMA connector and V_{out} testing output.

are also dispensed on the printed traces at the positions where the SMD pads are going to be attached. After placing the components, the board is oven-heated at a moderate temperature of 65° C for at least 60 minutes. A microscope photograph of the attached SMD components and metallized vias is shown in Fig. 6.6. The fully-assembled harvester board (2.5x0.75 cm) with the attached end-launch connector is shown in Fig. 6.7.

6.3 Inkjet-printed UWB harvester performance

The VNA-measured S-parameters of the UWB harvester prototype are shown on a Smith Chart in Fig. 6.8 for an input power of 0 dBm, where the input reflection coefficient maintains a relatively stable magnitude across the 300 MHz–3 GHz band. A signal generator and a digital multimeter (DMM) have been used to measure the harvester output voltage level for various input power levels and frequency points. The 2-D function $V_{\text{out}} = f(F, P)$ contours are shown in Fig. 6.9 for the simulated circuit and measured prototype. The x-

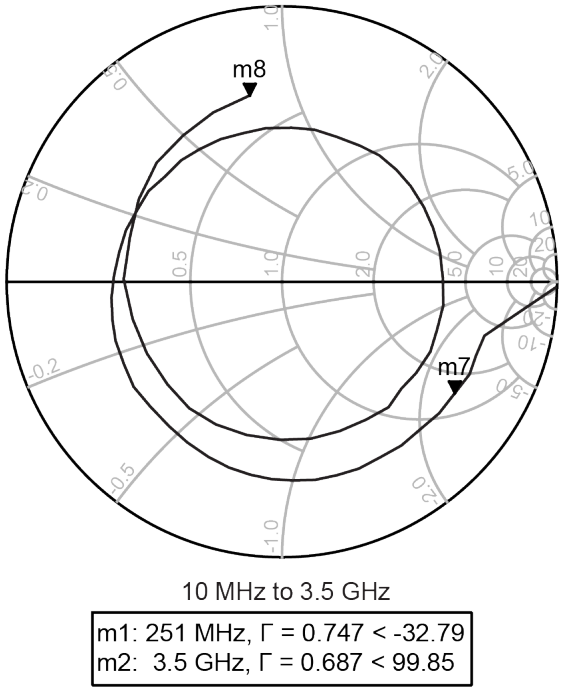

Figure 6.8: S_{11} Smith Chart for input power $P = 0$ dBm and $R_L = 1.3$ kΩ.

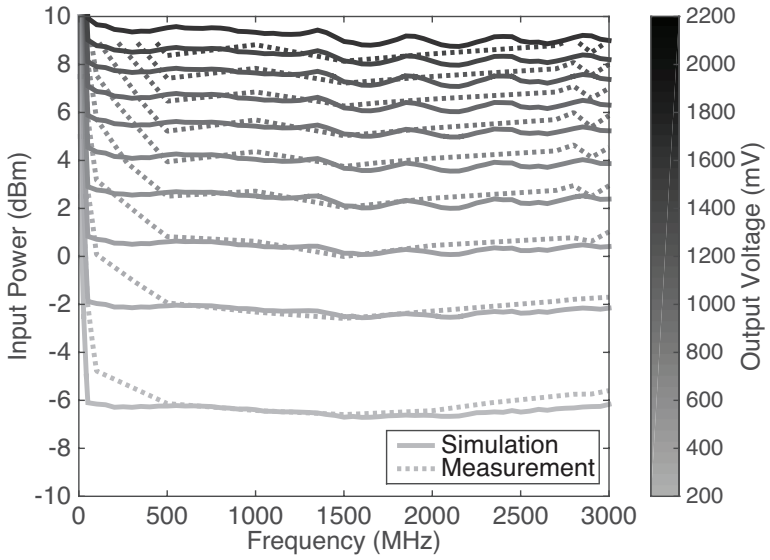

Figure 6.9: Contours of simulated and measured rectifier dc output voltage for varying input power level and frequency values.

axis is the frequency variation and the y-axis is the input power variation. The tone of grey denotes the level (output voltage) of each contour, according to the color bar on the right, i.e. the output voltage increases as the input power increases for a given frequency, and

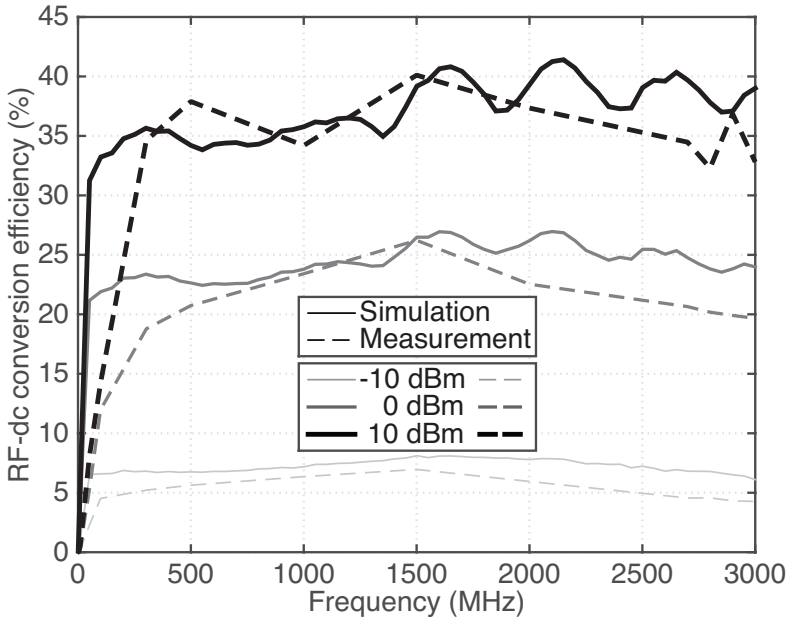

Figure 6.10: Simulated and measured efficiency for inkjet-printed UWB harvester.

the output voltage remains stable across frequency variations for any given input power level. It can be seen that the output power level for a given input power shows very little variation in the whole band of interest between 250 MHz to 3 GHz. In Fig. 6.10, the efficiency across the frequency band is plotted for three input power levels, -10, 0, and 10 dBm. The measured efficiency increases from 6% on average for -10 dBm input power to 37% on average for 10 dBm input power. The efficiency shows small variations within the band between 250 MHz and 3 GHz, between [4.5%, 7%] for an input power level of -10 dBm, [18%, 25%] for 0 dBm, and [32.5%, 40%] for 10 dBm input power. Even though the efficiency is increased for high power levels, there are applications where high-level RF power is available e.g. from handheld devices such as radios. The examples in [109, 110] have successfully demonstrated the exploitation of RF sources in close proximity for powering up wearable devices. The potential of such high power availability is enhanced by enabling an ultra-wideband operation of flexible printed harvesters that can be integrated with wearable IoT sensors and exploit power from handheld radios, cellphones, desktop Wi-Fi access points, etc.

CHAPTER 7

SUMMARY OF CONTRIBUTIONS AND FUTURE DIRECTIONS

7.1 Summary of Contributions

During this thesis, numerous prototypes and proof-of-concept devices were implemented and tested, to push the boundaries of backscatter communication and energy harvesting one or multiple steps further from the prior art. Enhanced scattering efficiency front-ends were shown, increasing the effective communication range in heavily-cluttered environments by more than 25%, extendable to even more in outdoor scenarios. Improved spectral efficiency backscatter modulators were shown that offer a more than 50X (17 dB) improvement in out-of-band sidelobe suppression compared to the prior art by using pulse shaping techniques and square-root raised cosine pulses. These concepts were scaled even more to achieve a big leap in backscatter communication: push backscatter datarate to 2 Gbps by utilizing mmWave frequency bands (24–28 GHz), while keeping a front-end energy-per-bit consumption of $E_b = 0.17$ pJ/bit. Additive manufacturing techniques were used to fabricate front-ends and structures with significant fabrication cost reduction benefits, and Origami principles were used for the first time to reduce fabrication time and cost of bulky 3D packages by 90%. High-resolution inkjet printing facilitated the implementation of UWB RF harvesters with a more-than-decade bandwidth between 250 MHz and 3 GHz and a flat RF-dc conversion efficiency of up to 35%.

Each technology posed its own implementation challenges, which have been covered in the respective chapters. From a higher-level standpoint, this work's main contributions can be summarized to the following achievements:

- Systematic requirements analysis to fully exploit the potential of semi-active backscatter topologies (reflection amplifiers) which had been sub-optimally used until now.

- Enabling tags for the first time to backscatter arbitrary waveforms instead of limiting operation to rectangular pulses and perform complex digital modulations with pulse shaping. Each computationally-enables tag can now be transformed to a miniature software defined radio.

- Demonstration of the first ultrafast Gigabit-datarate digital backscatter system at the mmWave frequency range. By utilizing pulse shaping/arbitrary waveform backscattering principles, high-order constellations can be backscattered without the need for additional transistors/switches.

- Combination of 3D printing and inkjet printing processes with origami principles for the first time to address challenging high frequency electromagnetic problems. Redesign the inkjet printing process to accommodate the idiosyncrasies of 3D-printed substrates with limiting hydrophobic properties and high surface roughness.

- Miniaturization of UWB harvesters that will allow IoT devices to parasitically harvest power while being completely agnostic of the power sources that are available in their proximity.

7.2 Future Directions

This work demonstrated for the first time the mechanisms of achieving multi-Gbps backscatter with miniaturized RF front-ends and antennas in mmWave bands. The potential of picojoule-per-bit communication at those frequencies extends beyond strictly-backscatter sensors. Viewing backscatter communication as "remote" mixing will lead to complexity minimization of commercial devices. For example, with conventional technologies, cellphones will have to upgrade to full 28 GHz radios in order to benefit from the upcoming 5G standards and reach Gigabit data transfer speeds. However, current cellphones already employ 2.4 GHz electronics that could act as an IF bridge between baseband and mmWave frequencies, as explained in Chapter 4, with the addition of a single mmWave transistor.

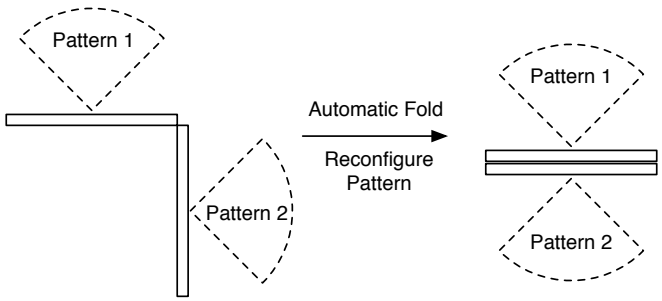

Figure 7.1: Potential for origami technology: shape-changing structures for on-the-fly reconfigurable RF systems and smart wireless sensors.

Backscattering at mmWave frequencies holds a big potential in bringing 5G network compatibility to devices without actually incorporating complete 28 GHz Tx/Rx chains. Scenarios such as cellphone data offloading (e.g. sending photos/videos to cloud storage) at ”hotspots” in cafes or other public places are in line with the concept of ”wireless charging hotspots” that make their appearance in similar locations. Backscatter radio would be a perfect low-complexity implementation for such short-range, rapid-data transfer links.

The origami-folding principles that were explored for packaging and harvesting applications during this thesis is another technology component with great potential. Utilizing origami for RF applications should not be limited to packaging. The ability to change (and retain) the shape of 3D structures opens new paths in electromagnetic applications, especially through *reconfiguration*. Shape-memory hinges can be built either to fold or unfold automatically, with heat triggering, and without manual force. This could enable complex structures to be reconfigured on-the-fly based on the ambient temperature conditions. In that case, smart sensors could be built, that signal rapid changes in temperature by changing their RF characteristics. An example could be directional antennas that change their radiation pattern when automatically folded (Fig. 7.1). In the same manner, reconfigurable antennas, transmission lines, filters, and numerous others RF structures could reconfigure their frequency of operation, gain, bandwidth, or phase. In a different approach, intentional changes of the temperature around the proximity of the system could enable the live, controlled reconfiguration by folding or unfolding the origami structure to tune, for example, a

filter. Beam steering for small antenna arrays by physically changing their geometry without the need for servo motors or manual force could be appealing for low-cost applications. This work demonstrated the feasibility of incorporating origami for RF applications and the methodology presented to additively manufacture complex origami structures will be hopefully enabling the fabrication of numerous other systems for demanding, non-conventional electromagnetic applications from low UHF up to mm-Wave bands.

BIBLIOGRAPHY

[1] J. Kimionis, A. Bletsas, and J. N. Sahalos, "Increased range bistatic scatter radio," *IEEE Trans. Commun.*, vol. 62, no. 3, pp. 1091–1104, mar 2014.

[2] I. Akyildiz, W. Su, Y. Sankarasubramaniam, and E. Cayirci, "Wireless sensor networks: a survey," *Comput. Networks*, vol. 38, no. 4, pp. 393–422, mar 2002.

[3] A. Mainwaring, D. Culler, J. Polastre, R. Szewczyk, and J. Anderson, "Wireless Sensor Networks for Habitat Monitoring," in *Proc. 1st ACM Int. Work. Wirel. Sens. Networks Appl.*, ser. WSNA '02. New York, NY, USA: ACM, 2002, pp. 88–97.

[4] G. Tolle, J. Polastre, R. Szewczyk, D. Culler, N. Turner, K. Tu, S. Burgess, T. Dawson, P. Buonadonna, D. Gay, and W. Hong, "A macroscope in the redwoods," in *Intl. Conf Embed. Networked Sens. Syst.*, San Diego, USA, nov 2005, pp. 51–63.

[5] I. Stoianov, L. Nachman, S. Madden, and T. Tokmouline, "PIPENET: A Wireless Sensor Network for Pipeline Monitoring," in *2007 6th Int. Symp. Inf. Process. Sens. Networks*. IEEE, apr 2007, pp. 264–273.

[6] P. Bauer, M. Sichitiu, R. Istepanian, and K. Premaratne, "The mobile patient: wireless distributed sensor networks for patient monitoring and care," in *Proc. 2000 IEEE EMBS Int. Conf. Inf. Technol. Appl. Biomed.* IEEE, 2000, pp. 17–21.

[7] G. Werner-Allen, P. Swieskowski, and M. Welsh, "MoteLab: a wireless sensor network testbed," in *Fourth Int. Symp. Inf. Process. Sens. Networks (IPSN), 2005*, apr 2005, pp. 483–488.

[8] M. Johnson, M. Healy, P. van de Ven, M. J. Hayes, J. Nelson, T. Newe, and E. Lewis, "A comparative review of wireless sensor network mote technologies," in *Proc. IEEE Sensors 2009*, oct 2009, pp. 1439–1442.

[9] E. Kampianakis, J. Kimionis, K. Tountas, and and A. Bletsas, "A Remotely Programmable Modular Testbed for Backscatter Sensor Network Research," in *Proc. 5th Work. Real-World Wirel. Sens. Networks*, Como Lake, Italy, sep 2013, pp. 153–161.

[10] L. Atzori, A. Iera, and G. Morabito, "The Internet of Things: A survey," *Comput. Networks*, vol. 54, no. 15, pp. 2787–2805, oct 2010.

[11] L. D. Xu, W. He, and S. Li, "Internet of Things in Industries: A Survey," *IEEE Trans. Ind. Informatics*, vol. 10, no. 4, pp. 2233–2243, nov 2014.

[12] P. Kamalinejad, C. Mahapatra, Z. Sheng, S. Mirabbasi, V. C. M. Leung, and Y. L. Guan, "Wireless energy harvesting for the Internet of Things," *IEEE Commun. Mag.*, vol. 53, no. 6, pp. 102–108, jun 2015.

[13] V. Lakafosis, A. Rida, R. Vyas, L. Yang, S. Nikolaou, and M. M. Tentzeris, "Progress Towards the First Wireless Sensor Networks Consisting of Inkjet-Printed, Paper-Based RFID-Enabled Sensor Tags," *Proc. IEEE*, vol. 98, no. 9, pp. 1601–1609, sep 2010.

[14] J. G. Hester, S. Kim, J. Bito, T. Le, J. Kimionis, D. Revier, C. Saintsing, W. Su, B. Tehrani, A. Traille, B. S. Cook, and M. M. Tentzeris, "Additively Manufactured Nanotechnology and Origami-Enabled Flexible Microwave Electronics," *Proc. IEEE*, vol. 103, no. 4, pp. 583–606, apr 2015.

[15] H. Stockman, "Communication by Means of Reflected Power," *Proc. IRE*, pp. 1196–1204, oct 1948.

[16] *EPC Radio-Frequency Identity Protocols, Class-1 Generation-2 UHF RFID Protocol for Communications at 860MHz–960MHz, version 1.2.0*. EPC Global, 2008.

[17] G. Vannucci, A. Bletsas, and D. Leigh, "A Software-Defined Radio System for Backscatter Sensor Networks," *IEEE Trans. Wirel. Commun.*, vol. 7, no. 6, pp. 2170–2179, jun 2008.

[18] A. P. Sample, D. J. Yeager, P. S. Powledge, and J. R. Smith, "Design of a Passively-Powered, Programmable Sensing Platform for UHF RFID Systems," in *2007 IEEE Int. Conf. RFID*. IEEE, 2007, pp. 149–156.

[19] J. Kimionis, A. Bletsas, and J. N. Sahalos, "Design and implementation of RFID systems with software defined radio," in *2012 6th Eur. Conf. Antennas Propag.* Prague, Czech Republic: IEEE, mar 2012, pp. 3464–3468.

[20] E. Kampianakis, J. Kimionis, K. Tountas, C. Konstantopoulos, E. Koutroulis, and A. Bletsas, "Wireless Environmental Sensor Networking With Analog Scatter Radio and Timer Principles," *IEEE Sens. J.*, vol. 14, no. 10, pp. 3365–3376, oct 2014.

[21] A. P. Sample, J. Braun, A. Parks, and J. R. Smith, "Photovoltaic enhanced UHF RFID tag antennas for dual purpose energy harvesting," in *2011 IEEE Int. Conf. RFID*. Orlando, FL: IEEE, apr 2011, pp. 146–153.

[22] S. Kim, A. Georgiadis, A. Collado, and M. M. Tentzeris, "An Inkjet-Printed Solar-Powered Wireless Beacon on Paper for Identification and Wireless Power Transmission Applications," *IEEE Trans. Microw. Theory Tech.*, vol. 60, no. 12, pp. 4178–4186, dec 2012.

[23] R. J. Vyas, B. B. Cook, Y. Kawahara, and M. M. Tentzeris, "E-WEHP: A Batteryless Embedded Sensor-Platform Wirelessly Powered From Ambient Digital-TV Signals," *IEEE Trans. Microw. Theory Tech.*, vol. 61, no. 6, pp. 2491–2505, jun 2013.

[24] J. Kimionis and M. M. Tentzeris, "RF tag front-end design for uncompromised communication and harvesting," in *2014 IEEE RFID Technol. Appl. Conf.* Tampere, Finland: IEEE, sep 2014, pp. 109–114.

[25] D. M. Dobkin, *The RF in RFID: Passive UHF RFID in Practice*. Newton, MA, USA: Newnes (Elsevier), 2008.

[26] J. Griffin and G. Durgin, "Complete Link Budgets for Backscatter-Radio and RFID Systems," *IEEE Antennas Propag. Mag.*, vol. 51, no. 2, pp. 11–25, apr 2009.

[27] D. Tse and P. Viswanath, *Fundamentals of Wireless Communication*. Cambridge University Press, 2005.

[28] Daeyoung Kim, M. Ingram, and W. Smith, "Measurements of small-scale fading and path loss for long range RF tags," *IEEE Trans. Antennas Propag.*, vol. 51, no. 8, pp. 1740–1749, aug 2003.

[29] U. Karthaus and M. Fischer, "Fully integrated passive UHF RFID transponder ic with 16.7-μW minimum RF input power," *IEEE J. Solid-State Circuits*, vol. 38, no. 10, pp. 1602–1608, oct 2003.

[30] P. Nikitin, K. Rao, S. Lam, V. Pillai, R. Martinez, and H. Heinrich, "Power reflection coefficient analysis for complex impedances in RFID tag design," *IEEE Trans. Microw. Theory Tech.*, vol. 53, no. 9, pp. 2721–2725, sep 2005.

[31] A. Bletsas, A. G. Dimitriou, and J. N. Sahalos, "Improving Backscatter Radio Tag Efficiency," *IEEE Trans. Microw. Theory Tech.*, vol. 58, no. 6, pp. 1502–1509, jun 2010.

[32] C. He and Z. J. Wang, "Closed-Form BER Analysis of Non-Coherent FSK in MISO Double Rayleigh Fading/RFID Channel," *IEEE Commun. Lett.*, vol. 15, no. 8, pp. 848–850, aug 2011.

[33] C. He, X. Chen, Z. J. Wang, and W. Su, "On the performance of MIMO RFID backscattering channels," *EURASIP J. Wirel. Commun. Netw.*, vol. 2012, no. 1, pp. 1–15, 2012.

[34] J. D. Griffin and G. D. Durgin, "Gains For RF Tags Using Multiple Antennas," *IEEE Trans. Antennas Propag.*, vol. 56, no. 2, pp. 563–570, 2008.

[35] ——, "Multipath Fading Measurements at 5.8 GHz for Backscatter Tags With Multiple Antennas," *IEEE Trans. Antennas Propag.*, vol. 58, no. 11, pp. 3693–3700, nov 2010.

[36] D. D. Donno, F. Ricciato, L. Catarinucci, A. Coluccia, and L. Tarricone, "Challenge: Towards Distributed RFID Sensing with Software-defined Radio," in *16th Annu. Int. Conf. Mob. Comput. Netw. (ACM MobiCom)*, Chicago, IL, 2010, pp. 97–104.

[37] M. Buettner and D. Wetherall, "A 'Gen 2' RFID Monitor Based on the USRP," *ACM SIGCOMM Comput. Commun. Rev.*, vol. 40, no. 3, pp. 42–47, jul 2010.

[38] S. J. Thomas, E. Wheeler, J. Teizer, and M. S. Reynolds, "Quadrature Amplitude Modulated Backscatter in Passive and Semipassive UHF RFID Systems," *IEEE Trans. Microw. Theory Tech.*, vol. 60, no. 4, pp. 1175–1182, apr 2012.

[39] M. S. Trotter, C. R. Valenta, G. A. Koo, B. R. Marshall, and G. D. Durgin, "Multi-Antenna Techniques for Enabling Passive {RFID} Tags and Sensors at Microwave Frequencies," in *Proc. IEEE {RFID} {C}onf.*, Orlando, FL, apr 2012.

[40] P. Chan and V. Fusco, "Bi-static 5.8GHz RFID range enhancement using retrodirective techniques," in *41st Eur. Microw. Conf.*, Manchester, United Kingdom, oct 2011, pp. 976–979.

[41] F. Amato, C. W. Peterson, B. P. Degnan, and G. D. Durgin, "A 45 uW bias power, 34 dB gain reflection amplifier exploiting the tunneling effect for RFID applications," in *2015 IEEE Int. Conf. RFID*. IEEE, apr 2015, pp. 137–144.

[42] M. M. Kaleja, P. Heide, and E. M. Biebl, "Imaging RFID system at 24 gigahertz for object localization," in *IEEE MTT-S Int. Microw. Symp. Dig.*, Anaheim, CA, USA, jun 1999, pp. 1497–1500.

[43] A. Strobel, C. Carlowitz, R. Wolf, F. Ellinger, and M. Vossiek, "A Millimeter-Wave Low-Power Active Backscatter Tag for FMCW Radar Systems," *IEEE Trans. Microw. Theory Tech.*, vol. 61, no. 5, pp. 1964–1972, may 2013.

[44] F. Amato, H. M. Torun, and G. D. Durgin, "Beyond the limits of classic backscattering communications: A quantum tunneling RFID tag," *IEEE Int. Conf. . . .*, 2017.

[45] J. G. Proakis, *Digital Communications*, 4th ed. New York, NY: McGraw-Hill, Inc., 2001.

[46] S. J. Maeng and B. G. Lee, "A design of linear-phased IIR Nyquist filters," *IEEE J. Sel. Areas Commun.*, vol. 13, no. 1, pp. 167–175, jan 1995.

[47] G. Vougioukas, S.-N. Daskalakis, and A. Bletsas, "Could battery-less scatter radio tags achieve 270-meter range?" in *2016 IEEE Wirel. Power Transf. Conf.* Aveiro, Portugal: IEEE, may 2016, pp. 1–3.

[48] J. Kimionis, A. Bletsas, and J. N. Sahalos, "Bistatic backscatter radio for tag read-range extension," in *2012 IEEE Int. Conf. RFID-Technologies Appl.* Nice, France: IEEE, nov 2012, pp. 356–361.

[49] V. Liu, A. Parks, V. Talla, S. Gollakota, D. Wetherall, and J. R. Smith, "Ambient Backscatter: Wireless Communication Out Of Thin Air," in *Proc. ACM SIGCOMM 2013 Conf. SIGCOMM*. Hong Kong, China: ACM, 2013, pp. 39–50.

[50] R. Correia and N. B. Carvalho, "Design of high order modulation backscatter wireless sensor for passive IoT solutions," in *2016 IEEE Wirel. Power Transf. Conf.* Aveiro, Portugal: IEEE, may 2016, pp. 1–3.

[51] Y. Ma, X. Hui, and E. C. Kan, "Harmonic-WISP: A passive broadband harmonic RFID platform," in *2016 IEEE MTT-S Int. Microw. Symp.* San Francisco, CA: IEEE, may 2016, pp. 1–4.

[52] M. Winkler, T. Faseth, H. Arthaber, and G. Magerl, "An UHF RFID tag emulator for precise emulation of the physical layer," in *Wirel. Technol. Conf. (EuWIT), 2010 Eur.*, Paris, France, sep 2010, pp. 273–276.

[53] V. Viikari, J. Chisum, and H. Seppä, "Wireless passive photo detector for insect tracking," *Microw. Opt. Technol. Lett.*, vol. 52, no. 10, pp. 2312–2315, jul 2010.

[54] Y. Taur and T. H. Ning, *Fundamentals of modern VLSI devices*, 2nd ed. Cambridge University Press, 2013.

[55] S. Kim, R. Vyas, J. Bito, K. Niotaki, A. Collado, A. Georgiadis, and M. M. Tentzeris, "Ambient RF Energy-Harvesting Technologies for Self-Sustainable Standalone Wireless Sensor Platforms," *Proc. IEEE*, vol. 102, no. 11, pp. 1649–1666, nov 2014.

[56] K. Gudan, S. Chemishkian, J. J. Hull, S. J. Thomas, J. Ensworth, and M. S. Reynolds, "A 2.4GHz ambient RF energy harvesting system with −20dBm minimum input power and NiMH battery storage," in *2014 IEEE RFID Technol. Appl. Conf.* Tampere, Finland: IEEE, sep 2014, pp. 7–12.

[57] Young-Ho Suh and Kai Chang, "A high-efficiency dual-frequency rectenna for 2.45- and 5.8-GHz wireless power transmission," *IEEE Trans. Microw. Theory Tech.*, vol. 50, no. 7, pp. 1784–1789, jul 2002.

[58] R. Scheeler, S. Korhummel, and Z. Popovic, "A Dual-Frequency Ultralow-Power Efficient 0.5-g Rectenna," *IEEE Microw. Mag.*, vol. 15, no. 1, pp. 109–114, jan 2014.

[59] D. Masotti, A. Costanzo, M. Del Prete, and V. Rizzoli, "Genetic-based design of a tetra-band high-efficiency radio-frequency energy harvesting system," *IET Microw,, Antennas Propag.*, vol. 7, no. 15, pp. 1254–1263, 2013.

[60] Z. P. N.P. Basta E.A. Falkenstein, "Bow-tie rectenna arrays," in *Proc. 2015 IEEE MTT-S Wirel. Power Transf. Conf.*, Boulder, CO, may 2015.

[61] B. Strassner and Kai Chang, "5.8-GHz circularly polarized dual-rhombic-loop traveling-wave rectifying antenna for low power-density wireless power transmission applications," *IEEE Trans. Microw. Theory Tech.*, vol. 51, no. 5, pp. 1548–1553, may 2003.

[62] N. Shinohara and H. Matsumoto, "Experimental study of large rectenna array for microwave energy transmission," *IEEE Trans. Microw. Theory Tech.*, vol. 46, no. 3, pp. 261–268, mar 1998.

[63] A. N. Parks and J. R. Smith, "Sifting through the airwaves: Efficient and scalable multiband RF harvesting," in *2014 IEEE Int. Conf. RFID (IEEE RFID)*. IEEE, apr 2014, pp. 74–81.

[64] S. D. Assimonis, S.-N. Daskalakis, and A. Bletsas, "Efficient RF harvesting for low-power input with low-cost lossy substrate rectenna grid," in *2014 IEEE RFID Technol. Appl. Conf.* IEEE, sep 2014, pp. 1–6.

[65] J. Kimionis, A. Georgiadis, M. Isakov, H. J. Qi, and M. M. Tentzeris, "3D/inkjet-printed origami antennas for multi-direction RF harvesting," in *2015 IEEE MTT-S Int. Microw. Symp.* Phoenix, AZ: IEEE, may 2015, pp. 1–4.

[66] B. S. Cook, J. R. Cooper, and M. M. Tentzeris, "Multi-Layer RF Capacitors on Flexible Substrates Utilizing Inkjet Printed Dielectric Polymers," *IEEE Microw. Wirel. Components Lett.*, vol. 23, no. 7, pp. 353–355, jul 2013.

[67] B. S. Cook, C. Mariotti, J. R. Cooper, D. Revier, B. K. Tehrani, L. Aluigi, L. Roselli, and M. M. Tentzeris, "Inkjet-printed, vertically-integrated, high-performance inductors and transformers on flexible LCP substrate," in *2014 IEEE MTT-S Int. Microw. Symp.* IEEE, jun 2014, pp. 1–4.

[68] S. A. Nauroze, J. Hester, W. Su, and M. M. Tentzeris, "Inkjet-printed substrate integrated waveguides (SIW) with drill-less vias on paper substrates," in *2016 IEEE MTT-S Int. Microw. Symp.* IEEE, may 2016, pp. 1–4.

[69] B. S. Cook and A. Shamim, "Inkjet Printing of Novel Wideband and High Gain Antennas on Low-Cost Paper Substrate," *IEEE Trans. Antennas Propag.*, vol. 60, no. 9, pp. 4148–4156, sep 2012.

[70] H. Subbaraman, D. T. Pham, X. Xu, M. Y. Chen, A. Hosseini, X. Lu, and R. T. Chen, "Inkjet-Printed Two-Dimensional Phased-Array Antenna on a Flexible Substrate," *IEEE Antennas Wirel. Propag. Lett.*, vol. 12, pp. 170–173, 2013.

[71] J. Kimionis, M. Isakov, B. S. Koh, A. Georgiadis, and M. M. Tentzeris, "3D-Printed Origami Packaging With Inkjet-Printed Antennas for RF Harvesting Sensors," *IEEE Trans. Microw. Theory Tech.*, vol. 63, no. 12, pp. 4521–4532, dec 2015.

[72] K. A. Nate, J. Hester, M. Isakov, R. Bahr, and M. M. Tentzeris, "A fully printed multilayer aperture-coupled patch antenna using hybrid 3D / inkjet additive manufacturing technique," in *2015 Eur. Microw. Conf.* Paris, France: IEEE, sep 2015, pp. 610–613.

[73] F. Fuschini, C. Piersanti, F. Paolazzi, and G. Falciasecca, "Analytical Approach to the Backscattering from {UHF RFID} Transponder," *IEEE Antennas Wirel. Propag. Lett.*, vol. 7, pp. 33–35, 2008.

[74] P. Chan and V. Fusco, "Full duplex reflection amplifier tag," *IET Microwaves, Antennas Propag.*, vol. 7, no. 6, pp. 415–420, apr 2013.

[75] A. Georgiadis and A. Collado, "Solar powered Class-{E} active antenna oscillator for wireless power transmission," in *Proc. 2013 IEEE Radio Wirel. Symp.*, Austin, TX, jan 2013, pp. 40–42.

[76] J. Ebert and M. Kazimierczuk, "Class {E} high-efficiency tuned power oscillator," *IEEE J. Solid-State Circuits*, vol. 16, no. 2, pp. 62–66, apr 1981.

[77] J.-F. Bousquet, S. Magierowski, and G. G. Messier, "A 4-GHz Active Scatterer in 130-nm CMOS for Phase Sweep Amplify-and-Forward," *IEEE Trans. Circuits Syst. I Regul. Pap.*, vol. 59, no. 3, pp. 529–540, mar 2012.

[78] W. C. Jakes, *Microwave Mobile Communications*. Piscataway, New Jersey, 08855-1331: IEEE Press, 1995.

[79] N. S. Alagha and P. Kabal, "Generalized raised-cosine filters," *IEEE Trans. Commun.*, vol. 47, no. 7, pp. 989–997, jul 1999.

[80] J. Kimionis, A. Georgiadis, A. Collado, and M. M. Tentzeris, "Enhancement of RF Tag Backscatter Efficiency With Low-Power Reflection Amplifiers," *IEEE Trans. Microw. Theory Tech.*, vol. 62, no. 12, pp. 3562–3571, dec 2014.

[81] "ADG904 4:1 Mux/SP4T," Analog Devices, Datasheet, 2013.

[82] "C8051F12x and C8051F13x Mixed-Signal ISP Flash MCU Family," Datasheet, 2003.

[83] "Understanding data converters," Texas Instruments, Tech. Rep. SLAA013, 1995.

[84] P. Xiao, C. Toal, D. Burns, V. Fusco, and C. Cowan, "Transmit and receive filter design for OFDM based WLAN systems," in *2010 Int. Conf. Wirel. Commun. Signal Process.*, no. 1. IEEE, oct 2010, pp. 1–4.

[85] V. Agarwal, P. Kim, D.-g. Oh, and D.-s. Ahn, "Hardware Efficient Root-Raised-Cosine Pulse Shaping Filter for DVB-S2 Receivers," in *Adv. Comput. Commun. First Int. Conf. ACC 2011, Kochi, India, July 22-24, 2011. Proceedings, Part II*, A. Abraham, J. Lloret Mauri, J. F. Buford, J. Suzuki, and S. M. Thampi, Eds. Berlin, Heidelberg: Springer Berlin Heidelberg, 2011, pp. 595–603.

[86] M. Mitchell, "Using PWM Timer_B as a DAC," Texas Instruments, App. Rep. SLAA116, dec 2000.

[87] "16-Bit PWM Using an On-Chip Timer," Silicon Labs, App. Note AN110, dec 2003.

[88] D. M. Alter, "Using PWM Output as a Digital-to-Analog Converter on a TMS320F280x Digital Signal Controller," Texas Instruments, App. Rep. SPRAA88A, sep 2008.

[89] R. Metivier, "Method for Converting a PWM Output to an Analog Output When Using Hall-Effect Sensor ICs," Allegro Microsystems, LLC, App. Inf. 296094-AN, 2013.

[90] L. Besser and R. Gilmore, *Practical RF circuit design for modern wireless systems. Vol. 2, Active circuits and systems*. Artech House, 2003.

[91] J.-S. G. Hong and M. J. Lancaster, *Microstrip filters for RF/microwave applications*. John Wiley & Sons, 2004.

[92] R. Correia, N. B. Carvalho, and S. Kawasaki, "Continuously Power Delivering for Passive Backscatter Wireless Sensor Networks," *IEEE Trans. Microw. Theory Tech.*, pp. 1–9, 2016.

[93] R. A. Shafik, M. S. Rahman, and A. R. Islam, "On the Extended Relationships Among EVM, BER and SNR as Performance Metrics," in *2006 Int. Conf. Electr. Comput. Eng.*, no. December. IEEE, dec 2006, pp. 408–411.

[94] S. J. Thomas and M. S. Reynolds, "A 96 Mbit/sec, 15.5 pJ/bit 16-QAM modulator for UHF backscatter communication," in *2012 IEEE Int. Conf. RFID*. Orlando, FL: IEEE, apr 2012, pp. 185–190.

[95] J. Kimionis and M. M. Tentzeris, "Pulse Shaping: The Missing Piece of Backscatter Radio and RFID," *IEEE Trans. Microw. Theory Tech.*, vol. 64, no. 12, pp. 4774–4788, dec 2016.

[96] R. Correia, A. Boaventura, and N. B. Carvalho, "Quadrature Amplitude Backscatter Modulator for Passive Wireless Sensors in IoT Applications," *IEEE Trans. Microw. Theory Tech.*, vol. 65, no. 4, pp. 1103–1110, apr 2017.

[97] Q. Ge, C. K. Dunn, H. J. Qi, and M. L. Dunn, "Active origami by {4D} printing," *Smart Mater. Struct.*, vol. 23, no. 9, p. 94007, 2014.

[98] H. J. Qi, T. D. Nguyen, F. Castro, C. M. Yakacki, and R. Shandas, "Finite deformation thermo-mechanical behavior of thermally induced shape memory polymers," *J. Mech. Phys. Solids*, vol. 56, no. 5, pp. 1730–1751, 2008.

[99] Y. Li, N. Kaynia, S. Rudykh, and M. C. Boyce, "Wrinkling of interfacial layers in stratified composites," *Adv. Eng. Mater.*, vol. 15, no. 10, pp. 921–926, 2013.

[100] B. Tehrani, B. S. Cook, and M. M. Tentzeris, "Post-Process Fabrication of Multilayer mm-Wave On-Package Antennas with Inkjet Printing," in *2015 IEEE Int. Symp. Antennas Propagat.*, Vancouver, BC, Canada, jul 2015.

[101] S. B. Walker and J. A. Lewis, "Reactive silver inks for patterning high-conductivity features at mild temperatures," *J. Am. Chem. Soc.*, vol. 134, no. 3, pp. 1419–1421, 2012.

[102] "SunTronic silver nanoparticle ink," Sigma-Aldrich, Spec. Sheet, 2014.

[103] R. Martinez, J. Kimionis, A. Georgiadis, A. Collado, M. Tentzeris, G. Goussetis, and J. L. Tornero, "Circularly polarized shorted ring slot rectenna with a mesh design for optimized inkjet printing on paper substrate," in *2015 9th Eur. Conf. Antennas Propag.*, may 2015, pp. 1–3.

[104] A. Collado and A. Georgiadis, "Conformal Hybrid Solar and Electromagnetic (EM) Energy Harvesting Rectenna," *IEEE Trans. Circuits Syst. I Regul. Pap.*, vol. 60, no. 8, pp. 2225–2234, aug 2013.

[105] B. L. Pham and A.-V. Pham, "Triple bands antenna and high efficiency rectifier design for RF energy harvesting at 900, 1900 and 2400 MHz," in *2013 IEEE MTT-S Int. Microw. Symp. Dig.* IEEE, jun 2013, pp. 1–3.

[106] H. Oraizi, "Design of impedance transformers by the method of least squares," *IEEE Trans. Microw. Theory Tech.*, vol. 44, no. 3, pp. 389–399, 1996.

[107] Y. W. Hsu and E. F. Kuester, "Direct synthesis of passband impedance matching with nonuniform transmission lines," *IEEE Trans. Microw. Theory Tech.*, vol. 58, no. 4, pp. 1012–1021, 2010.

[108] L. Ranzani, P. Boffi, R. Siano, S. Rondineau, Z. Popovic, and M. Martinelli, "Microwave-Domain Analog Predistortion Based on Chirped Delay Lines for Dispersion Compensation of 10-Gb/s Optical Communication Signals," *J. Light. Technol.*, vol. 26, no. 15, pp. 2641–2646, aug 2008.

[109] J. Bito, J. G. Hester, and M. M. Tentzeris, "Ambient RF Energy Harvesting From a Two-Way Talk Radio for Flexible Wearable Wireless Sensor Devices Utilizing Inkjet Printing Technologies," *IEEE Trans. Microw. Theory Tech.*, vol. 63, no. 12, pp. 4533–4543, dec 2015.

[110] T. H. Lin, J. Bito, J. G. Hester, J. Kimionis, R. A. Bahr, and M. M. Tentzeris, "Ambient energy harvesting from two-way talk radio for on-body autonomous wireless sensing network using inkjet and 3D printing," in *2017 IEEE MTT-S Int. Microw. Symp.*, jun 2017, pp. 1034–1037.